

# Engineering Journal

First Quarter 2022 | Volume 59, No. 1



Smarter.  
Stronger.  
Steel.

## Closure

- 1 Investigation on the Performance of a Mathematical Model to Analyze Concentrically Braced Frame Beams with V-Type Bracing Configurations  
Alireza Asgari Hadad and William Thornton
  
- 5 Comparison of Simple and Advanced Methods of Analysis in the AISC *Specification* for Fire-Resistant Structural Design  
Rachel Chicchi and Amit H. Varma
  
- 31 Steel-Plate Composite Wall-to-Reinforced Concrete Wall Mechanical Connection—Part 1: Out-of-Plane Flexural Strength  
Jungil Seo, Hassan S. Anwar, Amit H. Varma, and Yoonho Nam
  
- 53 Practice-Accessible Methodology for Nonlinear Refined Analysis of Gusset Plate Connections of Steel Truss Bridges  
Alireza Mohammadi and Walid S. Najjar
  
- 65 Review of Local Buckling Width-to-Thickness Limits  
Ben W. Schafer, Louis F. Geschwindner, Tom Sabol, and Chia-Ming Uang
  
- 85 Errata

# Engineering Journal

American Institute of Steel Construction

Dedicated to the development and improvement of steel construction,  
through the interchange of ideas, experiences, and data.

## Editorial Staff

Editor	Margaret A. Matthew, PE
Managing Editor	Keith A. Grubb, SE, PE
Research Editor	Judy Liu, PhD
Production Editor	Kristin Hall

## Officers

Stephen H. Knitter  
Chair

Hugh J. McCaffrey  
Vice Chair

Edward Seglias  
Secretary/Legal Counsel

Charles J. Carter, SE, PE, PhD  
President

Scott L. Melnick  
Senior Vice President

Mark W. Trimble, PE  
Senior Vice President

Carly Hurd, CAE  
Vice President

Lawrence F. Kruth, PE  
Vice President

Brian Raff  
Vice President

The articles contained herein are not intended to represent official attitudes, recommendations or policies of the Institute. The Institute is not responsible for any statements made or opinions expressed by contributors to this Journal.

The opinions of the authors herein do not represent an official position of the Institute, and in every case the officially adopted publications of the Institute will control and supersede any suggestions or modifications contained in any articles herein.

The information presented herein is based on recognized engineering principles and is for general information only. While it is believed to be accurate, this information should not be applied to any specific application without competent professional examination and verification by a licensed professional engineer. Anyone making use of this information assumes all liability arising from such use.

Manuscripts are welcomed, but publication cannot be guaranteed. All manuscripts should be submitted in duplicate. Authors do not receive a remuneration. Guidelines for authors are printed on the inside back cover.

*Engineering Journal* (ISSN 0013-8029) is published quarterly. Subscriptions: Members: one subscription, \$40 per year, included in dues; Additional Member Subscriptions: \$40 per year. Non-Members U.S.: \$160 per year. Foreign (Canada and Mexico): Members \$80 per year. Non-Members \$160 per year. Published by the American Institute of Steel Construction at 130 E Randolph Street, Suite 2000, Chicago, IL 60601.

Copyright 2021 by the American Institute of Steel Construction. All rights reserved. No part of this publication may be reproduced without written permission. The AISC logo is a registered trademark of AISC.

**Subscriptions:** [subscriptions@aisc.org](mailto:subscriptions@aisc.org), 312.670.2400

**Archives:** Search at [aisc.org/ej](http://aisc.org/ej). Article downloads are free for current members and are available for a nominal fee for non-members.

# Investigation on the Performance of a Mathematical Model to Analyze Concentrically Braced Frame Beams with V-Type Bracing Configurations

ALIREZA ASGARI HADAD and WILLIAM THORNTON

---

## ABSTRACT

The discussion-paper published by Roeder et al. (2021), hereafter referred to as the responders for clarity, disputes the results published by Hadad and Fortney (2020) and the chevron effect (CE) analysis method published by Fortney and Thornton (2015, 2017), based on the responders' earlier research results and their understanding of the behavior of chevron beams. This paper provides the reply to the disputed topics.

---

### WEAK BEAM VERSUS STRONG BEAM MECHANISMS

According to the literature, there are two failure mechanisms in chevron-braced bays: (1) a weak beam mechanism in which the buckling of the compression brace causes an unbalanced force to be applied on the beam and subsequently the formation of plastic hinges in the beam and where weak beams lead to considerable plastification in columns, beams, and braces, irrespective of brace slenderness, and (2) a strong beam mechanism where buckling of the compression brace is followed by yielding of the tension brace, the beam being sufficiently strong to remain elastic despite the vertical unbalanced force applied to it by the braces at mid-span. Chevron-braced frames (CBFs) with strong beams and weak braces exhibit a more uniform distribution of yielding with height than frames with weak beams and strong braces.

The intention behind explaining the mentioned mechanisms in the paper was to show the importance of chevron beams in determining the behavior of V-bracing and X-bracing CBF. The paper does not consider any mechanism superior to the other one. Below is the exact statement from the paper:

*“It is not evident from the data in the literature which collapse mechanism is preferable.”* (Hadad and Fortney, 2020; emphasis added)

Although the responders consider the weak beam mechanism superior to the other failure mechanism based on their earlier research (Sen et al., 2016), they can review the other literature (Shen et al., 2015) to see how the weak beam mechanism is challenged. D’Aniello et al. (2015) showed the importance of chevron beam strength and stiffness in determining the behavior of concentrically braced frames. Thus, it is necessary to understand the actual demand on chevron beams and design them accordingly before taking a side on the controversial discussion about the desirable behavior of chevron beams. Thus, the authors investigated the performance of the CE method in the paper.

### THE CHEVRON EFFECT ANALYSIS METHOD

The chevron effect (CE) method provides simple, closed-form solutions for normal and shear forces in the beam at the gusset to beam interface. There was no available information on these forces on the beam section until the CE analysis method (Fortney and Thornton, 2015, 2017) was published. Designers require a method to design these connections for buildings in a reasonable time frame. The responders criticize the authors' approach but provide no alternate method. Figure 3 in the responders' paper (Roeder et al., 2021) showed a broken line in the chevron region, which is exactly that part of the beam where the CE method shows the actual shear force and bending moment distributions. What do the responders propose for this region? The responders should have calculated the beam shear force demand for the connections in the analyzed frame using the CE method. The question of whether a beam that is inadequate per the CE method nevertheless performs adequately

---

Alireza Asgari Hadad, PhD, Structural Engineer, GEI Consultants, Inc., Marquette, Mich., Email: aahadad@geiconsultants.com (corresponding)

William Thornton, PhD, PE, NAE, Corporate Consultant, Cives Engineering Corporation, Roswell, Ga. Email: bthornton@cives.com

---

Paper No. 2018-07RC

seems obvious but is not addressed by the responders' analyses. If the beams, selected using other criteria, have sufficient strength per the CE method, their adequate performance can be interpreted as supporting the CE method.

The finite element studies of Hadad and Fortney (2020) were intended to verify the reasonable accuracy of the simple closed-form solutions of the original two papers. That goal was achieved. The results of the paper showed the chevron effect can be reasonably analyzed with simple closed-form equations without the use of finite element analysis. With the addition of AISC *Seismic Provisions* Section F2.6c.4 (AISC, 2016), even a seismic special concentrically braced frame (SCBF) design will likely be adequate.

It is worth noting that in buildings with composite floor systems, very little axial force will be carried to the beam-to-column connections. That is the reason Fortney and Thornton (2015, 2017) focused on estimating the shear force and bending moment distribution in chevron beams. The responders' considered the results of a bare 2D frame model to show the importance of axial load in chevron beams. The responders' test model is probably not representative of actual design conditions.

Figure 3 in the responders' paper showed a beam with axial forces. These can be handled by the CE method because it looks at the whole beam, including the chevron zone. The design shears and moments in the chevron region may be bigger than the design values shown in Figure 3.

Additionally, the responders' design relies on the fixity of the beam-to-column connection. This fixity induces shear in the beam that counteracts the chevron effect in the elastic range of drift. For elastic systems, the brace force direction (i.e., tension or compression) correlates with the drift direction such that both reverse in unison, and the offsetting of the beam-shear effects may be reliable. This correlation between brace force direction and drift direction likely holds for an SCBF. The large peak forces associated with the initial buckling strength of the brace in compression may occur only once, or once in each direction. For both of these peak-force conditions, the shear from the beam fixity reduces the chevron-effect shear force within the connection. However, for buckling-restrained braced frames, such correlation between drift direction and brace-force direction no longer holds after yielding of the braces. As such, the beam shear from the moment-frame behavior could be additive to the chevron shear. Recommendation to ignore the chevron effect generally and not limited to the specific configuration and system studied by the responders is irresponsible and could lead to unanticipated and potentially undesirable mechanisms in systems the responders have not considered or analyzed. The responders' failure to examine, or even consider, the statics of the connection results in their erroneous conclusion that the chevron does not exist because, in the case they studied, it is offset by another effect.

The authors do believe the CE method is not the ultimate method in the analysis of chevron configured brace frames, and thus, they appreciate and encourage the discussions on the CE analysis method and the efforts to further improve its accuracy. However, the inclusion of the chevron effect phenomenon, as confirmed by other researchers (Sabelli and Saxey, 2021), is a necessity to understand the shear force and bending moment demands on chevron beams. Until more accurate and convenient methods are available, the CE method is encouraged to be used in the analysis and design of new structures.

#### **FINITE ELEMENT ANALYSES TO INVESTIGATE THE CHEVRON EFFECT METHOD**

To evaluate the accuracy of the CE analysis method, the authors studied the shear force and bending moment distributions along the whole length of the beams in a group of beam-gusset assemblies through finite element analysis. The beam length in Figures 7 to 11 of the original paper is 300 in. as presented in Table 1 (Hadad and Fortney, 2020). The results published in the paper show:

- The existence of chevron effect and the success of the CE analysis method in identifying the phenomenon through its simple closed form solutions.
- The reasonable accuracy of the CE analysis method in estimating the beam shear force and bending moment in chevron beams, specifically in the beam-to-gusset plate connection region, while it requires no finite element analysis and a relatively small amount of time to be performed.

Because the paper investigated the performance of the CE analysis method that was introduced earlier (Fortney and Thornton, 2015, 2017), the same modeling approach was used in the finite element models (i.e., simply supported beams with gusset plate(s) in the middle carrying the brace loads).

The responders believe the chevron beams in braced frames should not be considered as simply supported beams due to the relative rigidity in the connection region. They also consider the gusset to be part of the beam increasing its strength. It could be helpful if the responders reported forces across section cuts at one or more chevron connections at the time of maximum shear force, such as shown in Figure 1. Such section cuts would reveal whether the shear force outside the connection region is offsetting the chevron shear, whether the moment on Section 1 is less than that determined based on brace axial forces (due to brace resisting moment), whether the gusset reinforces the web (as the proposed by the responders), or whether the distribution of shear force between the two is better described by the CE method.

Also, a reanalysis of the frame presented in the responders' paper without moment connections at the roof beam, perhaps with a beam that does not meet the required shear strength as determined using the CE method, could improve the discussion. The beam at the roof level in the responders' analyses appears to be a heavy beam with moment connections. Are such measures required in order for a design that does not consider the chevron effect to perform well?

Considering all the assumptions in the responders' analysis model, do the responders have a simple way of analyzing braced frames based on these considerations or have a complex finite element computer program is required? Until such time as a simple closed-form solution calculation method is available, the authors believe that the CE analysis method, as verified by the paper, is adequate to produce an acceptable design very quickly.

### DUCTILITY FACTOR AND STRESS DISTRIBUTIONS IN THE BEAM-TO-GUSSET PLATE CONNECTION INTERFACE

The ductility factor is considered in the literature (Richard, 1986; Hewitt and Thornton, 2004) as one possible solution to accommodate the stress concentrations in the design of welds connecting gusset plates to beams. The authors decided to examine the value of this factor based on the results obtained from the chevron beam-gusset assemblies studied in the research (Hadad and Fortney, 2019, 2020). To do so, the authors compared the actual stress distribution at gusset-to-weld interface versus the average of the stress values. None of the stress values were calculated based on CE method. The results clearly showed the factor needs to be changed.

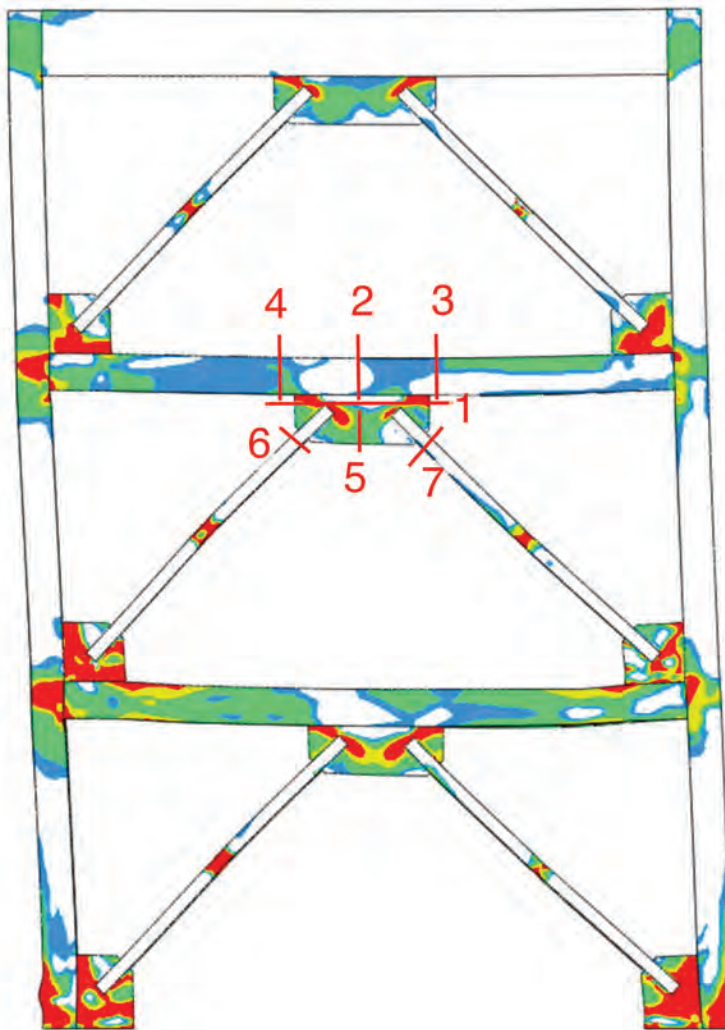


Fig. 1. Suggested sections that could be studied in the responders' model.

With respect to Figure 2 in the responders' discussion, it should be noted that this test was one of two tests that were identical except for the weld sizes. The weld sizes in the Figure 2 tests were sized for the gusset edge forces while the identical test had the weld increased by the AISC ductility factor of 1.25. In this second test the welds survived the fracture of the brace with no cracks. The requirement of AISC *Seismic Provisions* Section F2.6c.4 (AISC, 2016) is a direct result of the Figure 2 test, but did not explicitly involve a chevron gusset.

The solution suggested by the authors to use the gusset plate shear strength in designing the weld connecting the gusset plate to the chevron beam is obviously not the only possible solution. It is just a suggestion by the authors. Other researchers are highly encouraged to participate in this effort and suggest better solutions.

### CONCLUSION

The chevron effect analysis method is the pioneering method in identifying the chevron effect in chevron configured concentrically braced frames. The method provides simple closed form solutions for structural designers to estimate the shear force and bending moment distributions along the chevron beam length without requiring them to run computationally expensive finite element analyses. The performed investigations showed the reasonable accuracy of the method.

The authors appreciate the attention of the responders, the reviewers' helpful comments, and other structural engineers and researchers for their feedbacks on the method since it has been published. Such comments help the authors in improving the chevron effect analysis method.

### REFERENCES

- AISC (2016), *Seismic Provisions for Structural Steel Buildings*, ANSI/AISC 341-16, American Institute of Steel Construction, Chicago, Ill.
- D'Aniello, M., Costanzo, S., and Landolfo, R. (2015), "The Influence of Beam Stiffness on Seismic Response of Chevron Concentric Bracings," *Journal of Constructional Steel Research*, Vol. 112, pp. 305–324.
- Fortney, P.J. and Thornton, W.A. (2015), "The Chevron Effect—Not an Isolated Problem," *Engineering Journal*, AISC, Vol. 52, No. 2, pp. 125–163.
- Fortney, P.J. and Thornton, W.A. (2017), "The Chevron Effect and Analysis of Chevron Beams—A Paradigm Shift," *Engineering Journal*, AISC, Vol. 54, No. 4, pp. 263–296.
- Hadad, A.A. and Fortney, P.J. (2019), "Studying the Ductility Factor for Middle Gusset Connections in Chevron Braced Frame Configurations," *Proceedings of the ASCE/SEI Structures Congress: Buildings and Natural Disasters*, ASCE, Reston, Va.
- Hadad, A.A. and Fortney, P.J. (2020), "Investigation on the Performance of a Mathematical Model to Analyze Concentrically Braced Frame Beam," *Engineering Journal*, AISC, Vol. 57, No. 2, pp. 91–108.
- Hewitt, C.M. and Thornton, W.A. (2004), "Rationale Behind and Proper Application of the Ductility Factor for Bracing Connections Subjected to Shear and Transverse Loading," *Engineering Journal*, AISC, Vol. 41, No. 1, pp. 3–6.
- Richard, R.M. (1986), "Analysis of Large Bracing Connection Designs for Heavy Construction," *Proceedings of the National Steel Construction Conference*, AISC, Chicago, Ill.
- Roeder, C.W., Lehman, D.E., Tan, Q., Berman, J.W., and Sen, A. (2021), "Discussion—Investigation on the Performance of a Mathematical Model to Analyze Concentrically Braced Frame Beam," *Engineering Journal*, AISC, Vol. 58, No. 1, pp. 1–9.
- Sabelli, R. and Saxey, B. (2021), "Design for Local Member Shear at Brace and Diagonal-Member Connections: Full-Height and Chevron Gussets," *Engineering Journal*, AISC, Vol. 58, No.1, pp. 45–78.
- Sen, A.D., Roeder, C.W., Berman, J.W., Lehman, D.E., Li, C.-H., Wu, A.-C., and Tsai, K.-C. (2016), "Experimental Investigation of Chevron Concentrically Braced Frames with Yielding Beams," *Journal of Structural Engineering*, Vol. 142, No. 12, pp. 04016123.
- Shen, J., Wen, R., and Akbas, B. (2015), "Mechanisms in Two-Story X-Braced Frames," *Journal of Constructional Steel Research*, Vol. 106, pp. 258–277.

# Comparison of Simple and Advanced Methods of Analysis in the AISC Specification for Fire-Resistant Structural Design

RACHEL CHICCHI and AMIT H. VARMA

---

## ABSTRACT

AISC *Specification* Appendix 4 (AISC, 2016b) provides criteria to aid structural engineers in structural design for fire conditions. It includes an advanced method of analysis and a simple method of analysis. The simple method provides straightforward equations to determine member capacities at elevated temperatures. However, determination of demands on the structure (forces and deformations) due to elevated temperatures is less clear. This paper aims to minimize these gaps in knowledge. A comparison of these methods will be articulated through the analysis of a 10-story office building. The building is a steel structure with perimeter moment frames and a composite floor system that was designed for hazards in Chicago, Illinois. In order to conduct the advanced analyses, a three-dimensional (3D) finite element method building model was developed using ABAQUS (2016). This model can simulate inelastic deformations, instability failures, connection damage at elevated temperatures, and the effect of temperature on strength and stiffness of materials. The simple analyses were conducted using SAP2000 (CSI, 2018), a commercially available structural analysis and design software. A comparison of results from each method of analysis shows that for gravity framing members, the advanced method produced the longest fire-resistance rating. The fire-resistance rating determined from the simple method was more conservative, resulting in a shorter resistance rating. The simple method was also found to be the most conservative approach for the moment-resisting frame members, making it a less desirable method for designing the lateral system for fire than the prescriptive approach. Use of the simple method may be most advantageous for gravity framing applications only and may be overly conservative for considerations of the lateral framing system.

**Keywords:** fire resistant design, steel, simple method, performance-based design.

---

## INTRODUCTION

Structural design for fire conditions in the United States has traditionally been conducted by architects and fire protection engineers using a prescriptive approach. This approach is based on standard furnace tests of components and assemblies, which do not always correlate well with realistic building behavior. Following the World Trade Center collapse in 2001, structural fire engineering research and design began to move toward a performance-based approach that considers system-level response and design fires specific to each building (occupancy, materials, ventilation, etc.). With this shift, structural engineers have a more active role in the structural design for fire conditions. In an effort to facilitate this shift in responsibility, the American Institute of Steel Construction (AISC) authored and continues to update Appendix 4 of the AISC *Specification*

(2016b), which provides guidance on structural design for fire conditions. This appendix includes design guidance for using advanced and simple methods of analysis.

## Summary of Structural Design Approaches for Fire

Appendix 4 alludes to three primary methods of analysis or design for fire: the advanced and simple methods of analysis and the prescriptive method for design. The advanced method incorporates several considerations in its analysis. These include strength and stiffness deterioration with increasing temperature, thermal expansions and large deformations, second-order effects, inelasticity, and the ability to simulate all potential limit states, among many others. These analyses are performed in accordance with AISC *Specification* Appendix 1.3.1 (2016b). This modeling approach is often used for large or complex structures with irregularities in stiffness or geometry, though it is becoming an increasingly prevalent approach for analyzing regular buildings as engineers become more competent in designing for fire.

The simple method of analysis is a member-based approach that evaluates member adequacy using load and resistance factor design. It allows the designer to employ reasonable and conservative simplifying assumptions in order to assess member adequacy without the detailed modeling necessary for the advanced method. The simple

---

Rachel Chicchi, Assistant Professor, Department of Civil and Architectural Engineering and Construction Management, University of Cincinnati, Cincinnati, Ohio. Email: rachel.chicchi@uc.edu (corresponding)

Amit H. Varma, Karl H. Kettelhut Professor in Civil Engineering, Purdue University, West Lafayette, Ind. Email: ahvarma@purdue.edu

---

Paper No. 2020-13

method approach captures common limit states but does not currently include all potential limit states. For example, local buckling limit states and connection failure modes are not currently considered in Appendix 4. The simple approach also enables the designer to calculate the member design strength at a specific temperature but does not consider the member's behavior over time or evaluate the performance of the structure overall. The design equations for the simple method were primarily based on work by Takagi and Deierlein (2007), which showed close correlation to ECCS (2001) and detailed finite element models that were validated against physical test data.

The prescriptive approach of fire-resistance ratings is based on standard furnace tests of short span members. This approach does not specifically consider building geometries and loadings. The International Building Code (ICC, 2018) specifies the required fire-resistance rating (FRR) based on the ASTM E119 (2015) standard for structural members based on the size, number of stories, use of space, and building importance. This rating is the time (in hours) that an element or system can be exposed to a standard fire before it reaches its critical temperature or approaches collapse under applied loads. A database of successfully tested assemblies is used to determine the fireproofing thickness required on each structural member in order to achieve the necessary fire-resistance rating. The forthcoming 2022 edition of the AISC *Specification* will include more information about the prescriptive method, including design applications.

While the prescriptive approach is used widely in the U.S. building industry due to its simplicity and successful performance history, the standard fire-tested assemblies do not always translate well into real building behavior and can be overly conservative, limiting design capabilities of the structural engineer and architect. The advanced analysis method provides a performance-based approach that allows the design team and the owner to better understand building behavior, including anticipated extent of damage, due to fire hazards. The simple method allows for a comparison of design strength and resistance of individual members that is typically less computationally and labor expensive than the advanced method. These methods provide the potential for optimization of structural framing and flexibility of design.

This paper discusses the analysis of a case study building for a design fire using the simple and advanced methods of analysis. The prescriptive method of design was used to design the case study building and then the adequacy of the design was evaluated and compared with the results of the simple and advanced methods. The primary objectives of this paper are to (1) provide practical recommendations for the implementation of the simple method of analysis using the SAP2000 (CSI, 2018) software and (2) provide a comparison between the results of each method.

## BACKGROUND

Existing studies have been performed that apply the advanced analysis method to three-dimensional (3D) steel building finite element models, including Agarwal and Varma (2014), Fischer et al. (2019), Khorasani et al. (2019), and Gernay and Khorasani (2020). These models are capable of capturing all potential limit states, including composite slab behavior, connection failure, and inelastic column buckling. Two-dimensional models or single-compartment 3D models can also be modeled using the advanced method but may not adequately consider slab continuity and boundary conditions that are represented in a full building model.

In addition to previous research studies, the American Society of Civil Engineers (ASCE) published performance-based structural fire design examples that provide additional guidance on structural fire design using ASCE 7-16, Appendix E (ASCE, 2016). This includes design procedures, performance objectives, and recommendations generated by engineers at four different design firms across the United States. Performance objectives are typically determined in coordination with the owner, engineer, and authority having jurisdiction (AHJ). These are metrics of the intended performance of the structure under fire effects. The code-minimum requirement (ASCE, 2016; ICC, 2018) for performance is to maintain structural integrity for a period of time in order to ensure safe and complete evacuation of the building occupants. This period of time is known as the fire-resistance rating. Higher levels of performance may be required such as no collapse throughout the duration of the fire or extending the timeframe of structural integrity (i.e., increasing the fire-resistance rating beyond the code-minimum requirement).

## FIRE ANALYSIS AND DESIGN METHODOLOGY

An exemplar case study building will be used to demonstrate the simple and advanced methods of analysis and ultimately compare the results of each method. The fire-resistance rating achieved from each method will be compared as well as the demands determined from each approach. The advanced method provides an indication of the behavior of the system over time through a virtual simulation, while the simple method typically evaluates a design based on the peak demands of the structure. Thus, direct comparison of demands between these two methods is difficult if comparisons are not made at the same point in time. For the purposes of this comparative study, member demands were evaluated at a specific time (at 1 hr). One hour is the building's prescribed fire-resistance rating, and the case study structure was design for this code-minimum requirement.



When performing an analysis and design of a structure under fire, the performance objectives established for that design must be evaluated. If maintaining structural integrity throughout the duration of the fire is a performance objective, then consideration of demands and design strength at all phases of the design fire ought to be considered. Consideration should also be given to the effects of cooling, which could cause contraction (tensile forces) in connections. Connection design using the simple method is beyond the scope of this paper and requires further research and understanding.

## Analysis Considerations

### *Fire Types and Locations*

AISC *Specification* Appendix 4 (2016b) indicates that structural members should be designed for a design-basis fire, which is a fire that captures the likely heating conditions within the building based on fuel load densities and compartment characteristics. Appendix 4 specifies three types of design-basis fires: localized, post-flashover compartment, and exterior fires. After ignition and growth of the fire, flashover may occur, which initiates a fully developed, or post-flashover, fire. Localized fires are those that do not cause flashover due to either a lack of fuel or oxygen. These fires typically develop temperatures much lower than post-flashover fires. Post-flashover compartment fires are fully developed fires where the temperature within the compartment is presumed to be homogenous throughout. Compartments are defined as areas within the building that are bounded by fire-rated boundaries that can contain the fire throughout its duration (NFPA, 2020). Exterior fires occur when radiation and flames escape post-flashover compartment fires that could compromise structural members outside of the compartment. Only post-flashover compartment fires are being used in this study. Refer to the Appendix 4 Commentary for additional resources for identifying fire curves for the other fire types.

Engineering judgment must also be used to determine which critical locations within the building to analyze for fire. Areas prone to progressive collapse under fire loading should be considered; this may include members carrying high loads and/or long spans. Consideration should also be given to the likelihood of each fire event; for instance, spaces with equipment that could malfunction and initiate a fire should be considered. Also, areas with high fuel load density should be evaluated, as well as areas less accessible to firefighting measures.

### *Thermal Gradient*

Thermal gradient is the change in internal temperature of a structural member across its length and cross-section. The

assumptions regarding the design fire will influence the thermal gradient of the structural member. It was assumed that the fire is post-flashover; thus, a simplified one-zone modeling approach is used, and temperatures are modeled as constant along the length of the member. Localized fires, or those simulated using more realistic fire conditions, may invalidate this simplifying assumption.

Composite beams and steel columns may experience different thermal gradients along their cross section. The bottom flange of a composite beam is typically exposed to a fire from all sides while the top flange is insulated by the concrete slab on metal deck it connects to. This creates a higher internal temperature in the bottom flange of the beam than the top flange, creating a nonuniform thermal gradient in composite beams. The simple method accounts for this by applying a 25% reduction in steel temperature at the top flange of the cross section relative to the remainder of the cross section. When using the advanced method, the temperature gradient is typically determined by conducting heat transfer analyses to determine temperatures at different locations along the cross section.

In this study, it was assumed for simplicity that the columns were subjected to uniform heating from all sides. In design, this assumption should be carefully considered. The layout of the compartments and the location of the columns within the compartment or at the exterior of the compartment would influence the fire exposure assumptions for the columns. For instance, for a column located in the center of a compartment exposed to a post-flashover fire, uniform fire loading is a reasonable assumption. However, if the column is located at the edge of a compartment where there is a potential for one side (or corner) of the column to be exposed to the fire and other sides to not be, a nonuniform fire-loading scenario may want to be employed.

Nonuniform heating on gravity columns was studied by Agarwal et al. (2014) and Choe et al. (2016). They found that slender columns with heavy loading experienced premature elastic buckling due to the thermal gradient; however, most nonslender columns were minimally affected by the thermal gradient. For these reasons, the columns in this study were assumed to experience a uniform thermal gradient.

### *Fire Load Combination*

Appendix 4 specifies the following load combination to be used for fire analyses. This load combination also corresponds to the load combination for extraordinary events in ASCE/SEI 7 (2016).

$$1.2D + A_T + 0.5L + 0.2S \quad (1)$$

where  $D$  is the dead load,  $L$  is the live load, and  $S$  is the snow load. The variable  $A_T$  is defined as the nominal forces and deformations due to the design-basis fire, which can be

simulated directly through the analysis. A dead load factor of 0.9 may also be used in Equation 1 in lieu of the 1.2 factor in situations where the dead load helps stabilize the structure. Note that it may be preferable to use roof live load instead of snow load for structural fire design since the probability of snow load concurrently with fire is low. Live load reduction (LLR) per ASCE/SEI 7 was not considered in the presented results. However, live load reduction, which accounts for the reduced likelihood of the full live load acting on the structure, can be helpful in reducing the demands on the structure. Incorporating live load reduction may be especially beneficial for evaluating column designs. This load combination was used for both the simple and advanced methods of analysis.

### Case Study Building

The case study structure is a 10-story office building designed to comply with U.S. building codes and standards: IBC (ICC, 2018), ASCE/SEI 7 (2016), and the AISC *Specification* (2016b). The structure was designed for hazard levels in Chicago, Illinois. It is a three-bay by five-bay structure, with each bay measuring 25 ft (7.63 m) × 25 ft (7.63 m). Each story height is 12 ft (3.66 m). The structure is a traditional steel-framed building with a partially composite floor system. The lateral system is a perimeter moment frame system using ordinary moment frames. Refer to Figure 1 for a typical framing plan. Triangles at columns indicate moment connections.

### Preliminary Design

The building was designed for a dead load of 65 pounds per square foot (psf) and a live load of 50 psf. The composite floor slab is a 3-in., 20-gauge (75-mm) composite deck with 2½-in. (65-mm) lightweight concrete topping. The gravity beams are W14×22 and the gravity girders are W18×35. For simplicity, the gravity framing for the roof is the same as the typical floors. The moment frame design was controlled by a wind drift limit of  $L/400$ , where  $L$  is the building height. Table 1 shows the moment frame and gravity column member sizes.

The minimum fireproofing required for each member was determined using the prescriptive method of design. The case study office building is classified as building occupancy B per IBC, which corresponds to a Type IB building. Type IB buildings require a 2-hr FRR on all framing members; however, if proper control valves and initiating devices are used in conjunction with the sprinkler system, then the building can be reduced to Type IIA per IBC, Section 403, which requires only a 1-hr FRR for all structural members. The case study building was designed for a 1-hr FRR per Type IIA construction.

Spray-applied fire-resistive material (SFRM) was selected to protect the steel members and achieve the necessary 1-hr FRR. Fireproofing thickness,  $d_p$ , for each structural member was determined based on fire tests conducted by Underwriters Laboratory (UL) (2018). These tests consist of a limited number of individual components and assemblies

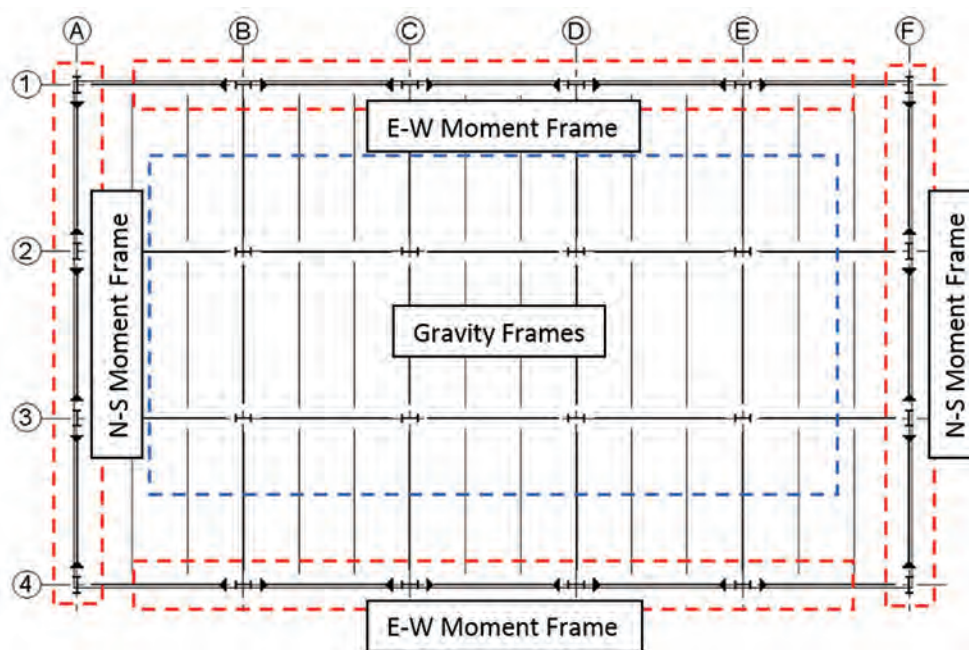


Fig. 1. Case study building framing plan.

**Table 1. Member Sizes Used in Case Study Building**

Story	N-S MF Beams	N-S MF Columns	E-W MF Girders	E-W MF Columns	Gravity Columns
9–10	W18×50	W14×53	W18×35	W12×45	W8×24
7–8	W21×83	W14×90	W18×50	W14×53	W8×40
5–6	W21×93	W14×109	W18×60	W14×99	W12×58
3–4	W21×111	W14×159	W18×71	W14×145	W14×74
1–2	W27×217	W14×311	W21×132	W14×283	W14×90

**Table 2. SFRM Thicknesses per Prescriptive Approach**

	Member Size	UL Assembly	Thickness, $d_p$ , in. (mm)
Beams	W14×22	D902	1 <sup>1</sup> / <sub>16</sub> (18)
	W18×35	D902	9 <sup>1</sup> / <sub>16</sub> (15)
	W18×60	D902	1/2 (13)
	W21×93	D902	3 <sup>1</sup> / <sub>8</sub> (10)
Columns	W12×58	X772	1 <sup>1</sup> / <sub>16</sub> (18)
	W14×99	X772	9 <sup>1</sup> / <sub>16</sub> (15)
	W14×109	X772	9 <sup>1</sup> / <sub>16</sub> (15)

subjected to furnace tests per ASTM E119 (2015). Ruddy et al. (2003) provide guidance to designers on how to use fire test results to determine fireproofing thicknesses.

Heat transfer is a function of both the density and surface area of a member. Therefore, wide flange members are categorized by a  $W/D$  value, where  $W$  is the weight per linear foot and  $D$  is the perimeter of the member cross section that is exposed to the fire. Thickness adjustment equations provided in UL are used to convert the fireproofing thickness of the tested beam or column to the necessary thickness of the member being designed. Table 2 summarizes the member sizes, UL assembly designations, and SFRM thicknesses determined for the structural members analyzed in this project. Thicknesses were rounded to the nearest 1/16 in. The composite deck is not fire protected, as it can already achieve the fire-resistance rating without fireproofing per UL Design D904.

### Fire Hazard Selection

The temperature versus time profile of the design-basis fire should account for fuel load, compartment dimensions, thermal characteristics of the compartment (i.e., walls and ceiling), and ventilation of the space (both natural and mechanical). Standard fire curves such as ASTM E119 (2015), ISO 834 (2015), and Eurocode 1991-1-2 (CEN, 2002) are commonly used to define fire curves. As an alternative to using standard fire curves, the designer may choose to conduct computational fluid dynamics (CFD) or physical fire tests. The National Institute of Standards and

Technology (NIST) also provides the Fire Dynamics Simulator (FDS), which is a CFD program for simulating fire conditions (NIST, 2013). Appendix 4 does not provide specific guidance on how to select the time-temperature fire curve but provides references to assist in selection.

The Eurocode (CEN, 2002) parametric time-temperature approach for determining fire time-temperature curves may be preferable to the other standards because of its simplicity, the ability to modify the curve based on specific building parameters, and the fact that it includes both a heating and cooling portion. This cooling phase can be important as it results in thermal contraction, which can produce large tensile forces and fail connections. These parametric curves assume that the compartment contains a fully developed fire with uniform temperature through the space. These curves are limited to compartments with rectangular enclosures, floor areas less than 500 m<sup>2</sup>, ceiling heights less than 4 m, and no ceiling openings. Eurocode time-temperature curves are calculated using three primary variables: the thermal inertia of the enclosure,  $b$ , (J/m<sup>2</sup>s<sup>1/2</sup>K); opening factor,  $O$ , (m<sup>1/2</sup>); and fire load density,  $q_{t,d}$ , (MJ/m<sup>2</sup>). Eurocode provides guidance on the determination of these values based on the building use, geometry, ventilation, etc. Thermal inertia incorporates the density, specific heat, and thermal conductivity of the walls, ceiling, and floor of the compartment. The opening factor is calculated based on the ratio of opening area to wall area. The fire load density is based on the use of the space (i.e., the combustible materials within the space), as well as the fire-fighting measures and active fire suppression systems.

Figure 2 shows the Eurocode parametric time-temperature curve that was used for this study, denoted in the figure as EN 1991-1-2. The parameters that generated this curve are  $b = 1000 \text{ J/m}^2 \text{ s}^{1/2} \text{ K}$ ,  $O = 0.032 \text{ m}^{1/2}$ ,  $q_{t,d} = 1600 \text{ mJ/m}^2$ . These parameters were chosen because the corresponding Eurocode curve approximately follows the ASTM E119 and ISO 834 curves for 1 hr before beginning the cooling phase. The prescriptive approach is based on physical testing using ASTM E119 or ISO 834 fire curves. By selecting a design fire that matches these curves, a reasonable comparison can be made between the prescriptive approach and the results of the simple and advanced analyses.

The design engineer should use engineering judgment and consult with the owner and the AHJ when selecting appropriate design fires for each building and compartment. For instance, instead of analyzing only one fire scenario, the designer may choose to analyze an array of fire curves to account for a broader range of exposures. Additionally, compartment fires are likely to vary among different areas of the building based on openings (i.e., more openings likely at exterior or corner compartments than interior compartments), changes in fuel load densities based on the use of the space, and thermal properties of the compartment.

### Fire Location Selection

For the purposes of this study, only compartment fires were studied with the presumption that each bay of the structure is an individual compartment. The fifth story (mid-height of the structure) was analyzed because it is beyond the reach of firefighting ladders and hoses, and the columns are still exposed to large axial forces. Three compartments were analyzed and are classified as compartments 5A (corner compartment), 5B (exterior compartment), and 5C (interior compartment), as shown in Figure 3(a). Member sizes

for compartment 5A are shown in Figure 3(b), as this is the compartment that will be presented in detail. Results from compartments 5B and 5C are provided in the Appendix.

## SUMMARY OF ANALYSES

For the advanced method of analysis, a three-dimensional finite element model of the case-study structure was developed using ABAQUS (2016), a commercially available finite element method (FEM) software. This nonlinear, inelastic model can simulate inelastic deformations, instability failures, connection damage at elevated temperatures, and the effect of temperature on material strength and stiffness. The modeling approach was adapted from Agarwal (2011). Heat transfer analyses were performed in order to determine internal temperatures of structural members throughout their cross section. Temperature gradients were applied to the model in 5-min increments.

The simple method of analysis outlined in Appendix 4 allows the structural designer to consider and design for thermal loads within the structure, much in the same way that other loads (i.e., gravity, wind, seismic, etc.) are evaluated. The demands and capacities of individual structural members are determined in order to adequately design the structure using load and resistance factor design (LRFD). This procedure will be applied to the case study building and explained in subsequent sections.

Even within the simple procedure, two different approaches can be used. The first approach is an individual member approach that evaluates individual members in isolation. This approach assumes that the load effects (demands or required strengths) can be assumed to be the same as the ambient conditions. This simplifying assumption should be used with caution and only with proper engineering judgment. It can typically be reasonably applied to regular

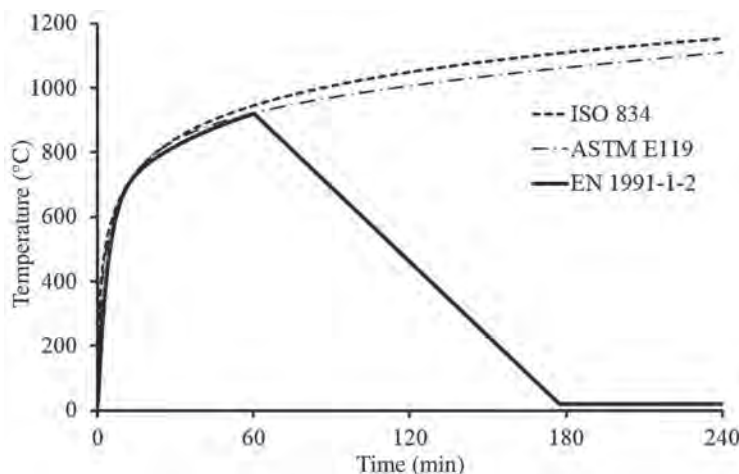


Fig. 2. Fire time-temperature curves.

gravity frames. Alternatively, the second approach evaluates frame behavior. With this approach, stiffness reductions, thermal deformations, and appropriate boundary conditions must be considered. This frame-level approach may be more appropriate for irregular frames with discontinuities. The frame-level approach for the simple method was used throughout this paper using the analysis software, SAP2000.

**Modeling Approach**

*Elements and Connections*

*Advanced Method*

The beams and columns were modeled using two-node beam elements, which approximate 3D solid elements using Timoshenko beam theory. The composite slab was a four-node, reduced integration shell element. Only the concrete

above the flutes (2½ in. thick) was modeled for conservatism and simplicity. ABAQUS contains a built-in embedded rebar option that was used to represent the metal deck. The area of rebar matches the area of metal deck applied only in the strong direction of the deck and was located at the centroid of the shell element. There is no reinforcing applied in the weak direction of the deck. The shear studs, which transfer forces between the slab and beams, were modeled using rigid connectors. A schematic of the modeling approach is shown in Figure 4.

The moment frame connections were modeled as rigid connectors. This simplification was made due to work by Yang et al. (2009), which found through experimental testing that the tested moment connections maintained design strength up to 650°C and with only a 25% reduction in stiffness. The shear tab (gravity) connections in the building were modeled using equivalent wire connector elements that capture the axial force-axial

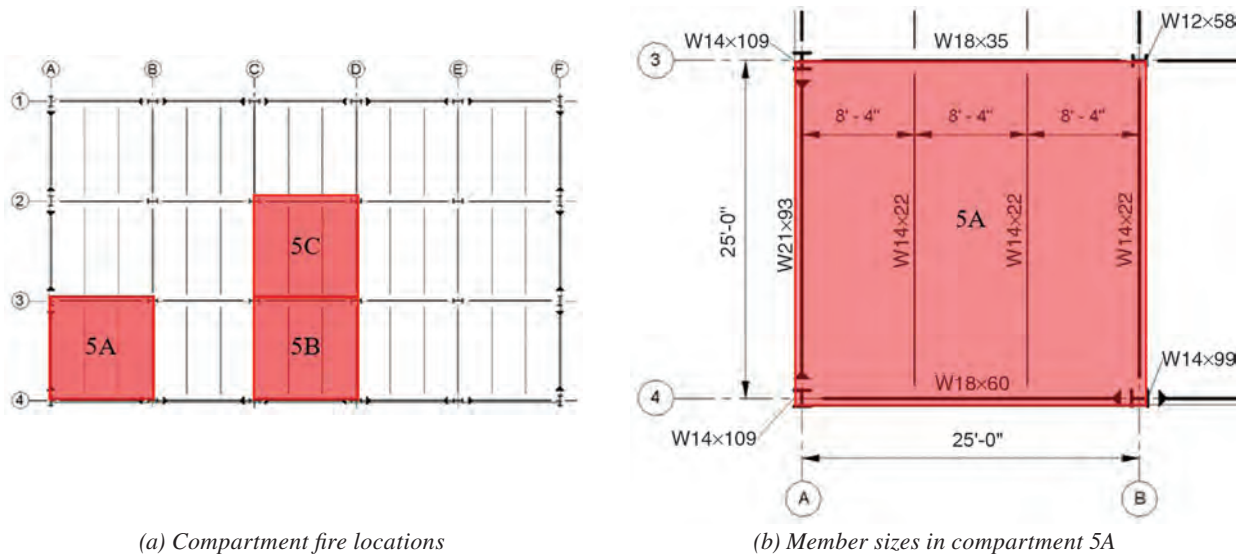


Fig. 3. Layout of compartment fires and member sizes.

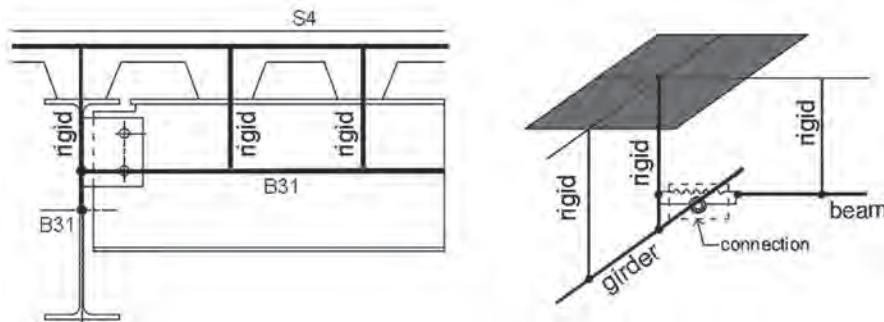

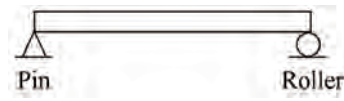
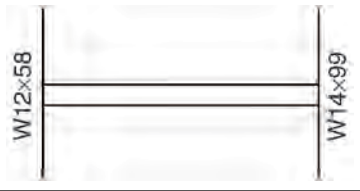
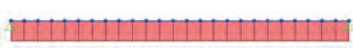




Fig. 4. Schematic of modeling approach for composite floor system (Agarwal and Varma, 2014).

**Table 3. Individual Member Analysis—End Restraints**

	(a)	(b)	(c)
W14×22 member			
Axial load diagram			
Axial load, $F$	310 kips	0 kips	59 kips

displacement-moment-rotation-temperature behavior, based on work by Sarraj (2007) and Agarwal and Varma (2014). It may be especially important to model this behavior so that fracture during the cooling phase, when the steel contracts, can be captured. Fischer et al. (2021) provide a research review of simple shear connection research conducted by a vast number of researchers.

*Simple Method*

Structural steel elements, such as beams and columns, inherently want to expand when exposed to elevated temperatures. This expansion may be partially resisted by the adjacent members framing into the heated element. The stiffness of the adjacent members and the rigidity of the connections influence the level of restraint to which the heated member is subjected. Therefore, if following a frame-level analysis approach, it is imperative that these conditions are modeled in order to accurately simulate member behavior. This is illustrated in Table 3 for a W14×22 beam. This member is 25 ft (300 in.) long and was modeled with different end constraints using SAP2000, a commercially available structural analysis and design software. Using idealized pin constraints at both ends of the heated member induced unrealistically high axial loads [Table 3(a)]. The pin restraints do not permit any movement of the member ends, resulting in very high reactions at these supports. The axial force,  $F$ , induced on the beam due to a temperature of 1306°F was found to be 310 kips using SAP2000. This value can be verified using Equation 2, which is based on the theory of thermal expansion:

$$F = EA\alpha\Delta T \tag{2}$$

where  $E$  is the modulus of elasticity (4,692 ksi due to the elevated temperature),  $A$  is the cross-sectional area of the member (6.49 in.<sup>2</sup>),  $\alpha$  is the coefficient of thermal expansion ( $7.8 \times 10^{-6}/^{\circ}\text{F}$ ), and  $\Delta T$  is elevated temperature (1,306°F).

If a roller is used to replace one of the pins, then all thermally induced axial loads disappear because there

is no restraint to prevent expansion [Table 3(b)]. Because the structural response to fire is highly interdependent on system behavior, analyzing members as individual components in isolation is not recommended. Instead, modeling of the structural system is suggested because it provides reasonable modeling of end restraints. Table 3(c) shows the thermally induced axial load for the simply supported beam framing into W12×58 and W14×99 columns oriented in their weak direction. The resulting axial load of 59 kips demonstrates that the adjacent framing members provide some level of restraint against thermal expansion. If the columns were also exposed to elevated temperatures, the axial load in the W14×22 beam would be influenced by the reductions in column stiffness. Approach (c) is the preferred approach for modeling because Approach (a) with pin-pin constraints results in overly conservative loads and Approach (b) with pin-roller constraints does not account for any axial loads.

As an alternative approach to Approach (c), individual members could be modeled in isolation using spring constraints, but this would require determination of simplified spring constants that represent system behavior. It was decided that modeling the structural system would be simpler. In some cases, such as infill beams with regular, orthogonal framing, Approach (b) may be deemed a reasonable simplifying assumption. Engineer judgment is needed in order to make such simplifications.

SAP2000 was used to model the primary steel members (beams and columns) of the case study building and determine member demands. The steel building was modeled in 3D as shown in Figure 5. Member capacities were calculated by hand using the Appendix 4 equations in Section 4.2.4d. The models include geometric nonlinear (P-delta) effects and linearly elastic material properties. In addition to the load combination described in Equation 1, global stability of the structure should be assessed. This was achieved through notional loads that are 0.2% of the gravity load, which are used to represent the allowable

out of plumb value of  $L/500$  (where  $L$  is the height of the structure) in accordance with the AISC *Code of Standard Practice* (2016a). The direct analysis method, explained in AISC *Specification* Section C2.2 (2016b), was used. This includes a 20% reduction of stiffness ( $EI$  and  $EA$ ) for all members. For simplicity,  $\tau_b$  was set equal to 1.0, and 0.1% of additional gravity loading was applied as notional loads in accordance with AISC *Specification* Section C2.3(c). In lieu of using notional loads, initial imperfections can be directly modeled in accordance with AISC *Specification* Section C2.2a.

For simplicity, only the steel framing was modeled and the composite slab was omitted. Designers may choose to include the composite slab in the model, but then heat transfer would also need to be conducted on the concrete slab. Additionally, SAP2000 does not have a built-in composite slab shell element, so engineering judgment would need

to be made in order to appropriately model the slab using a simplified shell element with shell offsets, body constraints, or links. Main and Sadek of NIST (2013) recommend a weak strip–strong strip approach that can be used with relative ease of modeling.

### Material Models

#### Advanced Method

The Eurocode (CEN, 2002) material models were used for steel and concrete, including thermal properties of conductivity, specific heat, and coefficient of thermal expansion. These codes provide stress-strain relationships at elevated temperatures. These relationships will also be included in the 2022 AISC *Specification*. Isotropic hardening was incorporated into the steel model. The material model for concrete is based on two failure mechanisms: tensile

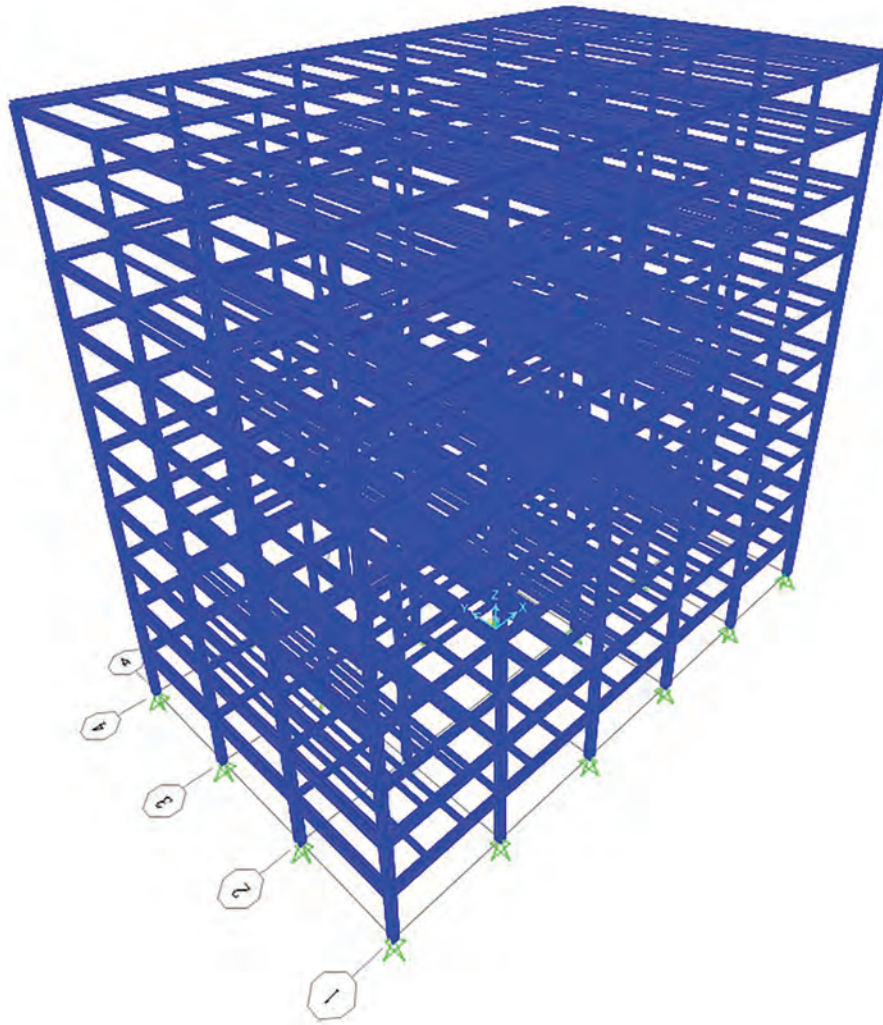


Fig. 5. SAP2000 building model.

**Table 4. Steel Temperatures and Material Properties for the Simple Method**

	Member Size	Steel Temperature, °F (°C)	$k_E = E(T)/E^a$	$E(T),^b$ ksi	$k_Y = F_y(T)/F_y^a$	$F_y(T),^b$ ksi
Beams	W14×22	1150 (621)	0.29	8,382	0.43	21.5
	W18×35	1128 (609)	0.37	10,866	0.48	24.0
	W18×60	993 (534)	0.50	11,513	0.67	33.5
	W21×93	977 (525)	0.51	14,821	0.69	34.6
Columns	W12×58	898 (481)	0.58	16,895	0.80	40.2
	W14×99	869 (465)	0.61	17,654	0.85	42.2
	W14×109	826 (441)	0.65	18,772	0.91	45.2

<sup>a</sup>  $k_E$  and  $k_Y$  are determined based on Appendix 4, Table 4.2.1.  
<sup>b</sup>  $E(T)$  and  $F_y(T)$  are calculated based on the relationship of  $E(T)/E$  defined by  $k_E$  and  $F_y(T)/F_y$  defined by  $k_Y$ .

cracking (using concrete damaged plasticity) and compressive crushing. The concrete material model was based on siliceous aggregates and lightweight concrete.

*Simple Method*

AISC Specification Appendix 4, Section 4.2.4d, provides equations for calculating the nominal strength of members at elevated temperatures due to tension, compression, flexure, and shear. These equations reference the strength equations in the AISC Specification for ambient conditions, with modifications to material properties in order to analyze and design for elevated temperatures.

AISC Specification Appendix 4, Section 4.2.3, consists of tables (Table A-4.2.1 through Table A-4.2.3) that contain retention factors. These factors are used to modify material properties at ambient conditions to represent material properties at elevated conditions. The ambient values used were based on ASTM A992 steel:  $F_y = 50$  ksi,  $F_u = 65$  ksi, and  $E = 29,000$  ksi. Table 4 shows calculated material properties based on the retention factors interpolated from the Appendix 4 tables. The coefficient of thermal expansion,  $\alpha$ , is  $7.8 \times 10^{-6}/^\circ\text{F}$  ( $1.4 \times 10^{-5}/^\circ\text{C}$ ) for structural steel at elevated temperatures, as provided in Appendix 4.

**Heat Transfer**

*Advanced Method*

Before member temperatures can be assigned to the FEM building model, heat transfer analyses must be conducted. ABAQUS was used to conduct 2D heat transfer analyses of each structural member subjected to elevated temperatures. The Eurocode time-temperature curves assume that the compartment fire is a fully developed fire with uniform temperature throughout the compartment, so temperature is uniform along the length of the structural member and,

therefore, there is no need to use 3D heat transfer. The cross section of each member was modeled as a 2D part with the fireproofing at the thickness determined from the prescriptive method. In order to compare with the simple method of analysis that requires a uniform temperature gradient, this same assumption of uniform temperature was applied to columns in the advanced model. Beams were modeled with the composite slab. Thermal properties (specific heat, thermal conductivity, and coefficient of thermal expansion) for steel and concrete were taken from Eurocode. Thermal properties of fireproofing were based on Design Guide 19, *Fire Resistance of Structural Steel Framing* (Ruddy et al., 2003) recommendations: specific heat of 0.18 Btu/lb °F (754 J/kg °C), thermal conductivity of 0.0013 Btu/hr ft °F (0.135 W/m °C), and mass density of 18.3 pcf (293 kg/m<sup>3</sup>). ECCS (1995) also provides thermal properties of fireproofing, but these values were based on ambient-temperature properties. Guidance on thermal properties of fireproofing at elevated temperatures can be found in Carino et al. (2005) and Kodur and Shakya (2013). SFRM properties are temperature dependent, so incorporating temperature-dependent SFRM properties in advanced analyses may be more appropriate. For the purpose of comparison with the simple method, the average values provided in AISC Design Guide 19 were used in this study.

A film subroutine, which includes radiation and convective effects, was used to conduct the heat transfer analyses per Cedeno et al. (2008). The program conducts thermal transfer of heat from the fire to the structural component in 2D across the member cross section. Internal temperatures are then recorded at integration points defined by ABAQUS for standard cross-sectional beam elements. As shown in Figure 6, five integration points (one at each flange edge and one in the web midspan) are used for the wide-flange cross section. ABAQUS linearly interpolates the temperatures between the beam flanges and parabolically interpolates



along the web. Five integration points are also used for the slab (shell element), resulting in a linear interpolation of temperatures. Because only the concrete above the deck flutes was modeled in the building model, temperatures in the slab were recorded at points uniformly distributed across that portion of the slab. Secondary beams were analyzed using the cross section shown in Figure 6, which considered the locations along the beam where the deck flutes are connected to the top surface of the top flange. Designers may want to also evaluate the locations along the beam where the top surface of the beam is not directly attached to the deck flutes. Girders were analyzed in a heat transfer model that included the deck flute geometry.

Figure 7 shows how a W14x22 composite beam subjected to the design-basis fire varies in temperature over time. The steel reaches much higher temperatures than the slab. Additionally, the top flange of the member reaches lower temperatures than the web and bottom flange due to the presence of the slab acting to insulate the top flange. The time-temperature response of the interior gravity column is shown in Figure 8.

**Simple Method**

The AISC *Specification* Appendix 4 Commentary outlines a simple approach for heat transfer known as lumped heat capacity analysis. This one-dimensional analysis can be used to calculate the internal temperature of steel members assuming a uniform temperature distribution of the fire. For

each member subjected to the compartment fire, internal steel temperatures were determined using the equation for protected steel members assuming that Appendix 4, Commentary Equation C-A-4-5, is satisfied:

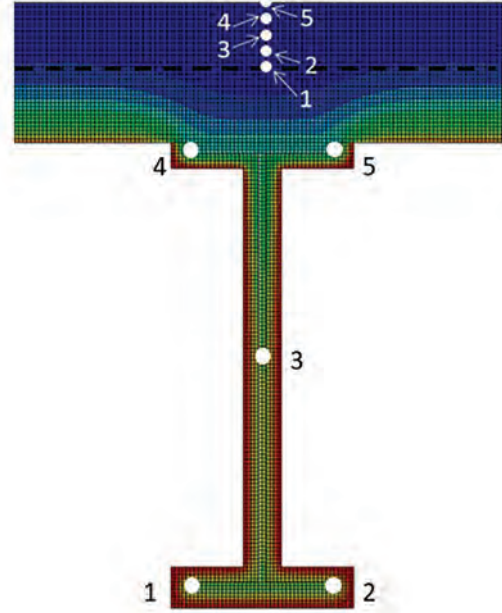


Fig. 6. Temperature gradation and integration points at composite slab with beam directly below.

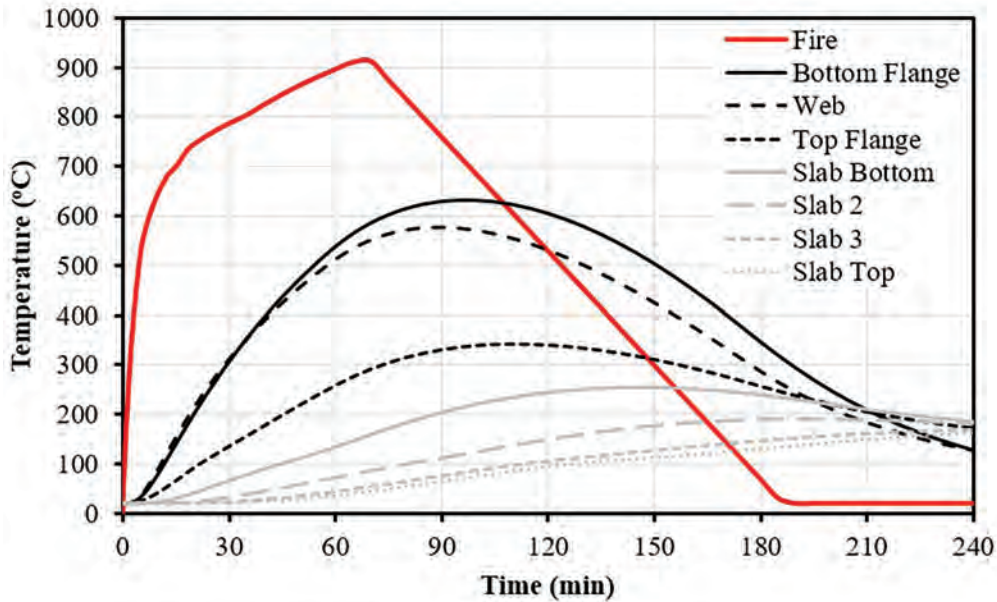


Fig. 7. Time-temperature response of W14x22 composite beam with 1-hr FRR fire protection exposed to fire.

$$\Delta T_s = \frac{k_p}{c_s d_p} \frac{W}{D} (T_F - T_s) \Delta t \quad (3)$$

where  $\Delta T_s$  is the change in steel temperature,  $T_F$  is the temperature of the fire, and  $T_s$  is the temperature of the steel. The time step,  $\Delta t$ , should not exceed 5 s. The thermal properties of SFRM vary by manufacturer. In lieu of manufacturer data, thermal properties were taken from Design Guide 19. The values of density,  $\rho_p$ , specific heat,  $c_p$ , and thermal conductivity,  $k_p$ , used for fireproofing were the same values used in the advanced method. The specific heat of steel,  $c_s$ , varied with temperature and the values were taken from the Eurocode.

The Appendix 4 Commentary also provides a heat transfer equation for cases with unprotected steel, as well as an alternative equation for protected steel when the thermal capacity of the insulation is comparable to the steel thermal capacity. The fireproofing thicknesses,  $d_p$ , determined from the prescriptive method, were used in the heat transfer calculation in order to directly compare the prescriptive and simple methods to one another. The resulting time-temperature curve for a W12x58 column is shown in Figure 8. The Simple curve is the uniform temperature of the W12x58 calculated using the lumped heat capacity equation. The Advanced curve shows the temperature determined through computational heat transfer analyses for the advanced method. This temperature was recorded at the tip

of the column flange. This shows a reasonable relationship between the simple and advanced methods of heat transfer analysis.

Table 5 provides the internal temperatures calculated using the lumped heat capacity analysis for each of the members subjected to compartment fires after 1 hr of heating and at the peak temperature. Peak temperatures will likely be used for analysis with the simple method, but this study will record temperatures at 1 hr in order to compare the simple and advanced methods. Table 6 provides a summary of the internal steel temperatures recorded at 1 hr from the ABAQUS heat transfer analyses versus the simple lumped heat transfer method. Temperatures for the bottom flange, web, and top flange are recorded at locations 1, 3, and 4 in Figure 6, respectively. Temperatures resulting from the simple method tend to be conservatively higher than the ABAQUS results. The bottom flange temperatures in both methods are reasonably comparable.

## Thermal Loading

### Advanced Method

Temperatures determined from the heat transfer model were recorded at the five integration points for the wide-flange members, which were modeled as beam elements. Five points were also recorded along the depth of the slab, which was modeled as a shell element. These temperatures were

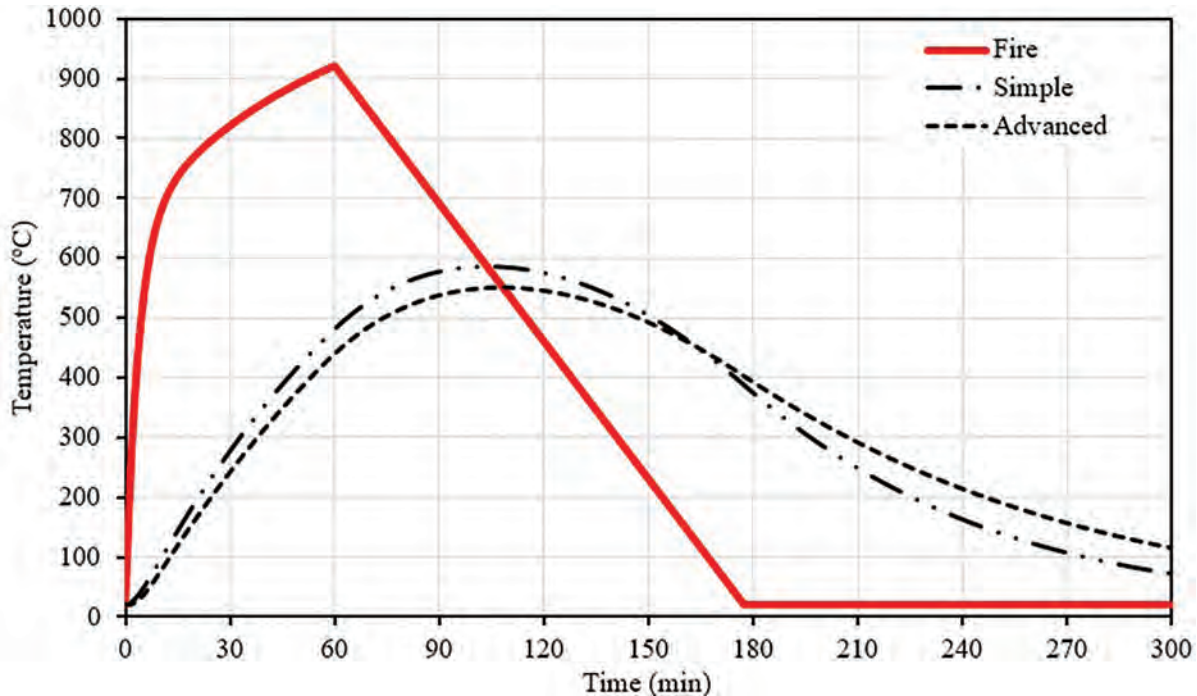


Fig. 8. Results of lumped heat capacity analysis for W12x58 column.

	<b>Member Size</b>	<b><math>T_s</math> at 60 Min °F (°C)</b>	<b><math>T_s</math> Max °F (°C)</b>
Beams	W14×22	1150 (621)	1276 (691)
	W18×35	1128 (609)	1261 (683)
	W18×60	993 (534)	1160 (627)
	W21×93	977 (525)	1148 (620)
Columns	W12×58	898 (481)	1087 (586)
	W14×99	869 (465)	1063 (573)
	W14×109	826 (441)	1027 (553)

	<b>Member Size</b>	<b>Steel Temperature, °F (°C) at 60 Min</b>			
		<b>Simple</b>	<b>ABAQUS</b>		
			<b>Bottom Flange</b>	<b>Web</b>	<b>Top Flange</b>
Beams	W14×22	1150 (621)	999 (537)	953 (512)	496 (258)
	W18×35	1128 (609)	1040 (578)	1049 (583)	511 (284)
	W18×60	993 (534)	914 (508)	945 (525)	481 (267)
	W21×93	977 (525)	913 (507)	986 (530)	508 (282)
Columns	W12×58	898 (481)	792 (440)	851 (473)	792 (440)
	W14×99	869 (465)	817 (436)	763 (406)	817 (436)
	W14×109	826 (441)	759 (404)	707 (375)	759 (404)

recorded at 5-min intervals and input into the ABAQUS structural model as internal temperatures of the structural members within the compartment. Because the material models implemented in ABAQUS incorporated the stress-strain behavior and thermal elongation at elevated temperatures, these temperatures applied to the model resulted in member forces and deformations due to fire.

### **Simple Method**

Temperature effects on member forces and deformations were accounted for by assigning member temperatures, modified steel mechanical properties at elevated temperatures, and coefficient of expansion values. For each fire scenario, three models were created to compare the effect of changing parameters on the member forces that were observed. These models, which all include notional loads and second-order effects, are:

Case 1: Model only gravity loads ( $1.2D + 0.5L$ ).

Case 2: Model Case 1 plus member temperatures and the coefficient of thermal expansion.

Case 3: Model Case 2 plus modulus of elasticity reductions for members exposed to fire.

When evaluating the forces in the beams due to elevated temperatures, the axial loads were very high when assigning the lumped steel temperature across the entire cross section. With a uniform temperature throughout the cross section, these forces acted only axially and did not produce any thermally induced moments that would be expected in reality. The composite slab insulates the top flange of the beam, which results in lower temperatures at that location. Appendix 4, Section 4.2.4d(d), allows for a 25% reduction in steel temperature at the top flange of the cross section. The reduced temperature can be used for the top half of the beam, as shown in Figure 9(a). This simple method of analysis conservatively produces steel temperatures greater than the advanced analyses, as was demonstrated in Table 6.

Temperature effects can be assigned to the member cross sections using SAP2000. The software currently permits a constant temperature over the cross section as well as linear temperature gradients along the depth and width of the cross section. The temperature profile shown in Figure 9(a) cannot currently be applied in SAP2000. Instead, a constant temperature,  $T_{equiv}$ , and a linear gradient were combined to produce the temperature profile in Figure 9(b). The constant temperature was applied to the SAP2000 model in order to produce an equivalent axial load as the profile

in Figure 9(a) (i.e., area times change in temperature are equal), along with a linear gradient. This approach produced slightly higher thermally induced moments due to the additional temperature at the bottom half of the cross section caused by the linear gradient.

## DISCUSSION OF RESULTS

### Results of Advanced Analyses

The structural members in compartment 5A were subjected to the full fire time-temperature curve. This resulted in failure of the internal gravity W12x58 column, as shown in Figure 10(b). This failure did not occur until the column reached 544°C at 95 min. Figure 10(a) shows the deflected shape of the structure at 60 min. At this time, the floor framing had deflected approximately 12 in., but no significant damage had occurred. The member demands that were determined from the ABAQUS model at 60 min will be summarized in order to compare results from the advanced and simple methods of analysis.

The compartment fires in 5B (exterior) and 5C (interior) also resulted in gravity column buckling at 95 min. The deformed shapes are shown in Figure 11(a) and 11(b) for compartment 5B and 5C, respectively. In compartment 5B, two of the gravity columns buckled, resulting in partial collapse of the structure. The compartment 5C fire resulted in buckling of all four gravity columns, which eventually led to complete collapse of the structure. Figure 11(b) shows a snapshot of the deformed shape prior to complete collapse. In both fire scenarios, the structure was able to withstand the fire until 95 min, which is beyond the 1-hr

fire-resistance rating of the structure. The comparison of member demands in ABAQUS versus SAP2000 is provided in the Appendix of this paper.

### Results of Simple Analyses

#### Axial Demands

Table 7 summarizes the axial demands for beams and columns computed in the SAP2000 models for each of the three aforementioned load cases (Cases 1–3). These demands were determined for compartment fires at 5A, 5B, and 5C. For brevity, results from fire 5A are described below, and fire 5B and 5C results are provided in the appendix of this paper. “CL” indicates beams along the column line, while “INF” indicates infill beams. “E” stands for edge column, and “C” means a corner column.

Case 1 does not include temperature effects, so the beams experience negligible axial loads and the columns have axial loads due only to gravity loads. Case 2 introduces member temperatures and the coefficient of thermal expansion. This causes axial loads in the beams. Note that the axial load of the W14x22 infill beams (not along the column lines) is minimal at only 5 kips because it frames into a girder that provides minimal restraint against expansion. This is in contrast to the W14x22 beams along the column lines that experience 45 kips of axial load due to the restraint provided by the column supports. Case 2 also tends to cause an increase in axial load for the moment frame columns. The gravity columns, however, do not experience any increase in axial loading due to temperature. This is because the members framing into the gravity columns are all modeled with idealized, pinned end conditions that do not restrain

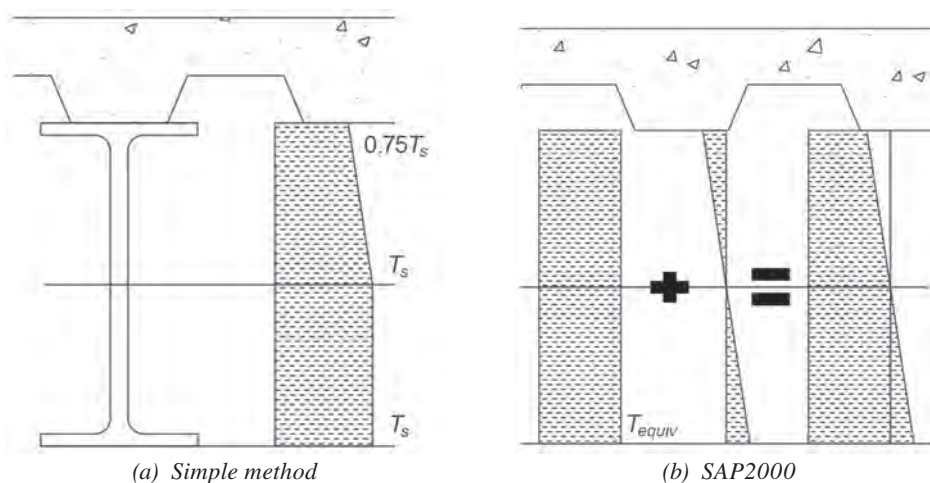
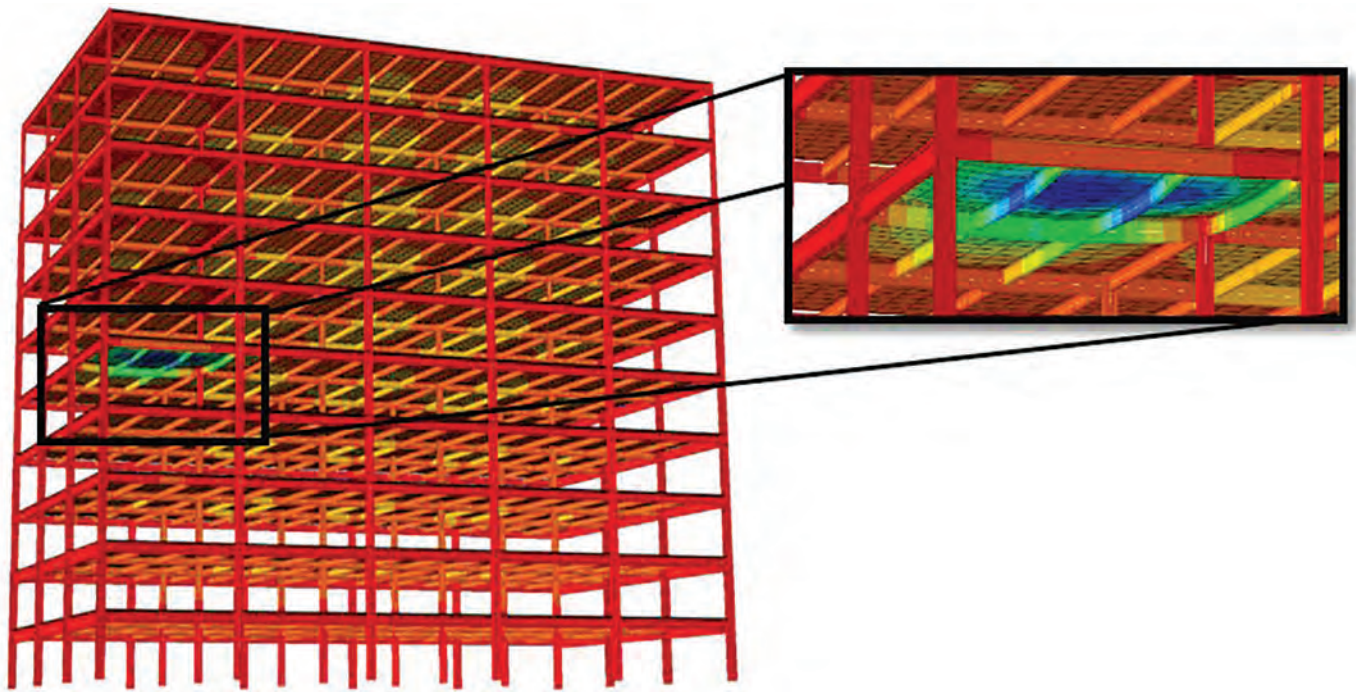
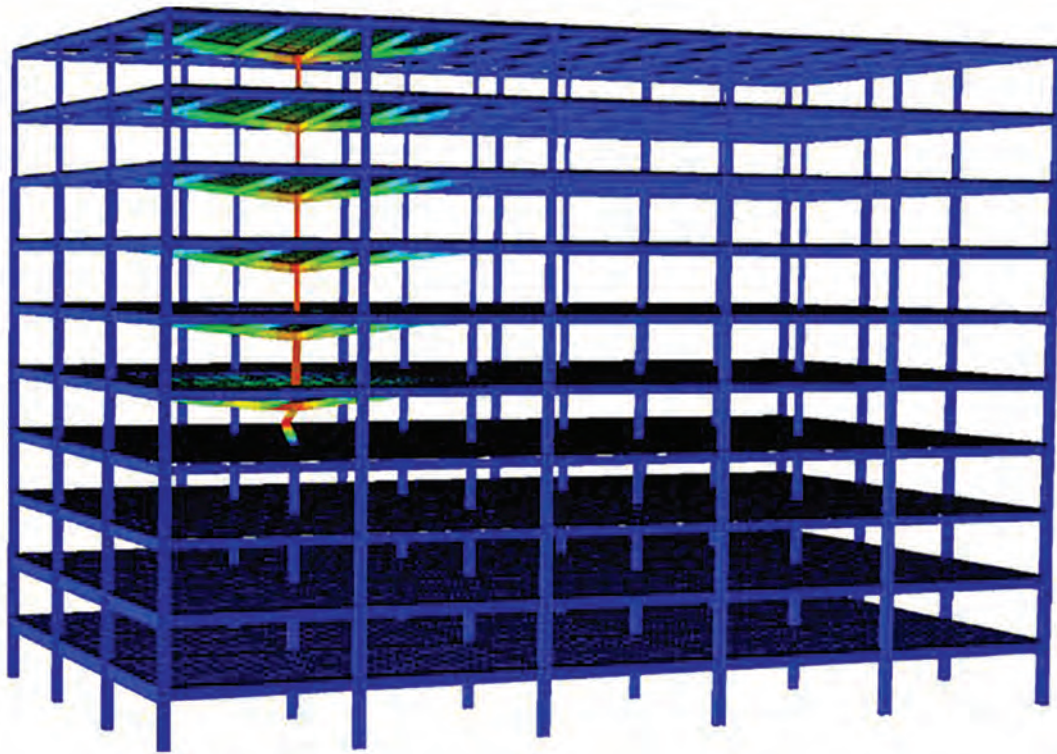


Fig. 9. Thermal gradient across composite beam section.

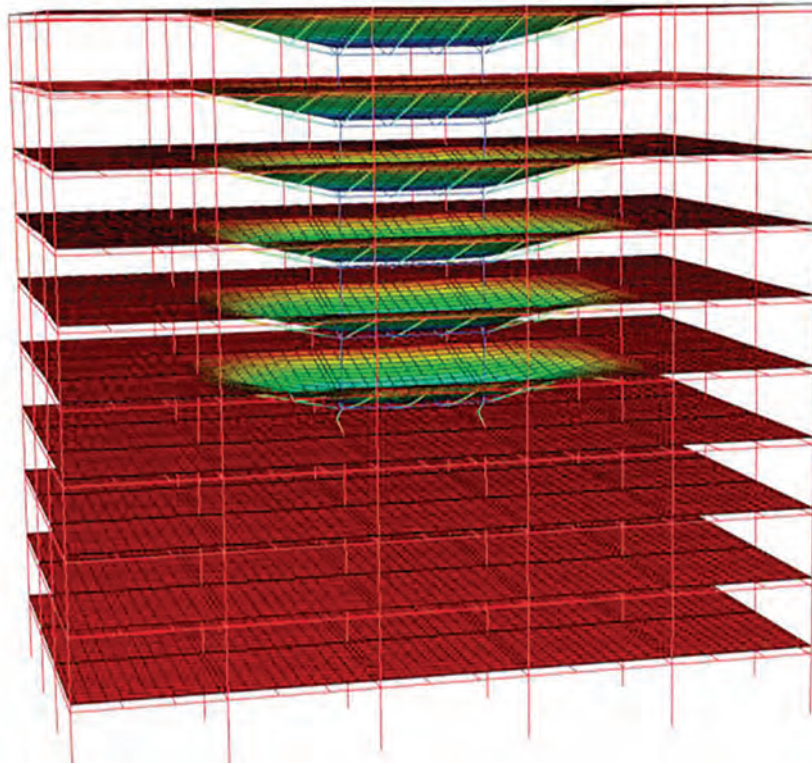


(a) At 60 minutes

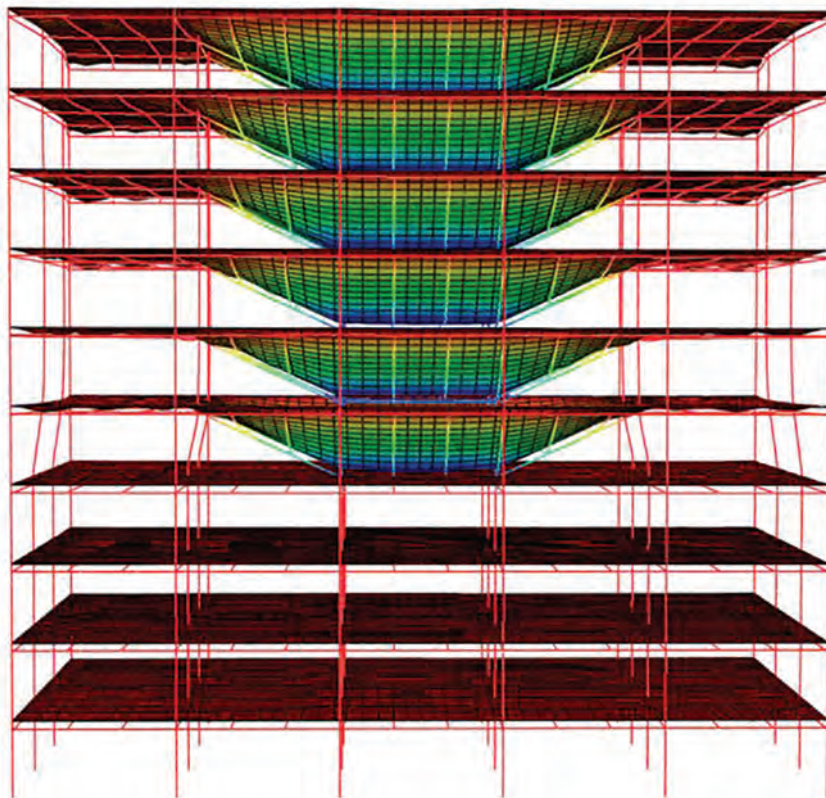


(b) At end of fire

Fig. 10. Deformed shape due to fire in compartment 5A.



(a) Compartment 5B



(b) Compartment 5C

Fig. 11. Deformed shape due to fire.

	<b>Member Size</b>	<b>Case 1, kips</b>	<b>Case 2, kips</b>	<b>Case 3, kips</b>
<b>Beams</b>	W14×22 (CL)	0	45	36
	W14×22 (INF)	0	5	1
	W18×35	0	84	68
	W18×60	0	93	76
	W21×93	0	210	170
<b>Columns</b>	W12×58	404	404	404
	W14×99	232	278	271
	W14×109 (E)	212	292	288
	W14×109 (C)	103	61	67

	<b>Member Size</b>	<b>Case 1, kip-ft</b>		<b>Case 2, kip-ft</b>		<b>Case 3, kip-ft</b>	
		$M_x$	$M_y$	$M_x$	$M_y$	$M_x$	$M_y$
<b>Beams</b>	W14×22 (CL)	69	—	84	—	101	—
	W14×22 (INF)	69	—	68	—	69	—
	W18×35	186	—	211	—	228	—
	W18×60	95	—	375	—	243	—
	W21×93	55	—	403	—	253	—
<b>Columns</b>	W12×58	0	—	89	41	58	26
	W14×99	24	—	186	192	96	155
	W14×109 (E)	23	—	344	334	191	228
	W14×109 (C)	28	1	866	344	626	277

these columns from experiencing thermal expansion. The gravity connections, in reality, provide some amount of rotational restraint. This restraint is relatively minor, however, and can be ignored in the simple method of analysis for typical buildings. The only other scenario where Case 2 does not cause an increase in column axial load is for the corner column in compartment 5A; this column actually experiences a reduction in axial loading due to the moment connection at column line B-4 and the pinned connection at column line A-4.

Case 3 incorporates a reduced modulus of elasticity, which results in a reduction in axial loading of the members. This is explained by Equation 2, which shows that axial load due to thermal expansion is a function of the modulus of elasticity of the member.

### **Flexural Demands**

Table 8 provides the resulting flexural demands from the SAP2000 model for compartment fires at 5A for each of the three model cases. The flexural beam demands are the

result of gravity loading and thermal gradient. The beams and girders along the column lines experience higher demands than the infill beams due to increased restraint at these locations. Flexural demands are also very high in the moment frame columns and beams due to the elevated temperatures.

### **Axial Member Design Strength**

AISC *Specification* Chapter E is used to calculate the design strength of compression members. In lieu of Equation E3-2, however, the following flexural buckling equation should be used (Appendix 4, Equation A-4-2):

$$F_{cr}(T) = \left[ 0.42 \sqrt{\frac{F_y(T)}{F_c(T)}} \right] F_y(T) \quad (4)$$

The designer should consider using a modified slenderness ( $L/r$ ) value in order to account for the rotational restraints provided by the cooler columns above and/or below the compartment fire. Consideration must be made,

**Table 9. Member Axial Design Strength**

	Member Size	A, in. <sup>2</sup>	$\phi P_n = 0.9F_y(T)A$ , kips		
Beams	W14×22	6.49	126		
	W18×35	10.3	348		
	W18×60	17.6	530		
	W21×93	27.3	916		
	Member Size	$L_c/r$	$F_e(T)$ , ksi	$F_{cr}(T)$ , ksi	$\phi P_n$ , kips
Columns (pinned-pinned)	W12×58	57.4	49.1	18.3	281
	W14×99	39.4	112	24.8	649
	W14×109	39.2	121	26.6	766
	Member Size	$L_c/r$	$F_e(T)$ , ksi	$F_{cr}(T)$ , ksi	$\phi P_n$ , kips
Columns (rotational restraint)	W12×58	35.8	130	24.8	379
	W14×99	22.1	356	31.3	820
	W14×109	22.9	355	33.2	956

however, to evaluate the likelihood of multistory fires or vertically moving fires that would compromise this assumption of rotational restraints. If deemed applicable, the calculated column design strength can be significantly improved using the modified slenderness. The modified  $L/r$  value, referred to as  $L_c/r$ , is defined as:

$$\left(\frac{L_c}{r}\right)_T = \left(1 - \frac{T - 32}{n \cdot 3,600}\right) \left(\frac{L_c}{r}\right) - \left(\frac{35}{n \cdot 3,600}\right) (T - 32) \geq 0 \quad (5)$$

where  $T$  is the column temperature (°F). If the columns above and below are both cooler,  $n = 1$ , and  $n = 2$  if either the columns above or below are cooler. This slenderness equation was calibrated for gravity columns and is provided in AISC *Specification* Commentary Equation C-A-4-9. It can also be used for moment frame columns, though this equation is overly conservative for moment frame columns due to the additional benefit of the restraint from the fixed beam to column connections.

Due to thermal expansion, beams may also experience significant compression. The beam can be considered fully braced along its top flange due to the presence of the composite slab, so flexural buckling equations need not be analyzed. Instead, the beam has the following axial nominal strength:  $P_n = F_y(T)A$ , where  $A$  is the cross-sectional area of the steel member. The same resistance factor,  $\phi$ , is used for both ambient and elevated temperature conditions. Member axial design strengths are shown in Table 9.

### Flexural Member Design Strength

All beams were designed as composite beams. Although the moment frame beams (W18×60 and W21×93) were initially designed as noncomposite members to resist lateral loads, it

was presumed that enough studs are present to enable composite action under gravity and fire loading.

### Composite Beams

The composite beams were designed assuming a constant temperature between the bottom flange and the mid-depth of the web with a 25% linear reduction from the mid-depth to the top flange, as shown in Figure 10. Appendix 4 allows two approaches for calculating the flexural strength of composite beams: (1) calculate the nominal flexural strength of the beam at ambient conditions and apply a retention factor,  $r(T)$ , per Table A-4.2.4 or (2) design using Chapter I with reduced yield stresses in the steel. Results from both approaches are in Table 10 and produce very comparable flexural strengths. The composite beams were designed for ambient conditions using ¾-in.-diameter studs and a minimum of 25% composite action. Lightweight concrete (110 lb/ft<sup>3</sup>) with 3.5 ksi compressive strength was assumed for the slab on metal deck. The nominal flexural strengths were calculated using plastic stress distribution method from Section I1.2a of the *Specification*.

### Noncomposite Members

The flexural strength of the columns was determined using the non-composite flexural equations from Appendix 4. These design equations for the nominal flexural strength of members at elevated temperatures pertain to the yielding and lateral-torsional buckling limit states. They apply only to laterally unbraced doubly symmetric members that do not have slender elements. This approach applies modified equations from AISC *Specification* Chapter F. The steel properties at elevated temperatures from Section 4.2.3b



**Table 10. Composite Beam Flexural Strength**

Member Size	$r(T)$	Number of Studs, $n$	$\phi M_n = 0.90M_n$ , kip-ft	Approach 1: $\phi M_n(T) = 0.90r(T)M_n$ , kip-ft	Approach 2: $\phi M_n(T) = 0.90M_n(T)$ , kip-ft
W14×22	0.55	20	231	127	125
W18×35	0.60	44	490	294	304
W18×60	0.72	26	664	478	450
W21×93	0.73	22	1026	750	750

**Table 11. Column Flexural Strength,  $\phi M_n$**

	Member Size	$\phi M_{n,x}$ , kip-ft	$\phi M_{n,y}$ , kip-ft
Column	W14×99	548	265
	W14×109	651	314
	W12×58	260	98

replace the ambient properties in Chapter F. When the unbraced length,  $L_b$ , of the member falls within the inelastic lateral-torsional buckling range [i.e., when  $L_b < L_r(T)$ , where  $L_r(T)$  is the limiting unbraced length for inelastic lateral-torsional buckling], the nominal flexural strength can be calculated using Appendix 4, Equation A-4-3:

$$M_n(T) = C_b \left\{ M_r(T) + [M_p(T) - M_r(T)] \left[ 1 - \frac{L_b}{L_r(T)} \right]^{c_x} \right\} \leq M_p(T) \quad (6)$$

where  $C_b$  is the lateral-torsional buckling modification factor. The other terms are defined as:

$$M_r(T) = S_x F_L(T) \quad (7)$$

$$F_L(T) = F_y (k_p - 0.3k_y) \quad (8)$$

$$M_p(T) = Z_x F_y(T) \quad (9)$$

$$c_x = 0.6 + \frac{T}{250} \leq 3.0 \text{ where } T \text{ is in } ^\circ\text{C} \quad (10)$$

and where  $S_x$  and  $Z_x$  are the elastic and plastic section moduli taken about the  $x$ -axis, respectively;  $k_p$  and  $k_y$  are retention factors for material properties at elevated temperatures and determined from AISC *Specification* Appendix 4, Table 4.2.1.

Table 11 provides the flexural strengths of the columns for the governing limit state. Note that because the W14×99 has a noncompact flange, flange local buckling (FLB) should also be checked. However, there is not yet guidance

in Appendix 4 on how to apply FLB to flexural members using the simple method of analysis, so FLB was not analyzed. The columns experience reverse curvature bending under fire loading; values of  $C_b = 2.2$  and  $2.16$  were calculated for the moment frame and gravity columns, respectively, using AISC *Specification* Equation F1-1. Due to the high  $C_b$  factors, yielding controlled the flexural strength.

#### Combined Force Member Interaction

The beams and columns in compartment 5A were subjected to axial and flexural demands, which required beam-column analyses. Each member was analyzed for combined axial and flexural forces using AISC *Specification* Chapter H, which implements an interaction check in Equations H1-1a and H1-1b. These equations are conservative for biaxial bending; to achieve interaction values closer to unity, alternative approaches outlined in the commentary of the *Specification* can be used instead to evaluate member adequacy. Table 12 summarizes the loads and strengths, as well as the interaction for all members within the compartment. The highlighted members are inadequate designs according to Equations H1-1a and H1-1b; these include the gravity column and all three moment frame columns. Design of the beam members were found to be adequate using the simple method of analysis.

It is presumed that the high demands on the moment frame columns are due in large part to the simplified modeling assumptions in the SAP2000 model. The composite slab is not incorporated in the model, so the stiffness of the moment frame beams in the model is less than what would realistically be present. Because of this, the moment frame columns carry very large moments. Additionally, the

**Table 12. Beam-Column Interaction Check**

		$P_u$ , kips	$\phi P_n$ , kips	$P_u/\phi P_n$	$M_x$ , kip-ft	$M_y$ , kip-ft	$\phi M_{n,x}$ , kip-ft	$\phi M_{n,y}$ , kip-ft	Interaction Check (H1-1a/b)
Beams	W14×22 (CL)	36	126	0.39	101	—	127	—	0.99
	W14×22 (INF)	1	126	0.03	69	—	127	—	0.55
	W18×35	68	348	0.22	228	—	304	—	0.85
	W18×60	76	530	0.18	243	—	450	—	0.61
	W21×93	170	916	0.22	253	—	750	—	0.43
Columns	W12×58*	404	379	1.07	58	26	260	98	1.50
	W14×99	271	820	0.34	96	155	462	247	1.04
	W14×109 (E)	288	956	0.32	191	228	561	314	1.21
	W14×109 (C)	67	956	0.06	626	277	561	314	1.88

\* If using a reduced axial demand due to LLR, the interaction check is 1.35.

**Table 13. Member Axial Demand vs. Design Strength Summary for Simple Method (Model Case 3)**

	Demand, $P_u$ , kips		Design Strength, $\phi P_n$ , kips		$P_u/\phi P_n$	
Beams	W14×22 (CL)	36	126		0.29	
	W14×22 (INF)	1	126		0.01	
	W18×35	68	348		0.20	
	W18×60	76	530		0.14	
	W21×93	170	916		0.19	
	<b>Member Size</b>	<b>5A</b>	<b>Pin-Pin</b>	<b>Rotational Restraint</b>	<b>Pin-Pin</b>	<b>Rotational Restraint</b>
Columns	W12×58	404	281	379	1.44	1.07
	W14×99	271	649	820	0.42	0.33
	W14×109 (E)	288	766	956	0.38	0.30
	W14×109 (C)	67	766	956	0.09	0.07

columns were evaluated without live load reduction, which results in larger demands on the columns. The gravity framing connections were also modeled as idealized pins, which do not transfer any moments. In reality, these connections have some level of rotational restraint that could help to redistribute large forces due to elevated temperatures. Each of the previously mentioned limitations of the simple method make this method overly conservative for moment frame columns and, therefore, unfavorable relative to the prescriptive method.

**Axial Demand vs. Design Strength**

A comparison of axial demand versus design strength, provided in Table 13, shows adequate strength for the beams

and moment frame columns, but inadequate strength for the W12×58 gravity column. Incorporating rotational restraint in the calculation of column design strength provides a much closer approximation to the demands than considering a pin-pin column; however, both approaches indicate column failure within 1 hr of the start of the design fire. However, the column was designed without live load reduction, which would have resulted in a demand less than the calculated design strength.

**Comparison of Methods**

Table 14 summarizes a comparison between member demands using the advanced method of analysis (ABAQUS, noted as ABQ) and the simple method (SAP2000, noted as

**Table 14. Comparison of Member Demands Between Advanced and Simple Methods**

	Member Size	Axial Load, kips		$M_x$ , kip-ft		$M_y$ , kip-ft		$V_x$ , kips		$V_y$ , kips	
		ABQ	SAP	ABQ	SAP	ABQ	SAP	ABQ	SAP	ABQ	SAP
Beams	W14×22 (CL)	50	36	58	101	2	0	12	11	5	0
	W14×22 (INT)	9	1	55	69	3	0	7	11	3	0
	W18×35	110	68	107	228	5	0	41	23	7	0
	W18×60	85	76	268	243	16	—	27	23	4	3
	W21×93	157	170	399	253	17	—	15	14	5	3
Columns	W12×58	422	404	61	58	17	26	13	8	13	2
	W14×99	299	271	46	96	106	155	8	16	21	26
	W14×109 (E)	285	288	161	191	188	228	26	35	31	38
	W14×109 (C)	46	67	496	626	178	277	88	111	48	50

SAP). The highlighted portions show differences between the modeling approaches of more than 15% or 15 kips (or kip-ft). Shear demands and capacities were also considered in these analyses but have not been presented for brevity. However, the summarized comparison of shear demands is also given in Table 14. SAP2000 typically resulted in larger demands than ABAQUS, though this was not always the case. The comparison shows close agreement between the axial forces in the members but varied results for the moment demands. In the gravity beams, SAP2000 tended to result in larger midspan moments because the ends were modeled as idealized pins, whereas the ABAQUS model incorporated some rotational restraint at the connections. SAP2000 also resulted in much larger moment demands on the columns than what was determined from the advanced analysis. As mentioned previously, this is likely due to the fact that the composite slab is not modeled in SAP2000. If the composite slab model was included in the simple analysis, the deviations in the predicted results relative to the advanced method would likely be greatly minimized. However, the advantage of the simple method is its speed and ease of modeling. If the designer were to begin incorporating composite slab behavior and catenary action into their simple analyses, then perhaps it would be more logical to employ the advanced analysis method.

It should also be noted that the temperature gradients used in the simple and advanced models for composite beams are different. The simple method utilizes an approach that is generally more conservative by only considering a 25% reduction in temperature at the top flange. In the advanced method of analysis, the reductions in temperature along the beam depth are typically greater. The differences in demand due to these thermal gradient differences can certainly contribute to the differential in the results. However,

there are many other differences that also contribute, such as connection behavior, slab continuity, etc.

### CONCLUSIONS

This work provides a comparison of the prescriptive, simple, and advanced methods of analysis, articulated through use of a case study building. It also proposes an approach for determining demands in the simple method of analysis through 3D modeling of the steel structural members in SAP2000. Member demands from elevated temperatures in the simple method can be determined by applying member temperatures and incorporating the coefficient of thermal expansion and reduced stiffness properties for the heated members. Variations in member demands were observed between the simple and advanced methods. These demand differences are to be expected because the simple method is an elastic analysis that overpredicts forces and uses simplifying modeling assumptions (idealized connections, no composite slab, etc.). These demand differences were deemed reasonable. The prescriptive and advanced methods demonstrated adequate performance of the structure. The simple method, however, provided more conservative results with inadequate moment frame designs for the columns. When using the simple method for checking moment frame members, the approach was even more conservative than the prescriptive method and is not suggested for this type of framing system. The findings from this particular study are not intended to imply that the use of the simple method is overly conservative in most cases. Instead, the use of the simple method may be found to be particularly advantageous and time-saving when considering gravity framing systems or when analyzing specific portions of a building structure.

## Future Needs

Code officials in the United States remain hesitant to allow alternative methods to the prescriptive method for design of structural members for fire conditions. Thus, it is imperative that the designer work closely with the building owner and code officials to select adequate acceptance criteria that is in accordance with the owners' wishes and building codes. Efforts are under way at a number of U.S. universities to incorporate structural design for fire conditions into the structural engineering curriculum in order to equip future structural engineers with the skills necessary to perform structural engineering analyses and design for fire.

Despite these efforts, additional research and guidance is still needed to assure safe structural designs for fire. While the simple method of analysis provides a basic approach to LRFD design for members subjected to fire, AISC *Specification* Appendix 4 requires additional guidance for checking additional limit states, particularly local buckling states as well as compressive limit states other than flexural buckling. There is also a need for more guidance on how to consider connections in the simple and advanced methods of analysis. Additionally, thermal calculations are sensitive to the temperature-dependent SFRM properties. It is, therefore, crucial to establish reliable temperature-dependent SFRM material properties. Finally, more guidance is needed to assist designers in selecting appropriate design-basis fires. General acceptance of a standard fire curve for simple and advanced methods of analysis would assist in removing ambiguity about fire load characterization.

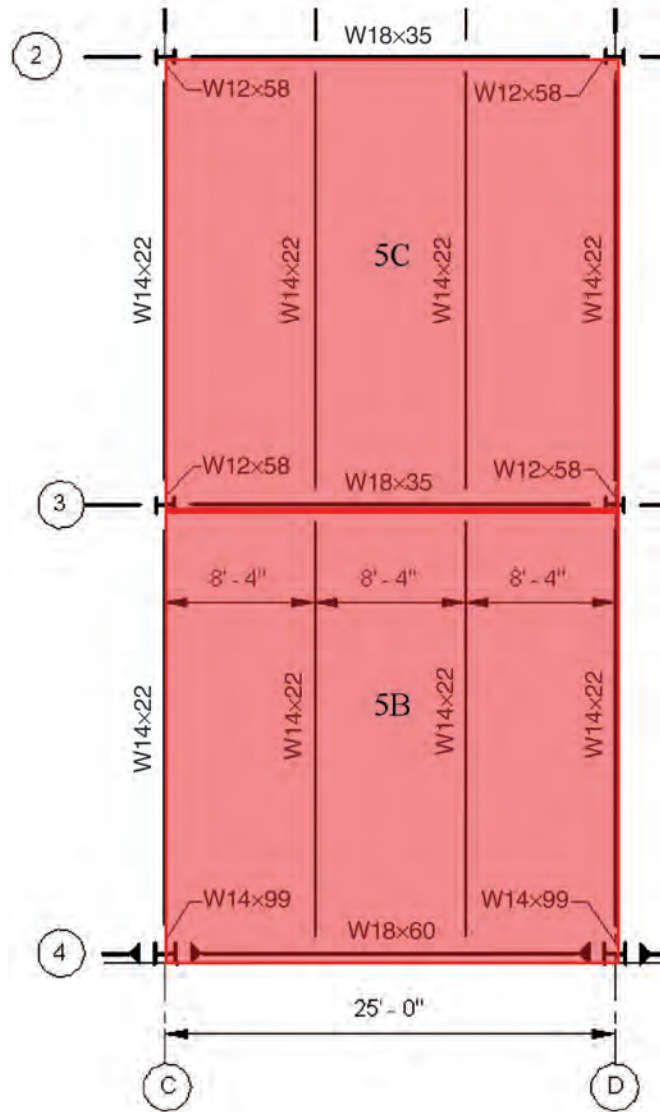
## REFERENCES

- ABAQUS (2016), Simulia, Dassault Systemes, Boston, Mass.
- Agarwal, A. (2011), "Stability Behavior of Steel Building Structures in Fire Conditions," Doctoral Dissertation, School of Civil Engineering, Purdue University, West Lafayette, Ind.
- Agarwal, A., Choe, L., and Varma, A.H. (2014), "Fire Design of Steel Columns: Effects of Thermal Gradients," *Journal of Constructional Steel Research*, Vol. 93, pp. 107–118.
- Agarwal, A. and Varma, A.H. (2014), "Fire Induced Progressive Collapse of Steel Building Structures: The Role of Interior Gravity Columns," *Engineering Structures*, Vol. 58, pp. 129–140.
- AISC (2016a), *Code of Standard Practice for Steel Buildings and Bridges*, ANSI/AISC 306-16, American Institute of Steel Construction, Chicago, Ill.
- AISC (2016b), *Specification for Structural Steel Buildings*, ANSI/AISC 360-16, American Institute of Steel Construction, Chicago, Ill.
- ASCE (2016), *Minimum Design Loads for Buildings and Other Structures*, ASCE/SEI 7-16, American Society of Civil Engineers, Reston, Va.
- ASTM (2015), *Standard Test Methods for Fire Tests of Building Construction and Materials*, ASTM E119-15, ASTM International, West Conshohocken, Pa.
- Carino, N.J., Starnes, M.A., Gross, J.L., Yang, J.C., Kukuck, S., Prasad, K.R., and Bukowski, R.W. (2005), "Federal Building and Fire Safety Investigation of the World Trade Center Disaster: Passive Fire Protection," NIST NCSTAR 1-6A, National Institute of Standards and Technology, Gaithersburg, Md, September.
- Cedeno, G., Varma, A.H., and Gore, J. (2008), "Predicting the Standard Fire Behavior of Composite Steel Beams," in *Composite Construction in Steel and Concrete VI*, Engineering Conferences International, Colorado, pp. 642–656, ASCE, Reston, Va. [http://dx.doi.org/10.1061/41142\(396\)53](http://dx.doi.org/10.1061/41142(396)53)
- Choe, L., Agarwal, A., and Varma, A.H. (2016), "Steel Columns Subjected to Thermal Gradients from Fire Loading: Experimental Evaluation," *Journal of Structural Engineering*, Vol. 142, No. 7.
- CSI (2018), *SAP2000: Integrated Software for Structural Analysis and Design*, Computers and Structures, Inc., Berkeley, Calif.
- ECCS Technical Committee 3 (1995), *Fire Resistance of Steel Structures*, ECCS Publication No. 89, European Convention for Constructional Steelwork, Brussels, Belgium.
- ECCS Technical Committee 3 (2001), *Model Code on Fire Engineering*, ECCS Publication No. 111, European Convention for Constructional Steelwork, Brussels, Belgium.
- CEN (2002), *Eurocode 1: Actions on Structures, Part 1-2: General Actions—Actions on Structures Exposed to Fire*, EN1991-1-2, European Committee for Standardization, Brussels, Belgium.
- Fischer, E.C., Chicchi, R., and Choe, L. (2021), "Review of Research on the Fire Behavior of Simple Shear Connections," *Fire Technology*, Vol. 57, pp. 1,519-1,540.
- Fischer, E.C., Varma, A.H., and Agarwal, A. (2019), "Performance-Based Structural Fire Engineering of Steel Building Structures: Design-Basis Compartment Fires," *Journal of Structural Engineering*, Vol. 145, No. 9.
- Gernay, T. and Khorasani, N.E. (2020), "Recommendations for Performance-Based Fire Design of Composite Steel Buildings Using Computational Analysis," *Journal of Constructional Steel Research*, Vol. 166.
- ICC (2018), *International Building Code*, IBC 2018, International Code Council, Falls Church, Va.

- ISO (2015), *Fire Resistance Tests—Elements of Building Construction—Part 1: General Requirements*, ISO 834-1:1999, International Organization for Standardization, Geneva, Switzerland.
- Khorasani, N.E., Gernay, T., and Fang, C. (2019), “Parametric Study for Performance-Based Fire Design of US Prototype Composite Floor Systems,” *Journal of Structural Engineering*, ASCE, Vol. 145, No. 5.
- Kodur, V.K.R., and Shakya, A.M. (2013), “Effect of Temperature on Thermal Properties of Spray Applied Fire Resistant Material,” *Fire Safety Journal*, Vol. 61, pp. 314–323.
- Main, J.A. and Sadek, F. (2013), “Robustness of Steel Gravity Frame Systems with Single-Plate Shear Connections,” NIST Technical Note 1749, National Institute of Standards and Technology, Gaithersburg, Md. <http://dx.doi.org/10.6028/NIST.TN.1749>
- NFPA (2020), *Standard for Determination of Fire Loads for Use in Structural Fire Protection Design*, NFPA 557, National Fire Protection Association, Quincy, Mass.
- NIST (2013), *Fire Dynamics Simulator Users Guide*, 6th Ed., National Institute of Standards and Technology, Gaithersburg, Md. <http://fire.nist.gov/fds/>
- Ruddy, J.L., Mario, J.P., Ioannides, S.A., and Alfawakhiri, F. (2003), *Fire Resistance of Structural Steel Framing*, AISC Design Guide 19, American Institute of Steel Construction, Chicago, Ill.
- Sarraj, M. (2007), “The Behaviour of Steel Fin Plate Connections in Fire,” Doctoral Dissertation, Department of Civil and Structural Engineering, The University of Sheffield, Sheffield, UK.
- Takagi, J. and Deierlein, G.G. (2007), “Collapse Performance Assessment of Steel-Framed Buildings under Fires,” Report No. 163, The John A. Blume Earthquake Engineering Center, Stanford University, Stanford, Calif.
- UL (2018), “UL Online Certifications Directory: Fire-Resistance Ratings—ANSI/UL263.” <http://database.ul.com/>
- Yang, K.C., Chen, S.J., and Ho, M.C. (2009), “Behavior of Beam-to-Column Moment Connections under Fire Load,” *Journal of Constructional Steel Research*, Vol. 65, No. 7, pp. 1,520–1,527.

APPENDIX

5B AND 5C ANALYSES



**Table A.1. Member Axial Demands Using the Simple Method**

		5B			5C		
	Member Size	Case 1, kips	Case 2, kips	Case 3, kips	Case 1, kips	Case 2, kips	Case 3, kips
Beams	W14×22 (column line)	0	46	37	0	47	40
	W14×22 (infill)	0	4	3	0	3	2
	W18×35	0	112	94	0	111	94
	W18×60	0	250	213	—	—	—
	W21×93	—	—	—	—	—	—
Columns	W12×58	404	404	404	404	404	404
	W14×99	209	250	248	—	—	—
	W14×109 (E)	—	—	—	—	—	—
	W14×109 (C)	—	—	—	—	—	—

**Table A.2. Member Axial Demand vs. Design Strength Summary**

		Demand, kips		Design Strength, kips	
	Member Size	5B	5C		
Beams	W14×22 (column line)	37	62	126	
	W14×22 (infill)	3	3	126	
	W18×35	94	81	348	
	W18×60	213	—	530	
	W21×93	—	—	916	
	Member Size	5B	5C	Pin-Pin	Rotational Restraint
Columns	W12×58	404	404	281	379
	W14×99	248	—	649	820

**Table A.3. Member Flexural Demands: 5B**

		Case 1, kip-ft		Case 2, kip-ft		Case 3, kip-ft	
	Member Size	$M_x$	$M_y$	$M_x$	$M_y$	$M_x$	$M_y$
Beams	W14×22 (CL)	69	—	89	—	112	—
	W14×22 (INT)	69	—	68	—	68	—
	W18×35	186	6	215	5	248	4
	W18×60	67	—	267	18	164	11
Columns	W12×58	5	—	190	46	135	29
	W14×99	14	4	448	163	285	138

**Table A.4. Member Flexural Demands: 5C**

		Case 1, kip-ft		Case 2, kip-ft		Case 3, kip-ft	
	Member Size	$M_x$	$M_y$	$M_x$	$M_y$	$M_x$	$M_y$
Beams	W14×22 (CL)	69	—	89	—	106	—
	W14×22 (INT)	69	—	68	—	67	—
	W18×35	186	—	224	2	248	1
Columns	W12×58	6	—	190	42	135	30

**Table A.5. Member Demands Comparison (ABQ = ABAQUS Results, SAP = SAP2000 Results): 5B**

	Member Size	Axial Load, kips		$M_x$ , kip-ft		$M_y$ , kip-ft		$V_x$ , kips		$V_y$ , kips	
		ABQ	SAP	ABQ	SAP	ABQ	SAP	ABQ	SAP	ABQ	SAP
Beams	W14×22 (CL)	49	37	38	112	4	—	13	12	4	0
	W14×22 (INT)	14	3	27	68	2	—	11	11	2	0
	W18×35	115	94	103	248	4	4	24	23	3	1
	W18×60	276	213	76	164	5	11	16	12	5	4
Columns	W12×58	422	404	72	135	14	29	14	16	4	2
	W14×99	261	248	194	285	116	138	37	41	21	19

**Table A.6. Member Demands Comparison (ABQ = ABAQUS Results, SAP = SAP2000 Results): 5C**

	Member Size	Axial Load, kips		$M_x$ , kip-ft		$M_y$ , kip-ft		$V_x$ , kips		$V_y$ , kips	
		ABQ	SAP	ABQ	SAP	ABQ	SAP	ABQ	SAP	ABQ	SAP
Beams	W14×22 (CL)	55	40	39	106	1	—	11	11	4	0
	W14×22 (INT)	29	2	31	67	1	—	12	11	4	0
	W18×35	124	94	108	248	4	1	24	21	3	0
Columns	W12×58	420	404	69	135	21	30	14	16	6	3

**Table A.7. Interaction Checks: 5B**

		$P_u$ , kips	$\phi P_n$ , kips	$P_u/\phi P_n$	$M_x$ , kip-ft	$M_y$ , kip-ft	$\phi M_{n,x}$ , kip-ft	$\phi M_{n,y}$ , kip-ft	Interaction Check (H1-1a/b)
Beams	W14×22 (CL)	37	126	0.29	112	—	127	—	1.08
	W14×22 (INF)	3	126	0.02	68	—	127	—	0.55
	W18×35	94	348	0.27	248	—	304	—	1.0
	W18×60	213	530	0.40	164	11	450	—	0.91
Columns	W12×58	404	379	1.07	135	29	260	112	1.76
	W14×99	248	820	0.30	285	138	462	247	1.35

**Table A.8. Interaction Checks: 5C**

		$P_u$ , kips	$\phi P_n$ , kips	$P_u/\phi P_n$	$M_x$ , kip-ft	$M_y$ , kip-ft	$\phi M_{n,x}$ , kip-ft	$\phi M_{n,y}$ , kip-ft	Interaction Check (H1-1a/b)
Beams	W14×22 (CL)	40	126	0.32	106	—	127	—	1.06
	W14×22 (INF)	2	126	0.02	67	—	127	—	0.54
	W18×35	94	348	0.27	248	—	304	—	0.70
Columns	W12×58	404	379	1.07	135	0	228	112	1.77



# Steel-Plate Composite Wall-to-Reinforced Concrete Wall Mechanical Connection— Part 1: Out-of-Plane Flexural Strength

JUNGIL SEO, HASSAN S. ANWAR, AMIT H. VARMA, and YOONHO NAM

---

## ABSTRACT

In safety-related nuclear structures, steel-plate composite (SC) walls are often used in combination with reinforced concrete (RC) walls or foundations. Appropriate connections are required to transfer force demands from the SC walls to the RC components without the connection failure that is often associated with brittle failure mode. This paper presents a design procedure developed for mechanical connections between SC and RC walls. This procedure implements the full-strength connection design approach in ANSI/AISC N690-18, *Specification for Safety-Related Steel Structures for Nuclear Facilities* (AISC, 2018), which requires connections to be stronger than the weaker of the connected walls. This paper also presents the results from experimental and analytical investigations conducted to verify the structural performance of the full-strength SC-to-RC connection. The focus of this paper (Part 1) is on the evaluation of the performance, strength, and ductility of SC wall-to-RC wall mechanical connections subjected to out-of-plane flexure. The results include global force-displacement responses, observations on concrete crack propagation, as well as applied force-strain responses of the connection region. The experimentally observed and analytically predicted results verify the conservatism of the proposed design procedure.

**Keywords:** steel-plate composite, reinforced concrete, mechanical connection, full-strength connection design, out-of-plane moment, LS-DYNA.

---

## INTRODUCTION

A steel-plate composite (SC) wall is typically comprised of plain concrete reinforced with two steel faceplates, as shown in Figure 1. The faceplates are attached to concrete using shear connectors and connected to each other using tie bars. Shear connectors provide composite action, whereas tie bars provide structural integrity and serve as out-of-plane reinforcement. Significant experimental and analytical research has been conducted around the world on the behavior and design of SC walls over the last two decades for various force demands including in-plane shear (Ozaki et al., 2004; Lee et al., 2009; Song et al., 2014; Bhardwaj et al., 2019), out-of-plane flexure and shear (McKinley and Boswell, 2002; Foundoukos and Chapman, 2008; Hong et al., 2009; Leng et al., 2015; Sener et al.,

2015), axial compression (Takeuchi et al., 1998; Choi and Han, 2009; Zhang et al., 2020), and impact loading (Bruhl et al., 2015a; Kim et al., 2020). The results from some of the aforementioned and other research programs have been used to develop design specifications and aids such as JEAC-4618 (JEAC, 2009), KEPIC-SNG (KEA, 2010), AISC N690 (AISC, 2018), AISC Design Guide 32 (Bhardwaj and Varma, 2017), and AISC 341-16 (AISC, 2016).

Previously conducted research has proven that SC walls have superior structural performance over conventional RC walls. In addition, the recent construction of SC walls for nuclear power plants (AP1000® nuclear power plants in China and Vogtle, Georgia) and a high-rise building in Seattle (Rainier Square, utilizing composite steel-plate shear wall systems) have proven that SC walls can reduce the overall construction duration. For these reasons, SC walls are continuously gaining interest from both (1) the nuclear industry for the third generation of nuclear power plants as well as small modular reactors (SMRs) and (2) the building industry for the application to core wall of high-rise structures.

Despite their advantages and potential as an alternative to conventional reinforced concrete (RC) described earlier, it is challenging to completely replace RC structures with SC walls in an entire structure due to relatively higher material and fabrication costs as well as the designer's personal preference to use RC walls for certain applications. Therefore, there is an inevitable need for providing joints between SC walls and RC structural elements. SC

---

Jungil Seo, Research Assistant Professor, Purdue University, West Lafayette, Ind. Email: seo2@purdue.edu (corresponding)

Hassan S. Anwar, Graduate Research Assistant, Purdue University, West Lafayette, Ind. Email: hsagheer@purdue.edu

Amit H. Varma, Karl H. Kettelhut Professor and Director of Bowen Laboratory, Purdue University, West Lafayette, Ind. Email: ahvarma@purdue.edu

Yoonho Nam, Engineering Group Supervisor, Civil & Architectural Engineering Department, KEPCO E&C, Korea, yoonho.nam@gmail.com

---

Paper No. 2021-01

wall-to-RC connections can be found when (1) SC walls are connected to RC floor slabs, (2) SC walls are connected to an RC basemat, and (3) SC walls are connected to RC walls. Only the SC wall-to-RC wall connection is considered in this study because the other two connections have already been previously investigated both experimentally and analytically (Kurt, 2016; Seo and Varma, 2017c).

The design demands need to be transferred properly from one structure to the other structure through the connection region so that the maximum benefits of SC walls can be achieved. Connecting SC and RC walls can be achieved using noncontact lap splice or mechanical connections. Multiple curtains of large reinforcement (in diameter) are typically placed for RC walls subjected to higher design demands. Connecting SC walls to RC walls using the noncontact lap splicing for reinforcement bars larger than 1.4-in. diameter (#11) would require a significantly longer development length, which may not be suitable for some locations. To overcome this challenge, mechanical connection of reinforcement bars greater than 1.4-in. diameter (#11) can be considered as per ACI 349-06 (ACI, 2006).

Although ACI 349-06 (ACI, 2006) specifies the design requirements for mechanical connection of reinforcement bars in RC construction, it cannot be easily extended to SC wall-to-RC wall mechanical connections due to complex force transfer mechanisms associated with two different structural systems and lack of detailed design requirements in ANSI/AISC N690-18, *Specification for Safety-Related Steel Structures for Nuclear Facilities* (AISC, 2018), hereafter referred to as AISC N690. For these reasons, a design procedure for SC-RC mechanical connections was developed by the authors based on available and existing connection design philosophy and concepts. The procedure was evaluated experimentally and analytically, and this paper focuses on the experimental and analytical investigation of the SC-RC mechanical connections subjected to out-of-plane flexure. It presents (1) the development of the design

procedure, (2) results and observations from both experimental and analytical investigation, and (3) the validity of the design procedure.

## BACKGROUND

The typical SC wall connections to RC structures include (1) SC wall-to-RC slab, (2) SC wall-to-RC foundation, and (3) SC wall-to-RC wall. These SC wall connections can be designed based on two different connection design philosophies for SC wall connections permitted by AISC N690 (AISC, 2018), and they use both full-strength connection design philosophy and overstrength connection design philosophy. With the full-strength connection implemented, the connection is strong enough to develop the full strength (125%) of the weaker of the connected structural components. It is often associated with forming plastic hinges away from the connection region, dissipating energy during design basis seismic events. Thus, the connection philosophy is often recommended and preferred. On the other hand, with the overstrength connection implemented, the connection can be weaker than the connected structural components, but its strength is designed to be greater than or equal to 200% of the seismic demands and +100% of the nonseismic demands in the load combination.

Seo and Varma (2017b, 2019) conducted experimental and analytical investigations for SC wall-to-wall connections (T and L joints). The focus was on understanding the behavior of SC wall joints and developing design recommendations. The authors developed a connection design method for SC wall-to-wall T and L joints by implementing a full-strength connection design philosophy and recommended a design equation for the strength of SC wall joints. However, SC wall-to-RC structure connections can be difficult to design due to a complex force transfer mechanism and the absence of specific design aids and specifications.

JEAC (2009) recommends three connection techniques to transfer the forces from SC wall to RC foundation: non-contact lap splicing between foundation dowel bars and SC wall steel faceplates [technique (a)], steel faceplates of SC wall embedded into the RC foundation using shear studs [technique (b)], and steel faceplates and embedded foundation dowel bars welded to the baseplate [technique (c)]. These three techniques are shown in Figure 2. Connection techniques (a) and (c) were experimentally and analytically investigated by Kurt (2016). A total of 10 tests were conducted with aspect ratios (height/length of SC wall) from 0.60 to 1.00. The specimens were subjected to cyclic in-plane loading, and the failure of the specimens occurred as crushing of concrete and fracture of steel dowel bars. The SC wall-to-RC foundation anchorage connection technique (a) subjected to monotonic tension loading was investigated by Seo and Varma (2017a). Three full-scale specimens were

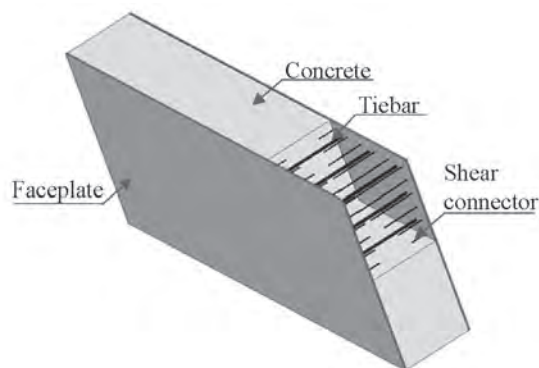


Fig. 1. Typical SC wall configuration.

designed based on a full-strength connection design philosophy. The focus was on the influence of shear reinforcement, dowel embedment length, and tie bar configuration on the axial behavior and force transfer mechanism of the SC-to-RC lap splice connection. Based on the results from this study, the authors concluded that the ductile behavior of the SC-to-RC lap splice connection can be led by developing concrete compressive struts within the connection

Researchers including Hwang et al. (2013), and Lee et al. (2012) have discussed the behavior of the SC wall-to-RC wall (L-joint) connection. For example, Hwang et al. carried out an experimental and analytical study to evaluate the strength, ductility, and failure mode of the noncontact lap splice (L-joint) connection, shown in Figure 3. The L joint exhibited ductile failure mode with yielding of vertical

reinforcement in the connection region governing the overall force-displacement behavior. Additionally, Lee et al. carried out a similar experimental program and reported flexural reinforcement pull out along with RC wall shear failure.

### DESIGN PROCEDURE

RC or SC walls in any structure are designed for seismic and nonseismic load combinations resulting in design demands. These design demands are transferred from one wall to the other through the connection region. Although AISC N690 (AISC, 2018) recommends two connection design philosophies (full-strength and overstrength), it does not provide a detailed design approach and recommendations for SC

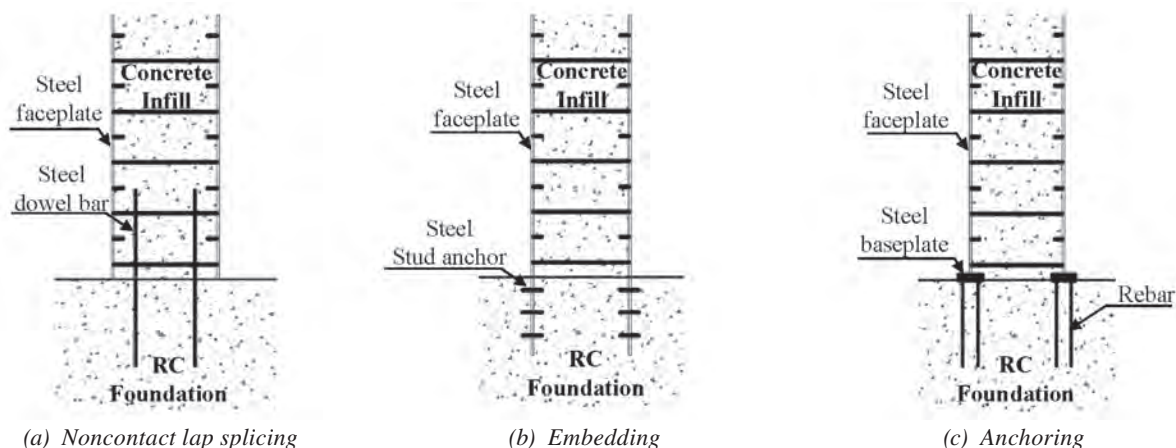


Fig. 2. Connection techniques for SC wall-to-RC foundation (Seo and Varma, 2017a).

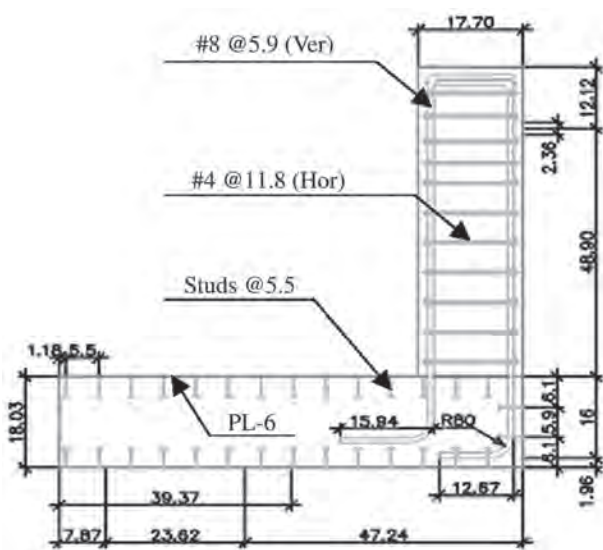


Fig. 3. SC wall-to-RC wall noncontact lap splice (L-joint) connection (units: in.) (Hwang et al., 2013).

wall-to-RC wall mechanical connections. In addition, there are no SC wall-to-RC wall mechanical connections that have been previously developed and tested. The authors have developed a design procedure for SC wall-to-RC wall mechanical connections based on the full-strength connection design philosophy.

When SC walls are implemented and connected to RC walls, these design demands must be transferred to connected structural components. Figure 4 illustrates four major design force demands on an RC wall panel section near the SC wall-to-RC wall connection, including axial tension ( $S_x$ ,  $S_y$ ), in-plane shear force ( $S_{xy}$ ,  $S_{yx}$ ), out-of-plane shear force ( $S_{xz}$ ,  $S_{yz}$ ), and out-of-plane flexural or twisting terms ( $M_x$ ,  $M_y$ ,  $M_{xy}$ ,  $M_{yx}$ ). In general,  $M_{xy}$  and  $M_{yx}$  are obtained from finite element analysis and added to  $M_x$  and  $M_y$ , respectively. In addition,  $S_x$ ,  $S_{xy}$ ,  $S_{xz}$ , and  $M_x$  are resisted by the RC and SC walls independently; therefore, these terms are not required to be transferred to the SC wall. Thus, only four force terms ( $S_y$ ,  $S_{yx}$ ,  $S_{yz}$ ,  $M_y$ ), shown in Figure 5, need to be transferred from RC wall to SC wall.  $S_y$  is the axial force in the  $y$ -direction ( $T$ ) and  $M_y$  is the out-of-plane moment (OOPM).  $S_{yx}$  and  $S_{yz}$  are the in-plane shear (IPV) and the out-of-plane shear (OOPV), respectively.

Figure 6 presents a schematic view of a typical SC wall-to-RC wall mechanical connection considered in this study. As shown, reinforcement embedded in the RC wall is extended and connected to the baseplate using mechanical

couplers. The baseplates are welded to the faceplates and the wing plates to resist the force from the rebars. The steel tie plates are placed and welded to the faceplates to provide the resistance against the tension force induced by the moment generated from the eccentricity.

Figure 7 illustrates the axial force,  $T$ , transfer through the mechanical connection from the RC wall to the SC wall. As shown, the rebar in the RC wall are extended and connected to the baseplate that is welded to both the wing plate and the faceplate of the mechanical connection. With the full-strength connection design philosophy, the maximum axial force that needs to be transferred to the SC wall is 125% of the yield strength of the reinforcing bars ( $T_1 = T_2 = T_3 = T_4 = 1.25A_{s,r}F_{y,r}$ ). This maximum axial force is referred to as the required axial tension strength,  $N_r$ , and it is equally distributed between the two faceplates. The required axial tension strength,  $N_r$ , in the rebars is transferred to the faceplates and generates the moment due to the eccentricity. The moment is resisted by concrete in compression and the tie plate in tension that connects the two faceplates.

Figure 8 illustrates the out-of-plane moment (OOPM) transfer mechanism from the RC wall to the SC wall. As shown, the OOPM is transferred to the SC wall through compression force in the concrete and tension force in the steel rebar and the faceplates. The maximum OOPM that needs to be transferred through the mechanical connection is 125% of the flexural strength of the RC wall,

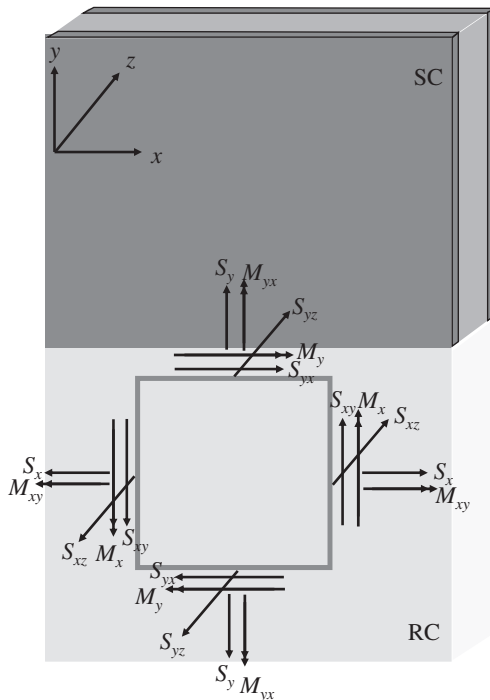


Fig. 4. Forces on RC wall panel section.

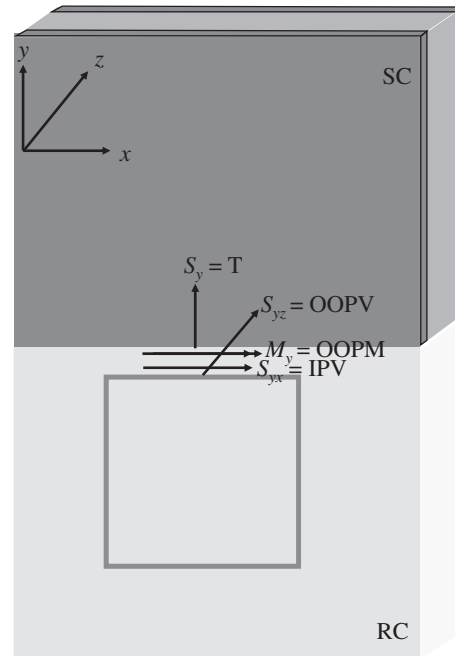


Fig. 5. Four forces on RC wall panel to be transferred to SC wall.

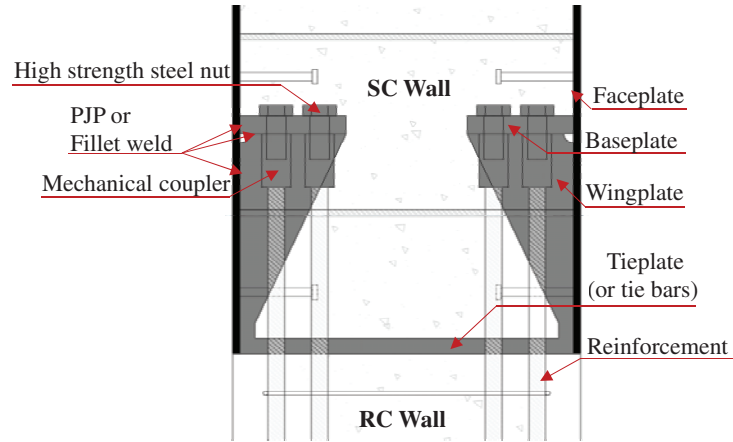


Fig. 6. Schematic of the mechanical splice connection.

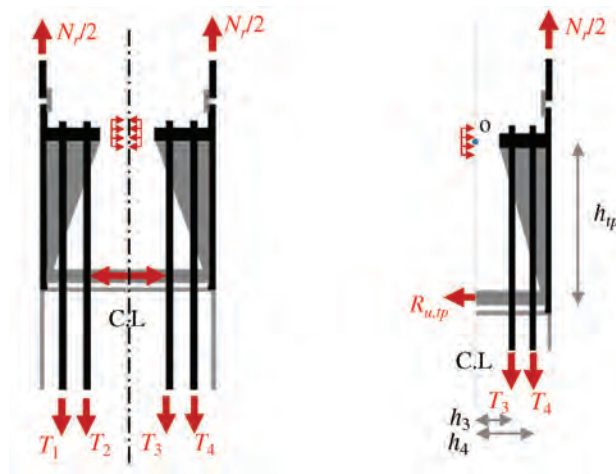


Fig. 7. Axial force transfer mechanism.

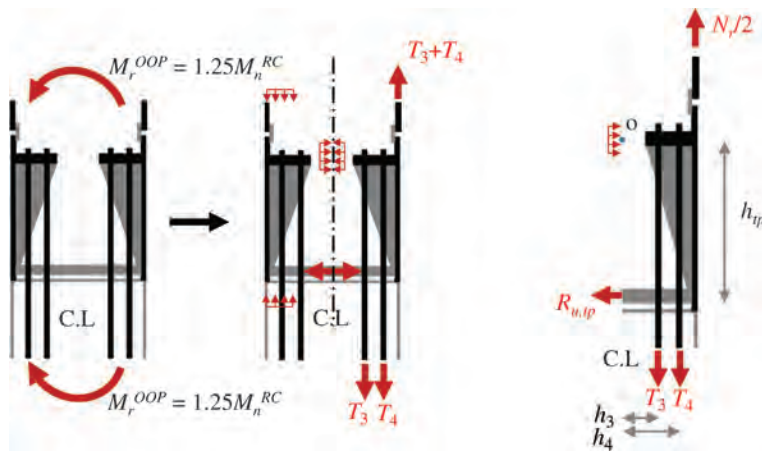


Fig. 8. Out-of-plane moment force transfer mechanism.

$M_n^{RC}$ . Thus, the required OOPM,  $M_r^{OOP}$ , is  $1.25M_n^{RC}$ . The  $M_r^{OOP}$  also generates an eccentric moment, and it is resisted by the SC wall infill concrete in compression near the baseplate, and the tensile force in the tie plate that connects the two faceplates.

For both the out-of-plane shear (OOPV) and the in-plane shear (IPV), the shear friction is the main force transfer mechanism, as shown in Figure 9. When the mechanical splice connection is subjected to either of the two shear forces, the shear transfer occurs across two planes via friction between the two concrete surfaces. The friction force is a result of the clamping forces created by the rebar keeping the two surfaces together. The maximum transferred shear force between two concrete surfaces,  $V_n^{SF}$ , is limited by the lesser of  $0.2f'_cA_c$ ,  $1600A_c$ , or  $(480 + 0.08f'_c)A_c$  according to ACI 318-19, Section 22.9.4.4 (ACI, 2019), where  $A_c$  is the area of concrete resisting shear transfer.

In general, the out-of-plane shear strength of RC walls is less than the shear friction force. Thus, the mechanical splice connection will not fail prior to the shear failure of the RC wall as long as the connection region can transfer the shear friction force. For this reason, the mechanical connection is designed based on the assumption that all the rebars connected to the connection develop 125% of their yield strength, which results in the moment due to the eccentricity induced by the required axial tension strength,  $N_r$ . Similarly, the moment is resisted by concrete near the baseplate and the tie plate that connects the two faceplates.

The design procedure developed in this study in underlying sections assumes that (1) both RC and SC walls have

been designed, (2) wall thickness of the RC wall is the same as the wall thickness of the SC wall, and (3) width of the baseplate is the same as the maximum width of the wing plate. The procedure can be generalized in three steps: (1) tie plate design, (2) baseplate design, and (3) wing plate design.

### Tie Plate (TP) Design

Designing the steel tie plate involves identifying the required axial tension force for the tie plate,  $R_{u,tp}$ . As shown in Figures 7 and 8, the magnitude of  $R_{u,tp}$  is influenced by the distance of the tie plate with respect to the baseplate,  $h_{tp}$ , and the rebar distance,  $h_3$  and  $h_4$ , with respect to the section centerline (CL). From the free-body diagrams,  $R_{u,tp}$  can be calculated by taking a moment at location  $O$ , as given in Equation 1. In the equation,  $N_r$  is the sum of  $T_1$ ,  $T_2$ ,  $T_3$ , and  $T_4$ .  $T_1$ ,  $T_2$ ,  $T_3$ , and  $T_4$  are the respective full strengths of the steel rebar ( $1.25A_{s,r}F_{y,r}$ ). In addition,  $t_{wall}$  is the wall thickness, and  $t_p$  is the faceplate thickness.

$$R_{u,tp} = \frac{\left[ \frac{N_r}{2} \left( \frac{t_{wall}}{2} - \frac{t_p}{2} \right) \right] - (T_3h_3 + T_4h_4)}{h_{tp}} \quad (1)$$

### Baseplate Design

The baseplate design can be performed using the yield line method. The yield line method is based on the bending moment of the structural element at its collapse state. The unit baseplate is subjected to two concentrated forces, equal

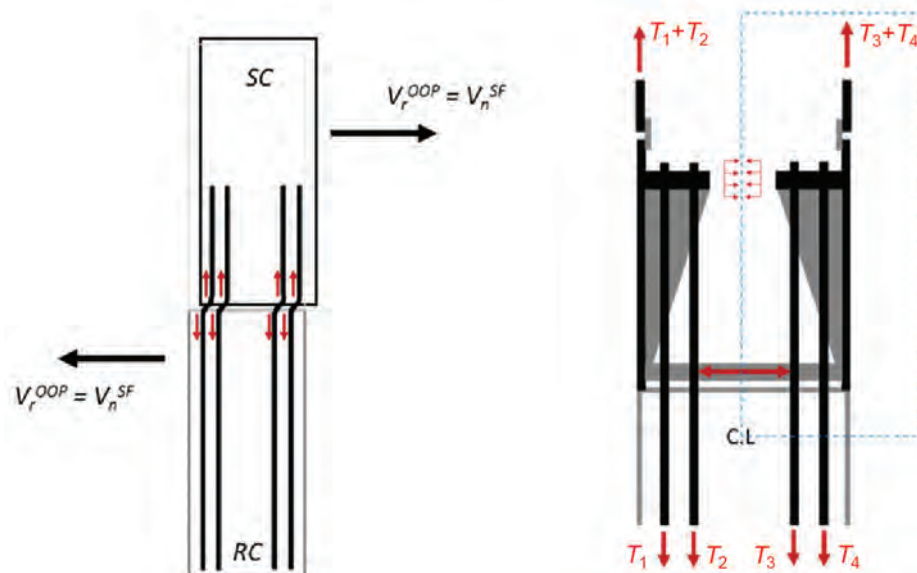


Fig. 9. Out-of-plane shear and in-plane shear force transfer mechanism.

to 125% of the yield strength of the steel rebar,  $1.25A_{s,r}F_{y,r}$ . As shown in Figure 10, the three perimeters of the unit baseplate reach their negative flexural strength,  $M_{bp}^-$ , forming yield lines  $l_4$ ,  $l_5$ , and  $l_6$ . Three additional yield lines,  $l_1$ ,  $l_2$ , and  $l_3$ , (as a result of positive flexural strength,  $M_{bp}^+$ ), are formed inside the unit baseplate connecting the concentrated forces,  $P$ , the bottom center point, and the two top corners, respectively. The spacing and thickness of the wing plate are  $S_{wp}$  and  $t_{p,wp}$ , respectively. In addition,  $W_{wp}$  is the width of the wing plate,  $S_{r1}$  is the distance of the rebar to the faceplate, and  $S_{r2}$  is the center-to-center distance between rebar. With the yield line analysis method, it is assumed that the work done by external forces,  $\Sigma W_{ext}$ , in undergoing a small deflection,  $\Delta$ , is equal to the internal work,  $\Sigma W_{int}$ , done in rotations along yield lines,  $\theta_1$  and  $\theta_2$ ; see Figure 11. Equating  $\Sigma W_{ext}$  and  $\Sigma W_{int}$  will result in the required flexural strength of the baseplate,  $M_{u,bp}$ , per unit length (1 in.). The external and internal work,  $\Sigma W_{ext}$  and  $\Sigma W_{int}$ , are given in Equations 2 and 3, and the required flexural strength,  $M_{u,bp}$ , is given in Equation 4.

$$\Sigma W_{ext} = 2P\Delta = 2(1.25A_{s,r}F_{y,r})\Delta \quad (2)$$

$$\Sigma W_{int} = \Sigma (M\theta) \quad (3)$$

$$M_{u,bp} = M = \frac{2(1.25A_{s,r}F_{y,r})\Delta}{2l_1\theta_1 + l_2(\theta_1 + \theta_2) + l_3(\theta_1 + \theta_2) + l_4\theta_1 + l_6\theta_1 + l_5\theta_2}$$

where

$$l_1 = W_{bp} - S_{r1} - 1.5d_{hole}$$

$$l_2 = l_3 = \sqrt{\left(\frac{S_{wp} - t_{p,wp}}{2}\right)^2 + (S_{r1})^2} - \frac{1}{2}d_{hole}$$

$$l_4 = l_6 = W_{bp}$$

$$l_5 = S_{wp} - t_{p,wp}$$

$$\Delta = 1$$

The minimum baseplate thickness can be calculated by equating  $M_{u,bp}$  and  $\phi M_{n,bp}$  (i.e.,  $\phi M_{n,bp} = \phi F_y Z$ ) using Equation 5.

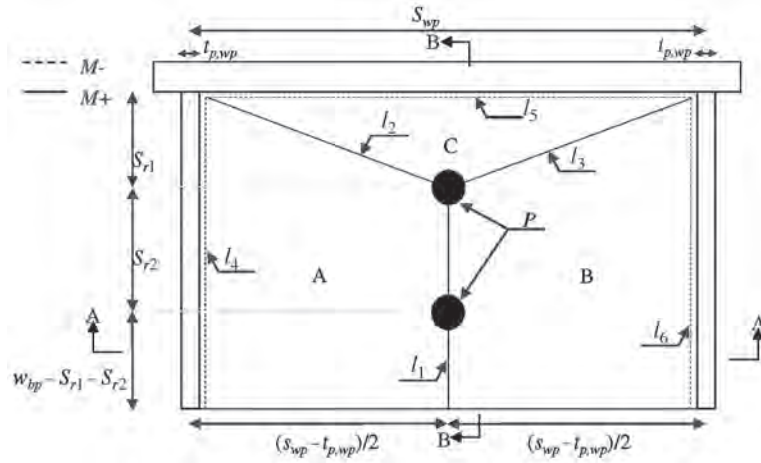


Fig. 10. Yield lines for unit baseplate.

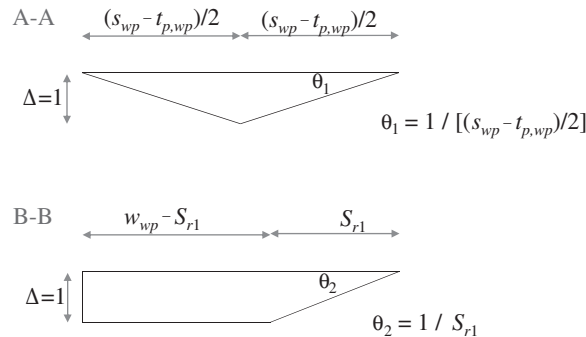


Fig. 11. Small deflection angles at section A-A and B-B.

$$t_{p, bp, min} = \sqrt{\frac{8(1.25A_{s,r}F_{y,r})}{2l_2\theta_1 + l_2(\theta_1 + \theta_2) + l_3(\theta_1 + \theta_2) + l_4\theta_1 + l_6\theta_1 + l_5\theta_2}} \Phi F_{y, bp} \quad (5)$$

where

$$Z = \frac{(1 \text{ in.})(t_{p, bp})^2}{4}$$

### Wing Plate Design

In this design process, the thickness of the wing plate is determined. Figure 12 illustrates a single wing plate that is subjected to axial compression force from four reinforcing bars located on both sides of the wing plate. As shown, the geometry of the system, as well as the loading condition, is similar to those of the triangular bracket seat in AISC Companion to the AISC Steel Construction Manual, Volume 1: Design Examples (AISC, 2019). Thus, the design process for the triangular bracket seat can be implemented for the steel wing plate if the variables  $P$ ,  $a$ , and  $b$  as shown in Figure 12(b) are replaced with  $T_1 + T_2$ ,  $h_{ip}$ , and  $W_{bp}$ , as shown in Figure 12(a), respectively. During the wing plate design process, demands and available strengths at sections A-A and B-B are calculated and compared.

## EXPERIMENTAL INVESTIGATION

The design procedure developed for SC wall-to-RC wall mechanical connections was verified experimentally. A total of seven tests (four full scale and three small scale) were conducted to evaluate the performance of the SC

wall-to-RC mechanical connections designed through the procedure. They were subjected to monotonic OOPM and OOPV and cyclic in-plane shear (IPV). In this paper, only two large specimens subjected to OOPM are discussed. The results from the remaining five specimens subjected to OOPV and IPV will be published later.

### Design of Test Matrix

The specimens were designed to depict a unit cell of a typical wall section in nuclear facilities. The typical configuration of the test specimens is shown in Figure 13. As shown, the specimens had a wall thickness,  $T_{wall}$ , and width,  $w_{wall}$ , of 36 in., with a span length,  $l_{span}$ , of 324 in. ( $9.0T_{wall}$ ). The RC wall portion had flexural reinforcement placed in four curtains, a pair along each edge, comprised of ASTM A706 (ASTM, 2016) Grade 60 #14 rebar at center-to-center spacing,  $s_{1,rc}$ , of 9 in., with a longitudinal reinforcement ratio,  $\rho_1$ , of 0.027. Shear reinforcement was comprised of ASTM A706 Grade 60 #4 double hoop stirrups at the same center-to-center spacing of 9 in. along the length of the wall. The SC wall portion of the test specimens consisted of 3/4-in.-thick, Grade 50 faceplates, resulting in a reinforcement ratio,  $\rho_2$ , of 0.04; 1-in.-diameter stud anchors at center-to-center spacing,  $s_s$ , of 9 in.; and ASTM A706 Grade 60 #8 tie bars welded with a partial-joint-penetration groove weld to faceplates at a center-to-center spacing,  $s_t$ , of 18 in. The mechanical connection region was designed using the proposed design procedure. The 27-in.-long connection region was comprised of a 2-in.-thick ( $t_{bp}$ ) and 11-in.-wide baseplate ( $w_{bp}$ ), 1-in.-thick wing plate ( $t_{wp}$ ), and a 1-in.-thick ( $t_{ip}$ ) and 1 3/4-in.-wide tie plate ( $w_{ip}$ ). All steel plates within the mechanical connection region were Grade 50.

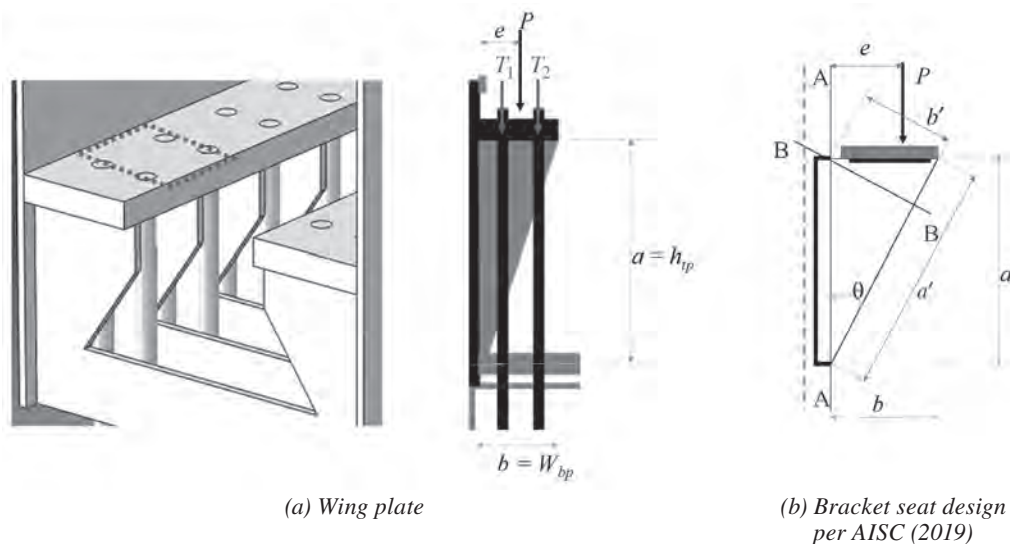


Fig. 12. Design comparison.



Table 1 presents geometric details of the test specimens. The two specimens in Table 1 are essentially identical specimens. They are only differentiated by their names as well as longitudinal rebar-to-baseplate connection plans. Figure 14 illustrates the two rebar-to-baseplate connection plans considered in this study. The coupler plan shown in Figure 14(a) utilizes a coupler that connects with the tapered threaded #14 reinforcing bar at one end. The coupler is then bolted to the baseplate using ASTM A449 (ASTM, 2020) high-strength bolts. The bolt is stronger than the connected reinforcing bar with a tensile strength,  $F_u$ , of 90 ksi and required no special tightening considerations. Similarly, the double nut plan as shown in Figure 14(b) also utilizes the

tapered threaded #14 reinforcing bar, which is connected to the baseplate using the coupler and a threaded rod.

The steel components of the two specimens were made from the same heat. The steel material properties were measured by conducting uniaxial tension tests according to ASTM E8 (ASTM, 2013). Table 2 summarizes the average measured steel material properties of the test specimens used in the study. In Table 2,  $F_y$  is the average measured 0.2% offset yield stress. The concrete material properties were measured by conducting uniaxial compression tests according to ASTM C39 (ASTM, 2014) on 4-in.-diameter concrete cylinders that were cast at the same time as the test specimens. The average measured concrete strengths at day of test for the test specimens are also presented in Table 2.

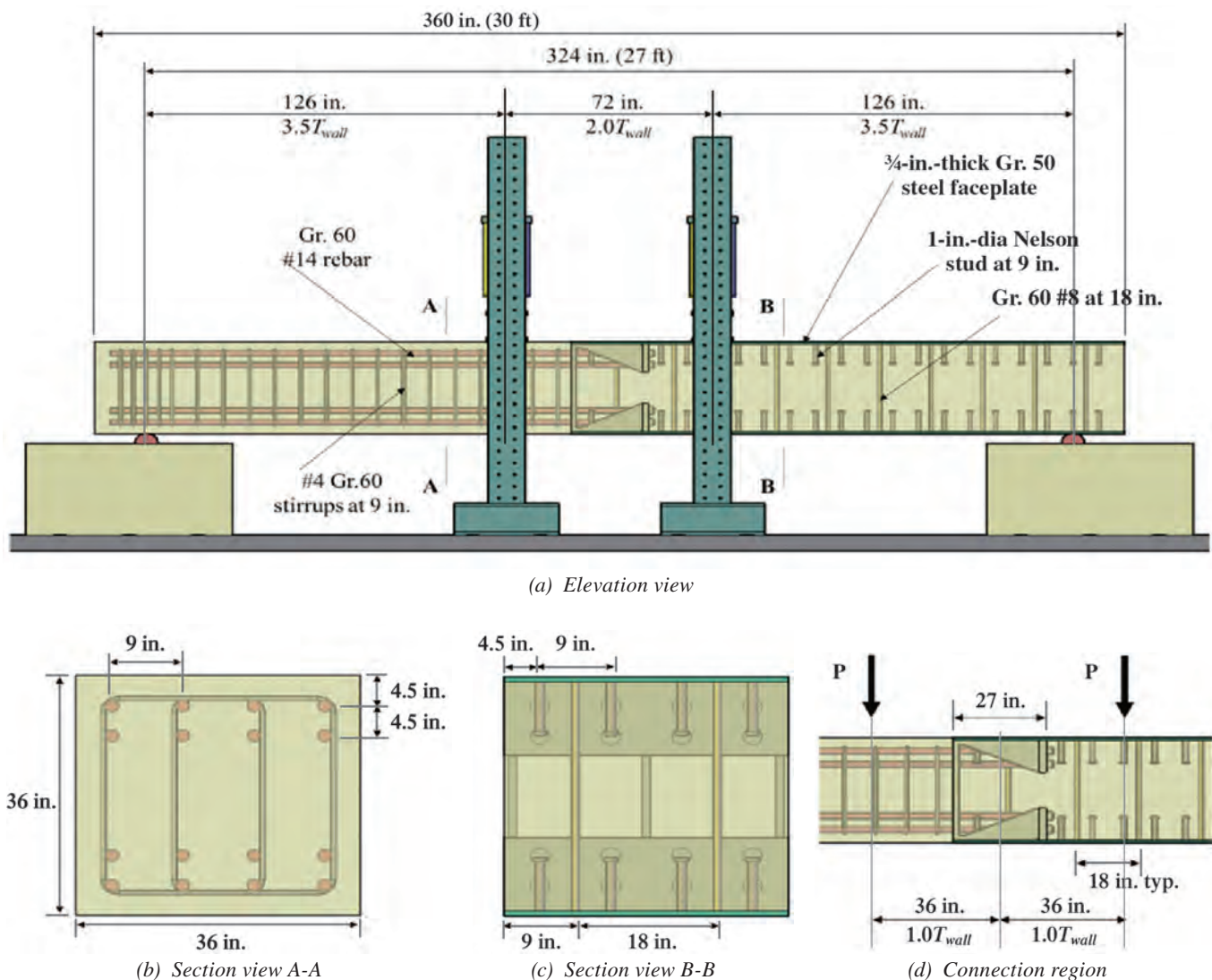


Fig. 13. OOPM test specimen.

Specimen	Overall Dimension			SC Wall				RC Wall			Connection				
	$w_{wall}$ (in.)	$l_{span}$ (in.)	$T_{wall}$ (in.)	$t_p$ (in.)	$\rho_2$	$s_s$ (in.)	$s_t$ (in.)	Rebar Size	$s_{1,rc}$ (in.)	$\rho_1$	$w_{tp}$ (in.)	$t_{tp}$ (in.)	$w_{bp}$ (in.)	$t_{bp}$ (in.)	$t_{wp}$ (in.)
OOPM-C	36	324	36	3/4	0.04	9	18	14	9	0.027	1.75	1	11	2	1
OOPM-DN	36	324	36	3/4	0.04	9	18	14	9	0.027	1.75	1	11	2	1

Specimen	Steel Yield Strength, $F_y$ , ksi						Concrete Strength, $f'_c$ , psi
	Faceplate	Baseplate	Tie Plate	Wing Plate	Rebar	Stirrup	
OOPM-C	60	62	57	57	68	67	5,447
OOPM-DN	60	62	57	57	68	67	5,470

### Instrumentation Plan

The OOPM test specimens were subjected to monotonic loading in the vertical direction, as illustrated in Figure 13. Two 500-kip hydraulic actuators were connected to the test frames to apply the monotonic loading at two locations 36 in. away from the center of the specimen.

The layout of string potentiometers (SPs) and displacement transducers (DTs) is illustrated in Figure 15. One set of two SPs were attached to the center of connection region to measure global deflection and possible twisting of the specimen. Another pair of SPs were attached to the bottom of the specimen under each loading point. Two DTs were placed under each roller support to measure support settlement. Four electrical-resistance strain gauges (SGs), each on the interior wing plates and tie plates, were attached as per the configuration shown in Figure 16. In case of baseplates, two SGs were attached, each on top and bottom baseplates at horizontal distances of 13.5 in. and 22.5 in., respectively, from the left face, as shown in Figure 17. Two SGs were attached on each #14 horizontal rebar (one at the top and one at the bottom of rebar) located at a horizontal distance of 2 in. from the mechanical coupler, making a total of 16 SGs in the specimen rebar cross section (connection region). This arrangement is illustrated in Figure 18.

### EXPERIMENTAL OBSERVATIONS AND RESULTS

#### Specimen OOPM-C

The applied force–displacement response of specimen OOPM-C is shown in Figure 19. As shown, the first concrete flexural cracks occurred in the RC wall portion at the applied force of  $P = 80$  kips, resulting in a change in the stiffness. Additionally, a significant decrease in the stiffness at  $P = 500$  kips was observed due to yielding of the bottom #14 reinforcing bars. Concrete crushing under the loading point in the RC portion was also observed at  $P = 514$  kips. The maximum applied force,  $P_{max}$ , was 585 kips, and the corresponding displacements were 6.39 in., 6.07 in., and 4.83 in. at the RC portion, center, and the SC wall portion, respectively. As expected, the maximum displacement,  $\Delta_{max}$ , was observed in the RC wall portion of the specimen (SP4). The maximum applied force,  $P_{max}$ , was greater than the force associated with the flexural strength of the RC portion calculated using ACI 349 (ACI, 2006) provisions with the measured properties ( $P_{Mn,RC} = 495$  kips) by 18%. The shear force associated with  $P_{max}$  was 293 kips ( $P_{max}/2$ ), less than the shear strength of the RC wall portion determined using ACI 349 ( $V_{n,RC} = 329$  kips), thus confirming

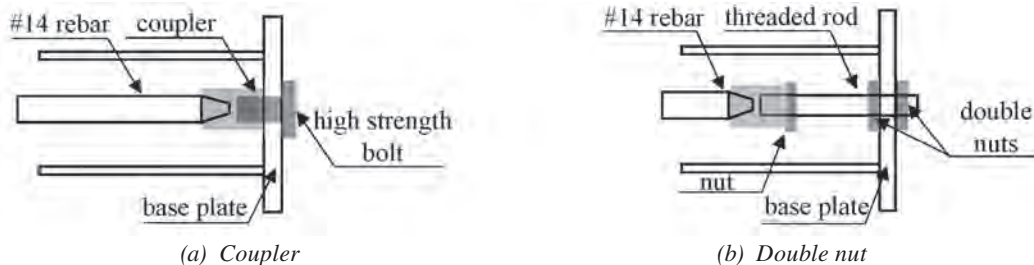


Fig. 14. Rebar to baseplate connections.

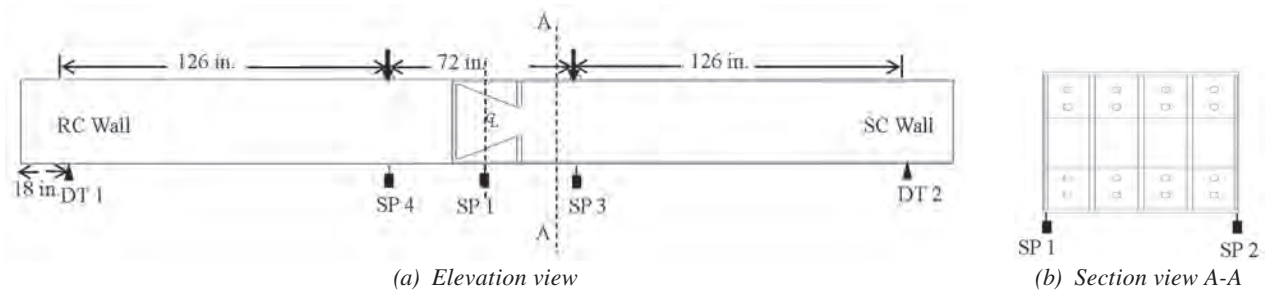


Fig. 15. SP and DT sensor layout.

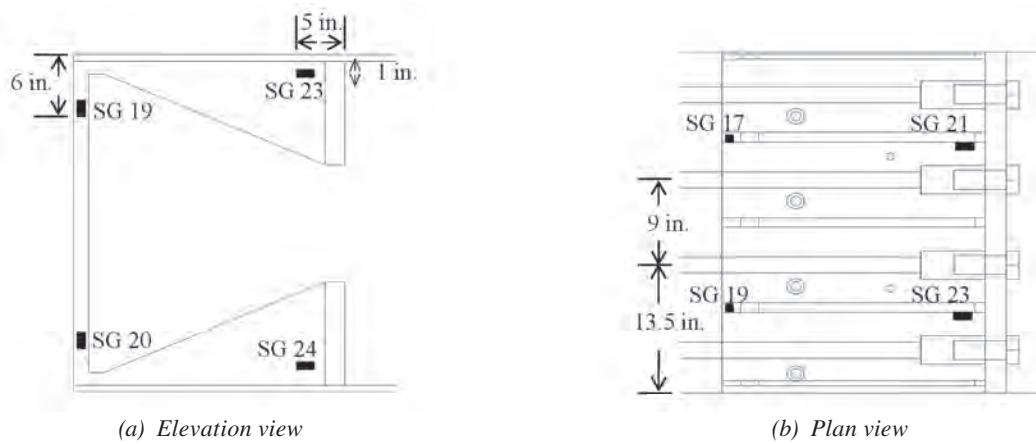


Fig. 16. SG layout of wing plates and tie plates.

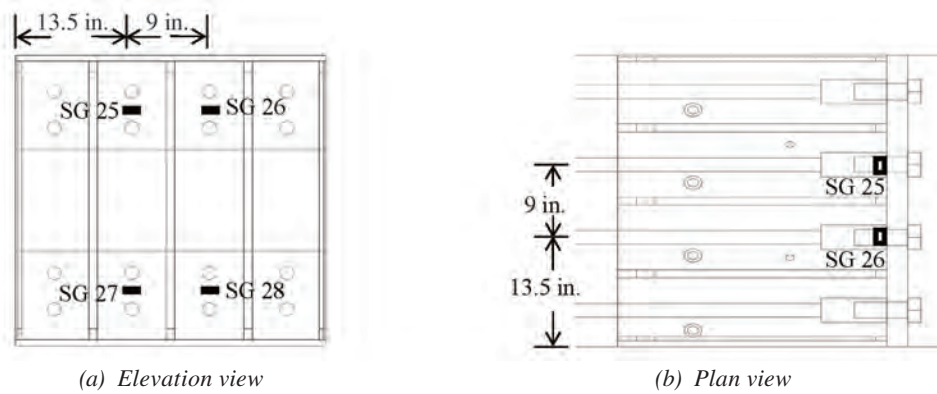


Fig. 17. SG layout of baseplates.

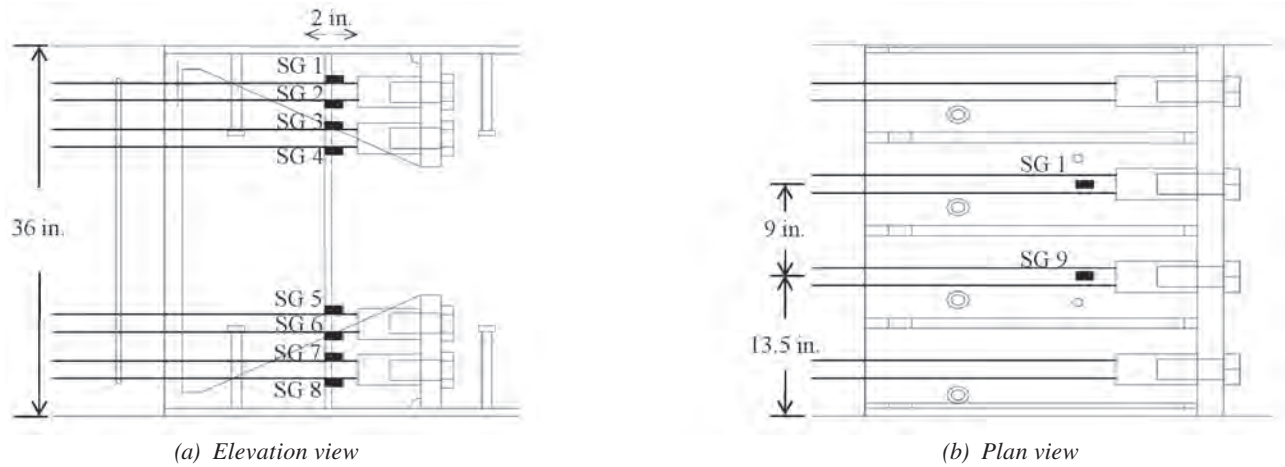


Fig. 18. SG layout for #14 rebar.

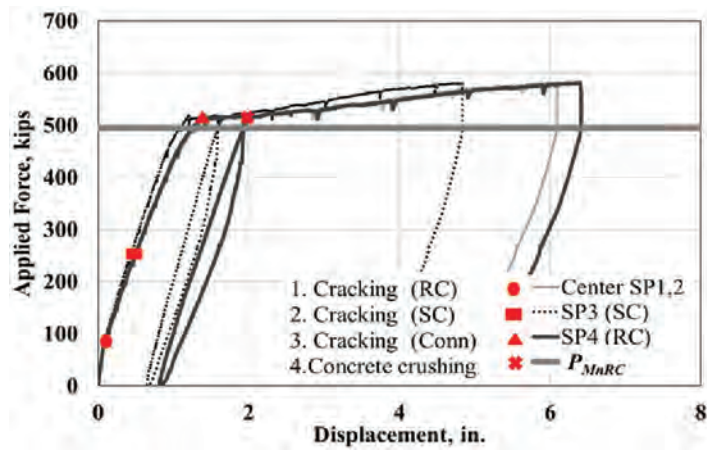


Fig. 19. Applied force–displacement response.

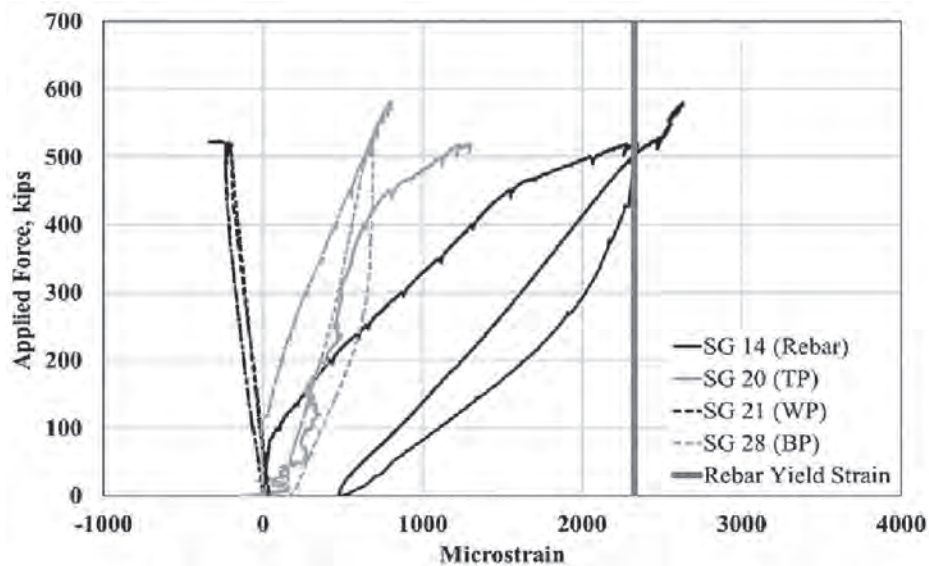


Fig. 20. Applied force–strain response of specimen OOPM-C (#14 rebar, wing plates, tie plates, and baseplates).

flexural yielding of the RC wall portion to be the governing failure mode.

Figure 20 shows the applied force–strain response for #14 rebar, wing plate, tie plate, and baseplate. The bottom #14 rebar exhibited the maximum strain of  $2,640 \mu\epsilon$  (SG 14), which was greater than the yield strain ( $\epsilon_y = 2,330 \mu\epsilon$ ). Note that the maximum strain of the #14 rebar is somewhat lower than expected because the strain gauges were attached 2 in. away from the mechanical couplers rather than being attached at the interface between the RC wall and SC wall portions. As shown, the maximum strain for wing plates and tie plates at  $P_{max}$  was  $1,440 \mu\epsilon$  (SG 20, tie plate) and  $-360 \mu\epsilon$  (SG 21, wing-plate), respectively, with corresponding stress values of 41.6 ksi and  $-10$  ksi. Lastly, a similar response of baseplates is shown in the same figure exhibiting the maximum strain of  $802 \mu\epsilon$  (SG 28) at  $P_{max}$ . As expected, all steel components in the connection region remained in the elastic range.

Figure 21 presents the overall damage progression in terms of concrete crack patterns. First flexural cracks appeared in the bottom of RC wall portion near the loading

point at 14% of  $P_{max}$ . As the loading increased, additional flexural cracks were formed within the RC wall shear span as well as in the SC wall region around 235 kips ( $0.4P_{max}$ ). The flexural cracks transformed into flexural-shear cracks at  $0.6P_{max}$ . Cracks appeared in the connection region just before the onset of concrete crushing at the RC wall portion loading point. After the yielding of the #14 rebar, the compression zone under the loading point (RC wall portion) softened as a result of concrete crushing and spalling, causing extensive ductile deformation of the test specimen, as shown Figure 22.

### Specimen OOPM-DN

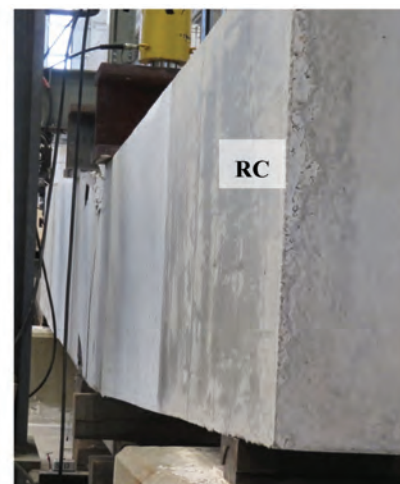
Figure 23 shows the applied force–displacement response of specimen OOPM-DN. As shown in the figure, the specimen exhibited similar behavior to that of OOPM-C. The maximum applied load was  $P_{max} = 570.8$  kips, and the corresponding displacements were 4.98 in., 4.80 in., and 3.79 in. at the RC portion, center, and the SC wall portion, respectively. The maximum vertical displacement,  $\Delta_{max}$ ,



Fig. 21. Concrete crack pattern (east side)—specimen OOPM-C.



(a) Gap opening at the RC-SC interface



(b) Significantly deformed specimen

Fig. 22. Damage of specimen OOPM-C.

was measured from the RC wall portion of the specimen (SP4).  $P_{max}$  was greater than the force associated with the flexural strength of the RC wall portion calculated using ACI 349 (ACI, 2006) provisions ( $P_{Mn.RC}$ ) with the measured material properties by 75.8 kips (15%).

Figure 24 shows the applied force-strain response of the #14 rebar. The bottom #14 rebar exhibited strain values greater than their yield strain ( $\epsilon_y = 2,330 \mu\epsilon$ ) at  $P_{max}$ , with maximum strain value of 2,710  $\mu\epsilon$  (SG 8). The same figure presents the response of wing plates and tie plates. The plates remained in the elastic range during the test, exhibiting maximum strain of 1,670  $\mu\epsilon$  (tie plates, SG 20) and -297  $\mu\epsilon$  (wing plates, SG 23) at  $P_{max}$ , respectively. The applied force-baseplate strain response shows the maximum strain of 176  $\mu\epsilon$  (SG 27).

Figure 25 shows the overall damage progression in terms of concrete crack pattern. As shown, the damage progression was similar to specimen OOPM-C. The first flexural crack occurred at 18% of  $P_{max}$ . As the load increased, additional flexural cracks were formed within the RC wall shear span, as well as in the SC wall region around 150 kips ( $0.26P_{max}$ ). The flexural cracks transformed into flexural-shear cracks, and cracks appeared in the connection region at 52% of  $P_{max}$ . After the yielding of the #14 reinforcement, the compression zone under the loading point (RC wall portion) softened as a result of concrete crushing and spalling, which initiated around 90% of  $P_{max}$  as shown in Figure 26(a). Thus, the beam deformations became prominent as the specimen deflected in a ductile manner, as shown in Figure 26(b).

## NUMERICAL INSIGHT INTO BEHAVIOR

A three-dimensional (3D) finite element model (FEM) was developed and analyzed to provide better insight into the

force transfer mechanism for the design demand. Analysis was conducted to predict the performance, strength, ductility, and failure mode of the designed specimens. The tests described in the previous section were simulated using the commercially available finite element modeling (FEM) software LS-DYNA, (LS-DYNA, 2012a, 2012b) employing an explicit time-stepping algorithm.

## Analysis Approach

The concrete in the SC and RC wall portions, the SC wall faceplate, and the connection region (wing plates, tie plates, and baseplates), as well as the RC wall flexural reinforcement, were modeled using eight-node hexahedron solid elements with six degrees of freedom per node as shown in Figure 27. The two most common integration techniques used for solid elements in LS-DYNA are the reduced and full integration technique (LS-DYNA, 2012a, 2012b). Concrete was modeled using a computationally less extensive constant stress (ELFORM 1, reduced integration) formulation. However, the connection region, SC wall faceplate, and flexural reinforcement (#14 rebar) were modeled using full integration element formulation due to the nature of their geometries. While the reduced integration technique has an inherent drawback of introducing zero energy modes, commonly referred to as hourglass modes, it does compensate by providing the computational efficiency. The potential hourglassing issue was prevented by introducing stiffness-based hourglass control with an hourglassing coefficient of 0.1 consistent with the values used by Yang (2015). On the contrary, full integration technique is prone to shear interlocking in case of pure bending. To overcome the issue, the LS-DYNA full integration type for poor aspect ratio (ELFORM 1) was used to reduce transverse shear locking. The Hughes-Liu beam element formulation (ELFORM 1)

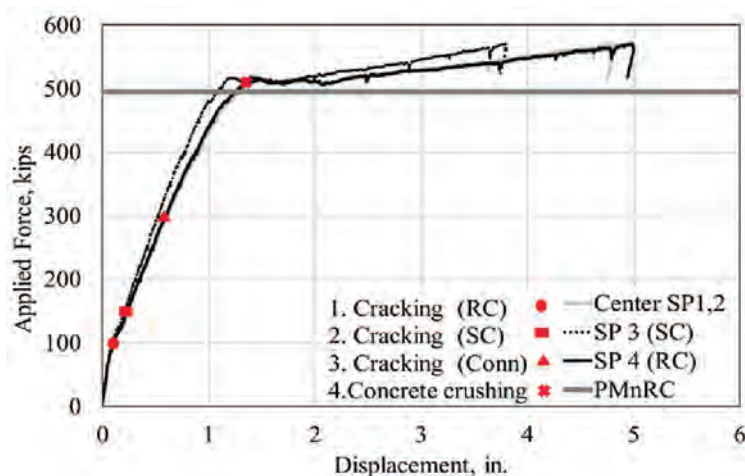


Fig. 23. Applied force-displacement response of specimen OOPM-DN.

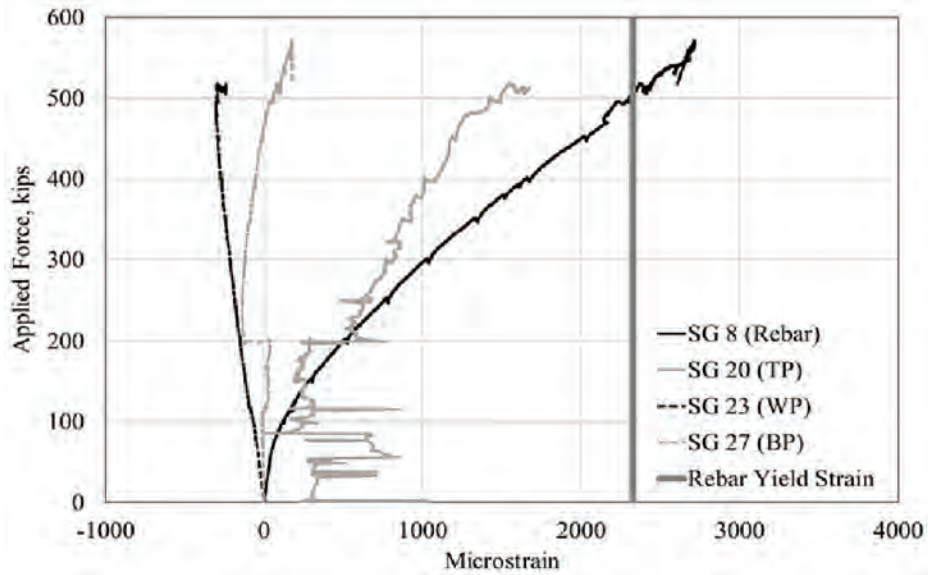


Fig. 24. Applied force–strain response of specimen OOPM-DN (#14 rebars, wing plates, tie plates, and baseplates).

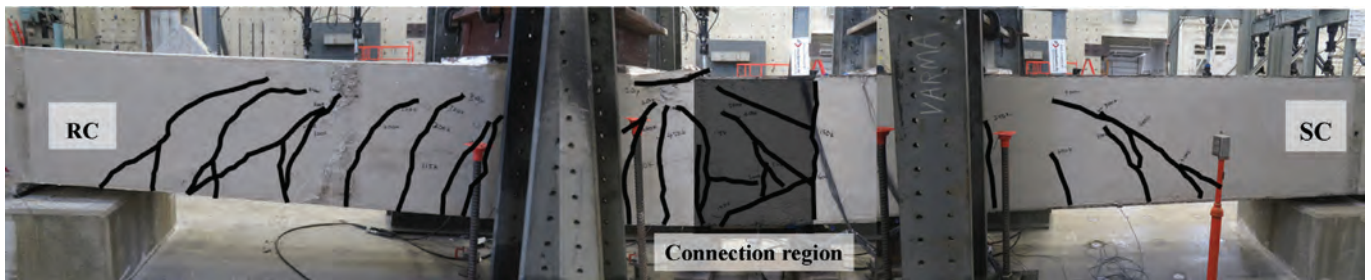
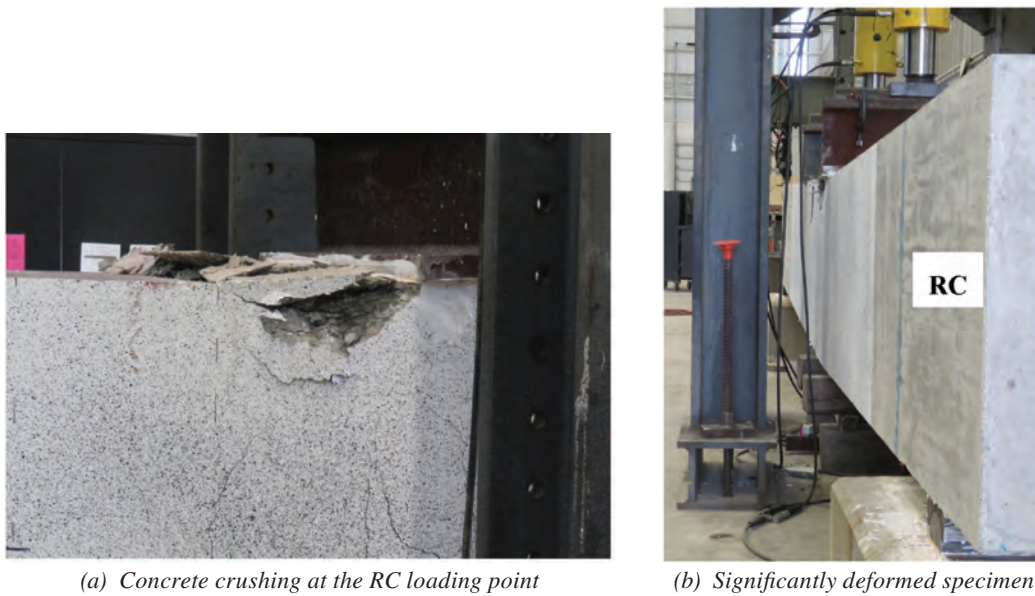


Fig. 25. Concrete crack pattern (east side)—specimen OOPM-DN.



(a) Concrete crushing at the RC loading point

(b) Significantly deformed specimen

Fig. 26. Damage of specimen OOPM-DN.

was used to explicitly model the RC wall shear reinforcement, SC wall shear studs, and tie bars using two node beam elements with one-point integration and a circular cross section, as shown in Figure 28. These element formulations are evaluated by various authors, including Bruhl et al. (2015b) and Epackachi et al. (2015). Both definitions for solid and beam elements are accessible via SECTION\_SOLID keyword. The average size of a solid element across the faceplate and the concrete infill is 1 in.

RC wall reinforcement and SC wall studs and tie bars (tied to the faceplate) were embedded in the respective concrete portions by coupling the acceleration and velocity via the Constrained\_Lagrange\_In\_Solid (CLIS) keyword to depict a perfect bond behavior. Connection region tie plates, wing plates, and baseplates were also coupled to the SC wall infill concrete using the same constraint definition. Interaction between SC wall infill concrete and faceplate was defined using the Automatic\_Surface\_To\_Surface formulation. This two-way contact definition prevents the slave and master nodes from penetration. In the tangential direction, a median value of coefficient of friction equal to 0.64, reported by Rabbat and Russel (1985), was used. The embedment length of the RC wall flexural reinforcement extending inside the SC wall was less than the required

development length from ACI 349 (ACI, 2006); therefore, it was not embedded inside the SC wall (connection region), and its interaction with infill concrete was also defined using the same contact definition. Additionally, the interaction between loading plates, support rollers, and corresponding surfaces of RC and SC walls were simulated using the same contact formulation.

### Material Models and Properties

Continuous\_Surface\_Cap\_Model (CSCM) concrete (MAT 159), chosen from the library of LS-DYNA (LS-DYNA, 2012a, 2012b), is an isotropic model that requires only basic strength data ( $f'_c$ ) and aggregate size. Therefore, it minimizes the need for expansive testing to determine a wide range of parameters. The input compressive strength was based on the average values obtained on the day of tests. The concrete material model (MAT 159) was developed as part of an effort to predict the performance of roadside concrete safety structures. The strength of the isotropic cap model revolves around the smooth intersection between failure and cap surfaces. To simulate concrete damage progression such as cracking, crushing, and spalling, element erosion criteria in the form of maximum and

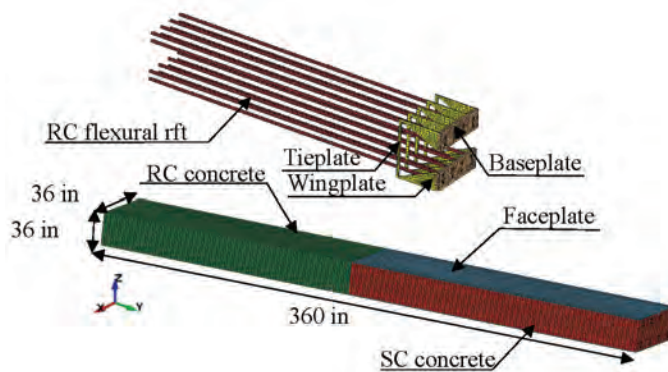


Fig. 27. FEM solid element formulation.

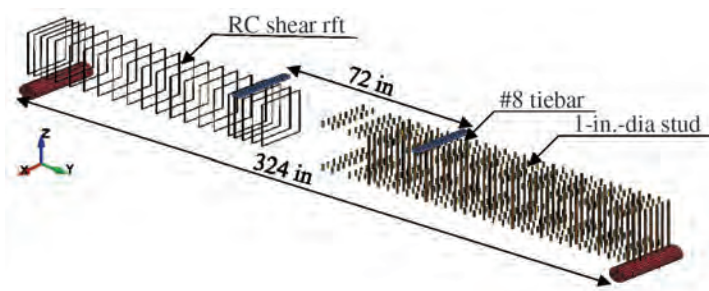


Fig. 28. FEM beam element formulation.



Material Type	Input Parameters	Value/Equation	Reference
Concrete	Mass density	$2.25 \times 10^{-4}$ lbfs <sup>2</sup> /in.	
	Unconfined compression strength	Table 2	Based on material tests
	Maximum aggregate size	0.750 in.	Experimental data
	Erosion criteria: MNEPS MXEPS	-0.003 0.005	Equation 6
Steel	Mass density	$7.34 \times 10^{-4}$ lbfs <sup>2</sup> /in.	
	Young's modulus	$2.90 \times 10^7$ psi	
	Poisson's ratio	0.300	
	Yield strength	Table 2	Based on material tests
	Failure strain	Table 2	Based on material tests
	Stress-plastic strain curve	Table 2	Based on material tests
	Hardening variable	0	LS-DYNA (2012a, 2012b)

minimum principal strains were artificially included by defining a MAT\_ADD\_EROSION keyword. A concrete ultimate compressive strain value of  $-0.003$  was specified as minimum principal strain (MNEPS), whereas maximum principal strain (MXEPS) was calculated using Equation 6. These values are consistent with the findings obtained by Yang (2015), where  $\omega$  is the crack width at zero tensile strength and  $V_e$  is the volume of one solid element. Concrete crack width,  $\omega$ , can be estimated from Equation 7. In Equation 7,  $f_t$  is uniaxial tensile strength and  $G_f$  is specified fracture energy, which can be estimated using Equation 8 (Wittmann et al., 1988). In Equation 8,  $\Phi$  is the maximum aggregate size.

$$\text{Maximum principal strain (MXEPS)} = \frac{\omega}{\sqrt[3]{V_e}} \quad (6)$$

$$\omega = \frac{2G_f}{f_t} \quad (7)$$

$$G_f = 1.297\Phi^{0.32} \quad (8)$$

RC wall reinforcement, connection region, and SC wall faceplates were modeled using the Piecewise\_Linear\_Plasticity material model (MAT 24). It is a constitutive steel material model with isotropic elastic, von Mises yield criterion, associated flow rule, and post-yield plastic behavior (Kurt et al., 2016). MAT 24 provides the flexibility of defining post-yield hardening behavior in form of effective stress-plastic strain curves averaged from standard uniaxial tension coupon tests performed during the experimentation

phase, thus allowing explicit modeling of nonlinear behavior. SC wall shear studs and tie bars were modeled with Plastic\_kinematic (MAT 03) material model. Both the steel models are featured with a strain rate scale effect, which was not activated due to quasi-static nature of tests. Additionally, Rigid material (MAT 20) was used to provide material definition for loading beams and roller supports. Table 3 summarizes the material properties used in the simulations.

### Analytical Verification

Figure 29 shows the analytically predicted applied force-displacement response of the model mapped over the experimentally measured response of the OOPM-C test specimen. As shown, the analytically predicted response is in close agreement with the experimentally measured response. The displacement is measured under the RC wall portion loading point (36 in. from the interface of SC wall region). The analytically predicted maximum load,  $P_{max}^{FEA}$ , was 571 kips, which is greater than the force associated with the flexural strength of the RC wall portion,  $P_{Mn,RC} = 495$  kips, by 15%. The shear force,  $V_{Pmax}^{FEA}$ , associated with the analytically predicted  $P_{max}^{FEA}$  was 286 kips, which is less than the shear strength of the RC wall portion ( $V_{n,RC} = 329$  kips), confirming flexural yielding as the governing failure mode.

The maximum stress predicted in the bottom layer of #14 rebar was approximately 93 ksi, which is just over 125% of the yield stress of the reinforcing bars ( $1.25F_{y,r} = 83.3$  ksi). Longitudinal strain responses predicted by the model are

compared with experimentally measured strain responses in Figure 30. In the case of the tie plate, SG 20 values were compared directly with corresponding simulated strains in Figure 30(a). In Figure 30(b), the same comparison is shown for the wing plate (SG 22). The simulated strain values are in a reasonable agreement compared with observed data in this case. Strain contour plots of the mechanical connection region at  $P_{max}^{FEA}$  are shown in Figure 31. As shown, the maximum predicted strain values for the tie plate (corresponding to SG 20) and wing plate (corresponding to SG 22) are somewhat lower than the experimental data. This was attributed to the treatment of the interface between concrete and the steel plates in the connection region in the model. The steel

plates (tie plate, wing plate, and baseplate) were embedded in concrete in the model, which allows the perfect composite action. However, no perfect composite action is developed in the connection region of the specimens. Only a limited level of bonding between the steel plates and concrete is achieved. For this reason, the tie plate and wing plate carried lower stress and exhibited lower strain. However, all steel components (including tie plate, wing plate, and baseplate) in the connection region remained in the elastic range until the connected RC wall portion developed its flexural strength (RC flexural yielding), which is in accordance with the experimental observation.

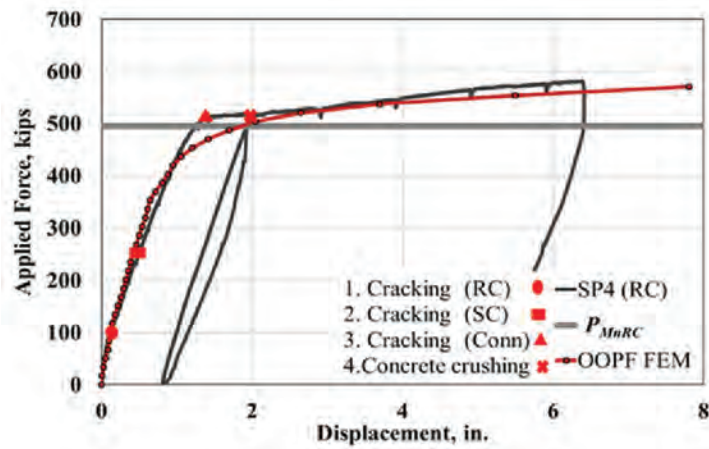
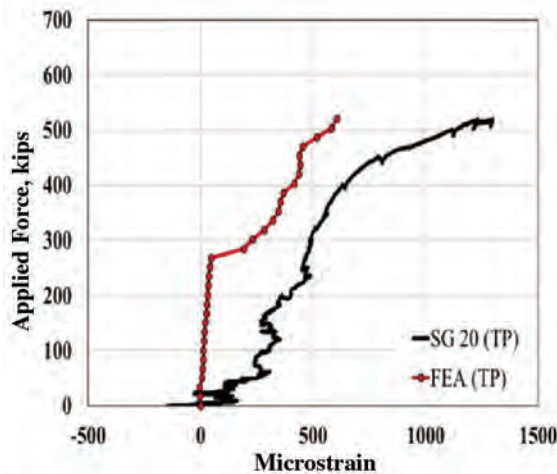
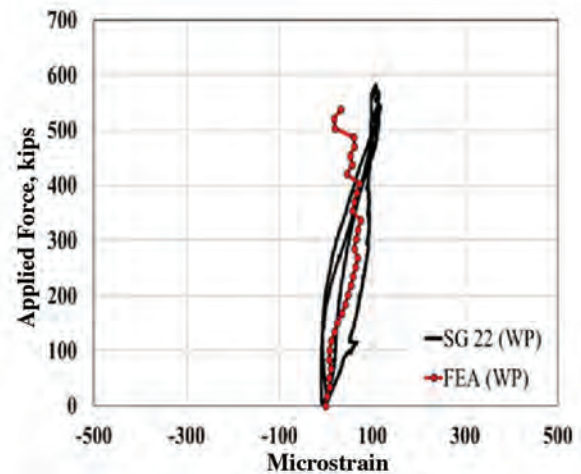


Fig. 29. Comparison between experimental (OOPM-C) and FEA results.



(a) Tie plate



(b) Wing plate

Fig. 30. Strain gauge data (experimental vs. FEA).

## SUMMARY AND CONCLUSIONS

Both experimental and numerical investigations were conducted to evaluate the design procedure developed for SC wall-to-RC wall mechanical connections. The design procedure was developed based on the full-strength connection design philosophy. The applied force-displacement responses and the applied force-steel strain responses were measured and evaluated to determine the ultimate strength and the governing failure. The measured strengths were compared with the RC wall strength determined using ACI 349 (ACI, 2006). The results from both experimental and analytical investigations indicated the following:

1. The governing failure mode of the two test specimens was flexural yielding of the RC components, ensuring energy dissipation away from the connection region. Thus, the connection region can be designed and detailed using the proposed design procedure.
2. The type of connection plan, coupler or double nut, had no influence on the force transfer mechanism of the designed connection.
3. The measured ultimate strength was 585 kips for specimen OOPM-C and 571 kips for specimen OOPM-DN, which was greater than the ACI code equation by 18% and 15%, respectively.
4. All the steel components in the connection region remained in the elastic range until the RC wall developed its full flexural strength.
5. The experimentally observed and analytically predicted maximum strain values in the case of the wing plates and

baseplates were well under their yield strain, indicating a significant contribution of the concrete in the force transfer mechanism and exhibiting conservatism in the design procedure.

6. The proposed design procedure is suitable and conservative for designing SC wall-to-RC mechanical connections. However, additional experimental and analytical studies should be conducted to expand the limited database and further verify the design procedure for different loading conditions such as in-plane and out-of-plane shear.

## ACKNOWLEDGMENTS

This research was funded by KEPCO E&C, Korea, and the specimens were tested at Bowen Laboratory at Purdue University. The authors acknowledge the valuable contributions of the sponsor and all the technical staff involved in the experimental and analytical work throughout the execution of the project. However, the views presented in this paper are solely those of the authors.

## REFERENCES

- ACI (2006), *Code Requirements for Nuclear Safety-Related Concrete Structures and Commentary*, ACI 349-06, American Concrete Institute, Farmington Hills, Mich.
- ACI (2019), *Building Code Requirements for Structural Concrete*, ACI 318-19, American Concrete Institute, Farmington Hills, Mich.

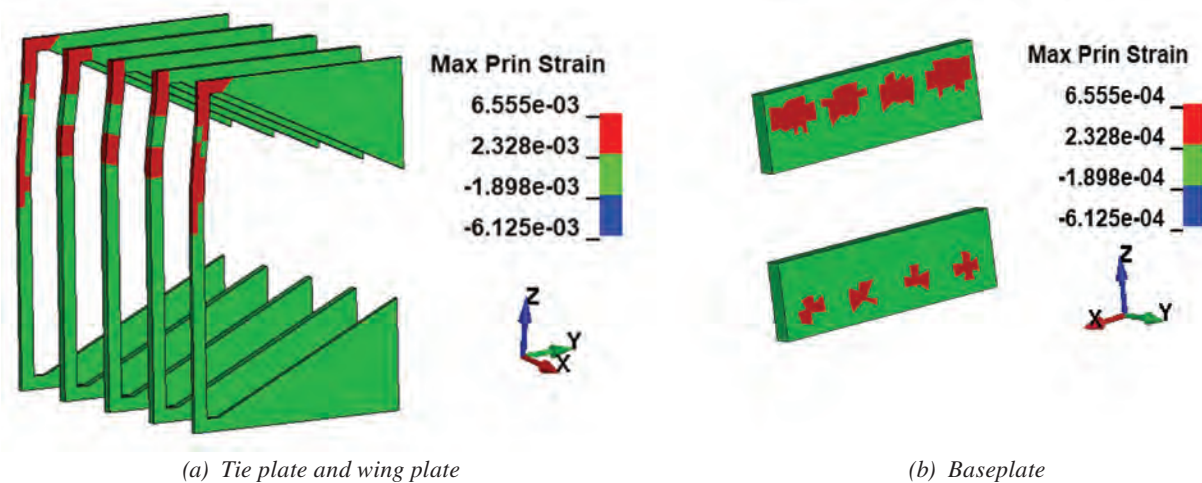


Fig. 31. Strain contour plot.

- AISC (2016), *Seismic Provisions for Structural Steel Buildings*, ANSI/AISC 341-16, American Institute of Steel Construction, Chicago, Ill.
- AISC (2018), *Specification for Safety-Related Steel Structures for Nuclear Facilities*, ANSI/AISC N690-18, American Institute of Steel Construction, Chicago, Ill.
- AISC (2019), *Companion to the AISC Steel Construction Manual, Volume 1: Design Examples*, Version 15.1, American Institute of Steel Construction, Chicago, Ill.
- ASTM (2013), *Standard Test Method for Tension Testing of Metallic Materials*, ASTM E8/E8M, ASTM International, West Conshohocken, Pa.
- ASTM (2014), *Standard Test Method for Compressive Strength of Cylindrical Concrete Specimens*, ASTM C39/C39M, ASTM International, West Conshohocken, Pa.
- ASTM (2016), *Standard Specification for Deformed and Plain Low-Alloy Steel Bars for Concrete Reinforcement*, ASTM A709/A709M-16, ASTM International, West Conshohocken, Pa.
- ASTM (2020), *Standard Specification for Hex Cap Screws, Bolts and Studs, Steel, Heat Treated, 120/105/90 ksi Minimum Tensile Strength, General Use*, ASTM A449-14 (2020), ASTM International, West Conshohocken, Pa.
- Bhardwaj, S.R., Sener, K.C., and Varma, A.H. (2019), “Multi-Hazard Investigation and Testing of Steel-Plate Composite (SC) Wall Piers: Seismic and Thermal Loads,” *Nuclear Engineering and Design*, Vol. 348, pp. 121–130. <https://doi.org/10.1016/j.nucengdes.2019.03.026>
- Bhardwaj, S.R. and Varma, A.H. (2017), *Design of Modular Steel-Plate Composite Walls for Safety Related Nuclear Facilities*, Design Guide 32, AISC, Chicago, Ill.
- Bruhl, J.C., Varma, A.H., and Johnson, W.H. (2015a), “Design of Composite SC Walls to Prevent Perforation from Missile Impact,” *International Journal of Impact Engineering*, Vol. 75, pp. 75–87. <https://doi.org/10.1016/j.ijimpeng.2014.07.015>
- Bruhl, J.C., Varma, A.H., and Kim, J.M. (2015b), “Static Resistance Function for Steel-Plate Composite (SC) Walls Subject to Impactive Loading,” *Nuclear Engineering and Design*, Vol. 295, pp. 843–859. <https://doi.org/10.1016/j.nucengdes.2015.07.037>
- Choi, B.J. and Han, H.S. (2009), “An Experiment on Compressive Profile of the Unstiffened Steel Plate-Concrete Structures under Compression Loading,” *Steel and Composite Structures*, Vol. 9, No. 6, pp. 519–534. <https://doi.org/10.12989/scs.2009.9.6.519>
- Epackachi, S., Whittaker, A.S., Varma, A.H., and Kurt, E.G. (2015), “Finite Element Modeling of Steel-Plate Concrete Composite Wall Piers,” *Engineering Structures*, Vol. 100, pp. 369–384.
- Foundoukos, N. and Chapman, J.C. (2008), “Finite Element Analysis of Steel–Concrete–Steel Sandwich Beams,” *Journal of Constructional Steel Research*, Vol. 64, No. 9, pp. 947–961. <https://doi.org/10.1016/j.jcsr.2007.10.011>
- Hong, S.G., Lee, K.J., Park, D.S., Ham, K.W., and Lee, H.W. (2009), “Out-of-Plane Shear Strength of Steel Plate Concrete Walls Dependent on Bond Behavior,” *Proceedings of 20th International Conference on Structural Mechanics in Reactor Technology (SMiRT-20)*, Div-6: Paper ID# 1855, August 9–14, Espoo, Finland.
- Hwang, K.M., Lee, K.J., and Kim, W.K. (2013), “An Experimental Study on the Flexural and Shear Behavior of Steel Plate Concrete–Reinforced Concrete Connected Structures,” *Nuclear Engineering and Design*, Vol. 257, pp. 88–99. <https://dx.doi.org/10.1016/j.nucengdes.2012.12.020>
- JEAC (2009), *Technical Code for Seismic Design of Steel Plate Reinforced Concrete Structures: Buildings and Structures*, JEAC-4618, Japanese Electric Association Nuclear Standards Committee, Tokyo, Japan.
- KEA (2010), *Specification for Safety-Related Steel Plate Concrete Structures for Nuclear Facilities*, KEPIC-SNG, Board of KEPIC Policy, Structural Committee, Korea Electric Association.
- Kim, K., Lee, K., Shun, J., Lee, J., and Varma, A.H. (2020), “A Study on the Resistance of SC Walls Subjected to Missile Impact Using Large-Scale Impact Tests,” *International Journal of Impact Engineering*, Vol. 139. <https://doi.org/10.1016/j.ijimpeng.2020.103507>
- Kurt, E.G. (2016), “Steel-Plate Composite (SC) Walls and Their Basemat Connections: Seismic Behavior, Analysis, and Design,” PhD Dissertation, Purdue University, West Lafayette, Ind.
- Kurt, E.G., Varma, A.H., Booth, P., and Whittaker, A.S. (2016), “In-Plane Behavior and Design of Rectangular SC Wall Piers without Boundary Elements,” *Journal of Structural Engineering*, Vol. 142, No. 6. [https://doi.org/10.1061/\(ASCE\)st.1943-541x.0001481](https://doi.org/10.1061/(ASCE)st.1943-541x.0001481)
- Lee, K.J., Hwang, K.M., Hahm, K.W., and Kim, W.B. (2012), “An Experimental Study on Flexural/Shear Load Properties of SC (Steel Plate Concrete) Structure with Reinforced Concrete Joint,” *Journal of Korean Society of Steel Construction*, Vol. 24, No. 2. <https://doi.org/10.7781/kjoss.2012.24.2.137>
- Lee, S.J., Choi, B.J., and Kim, T.K. (2009), “An Experimental Study on the Behavior of Steel Plate-Concrete Wall with Vertical Ribs,” *Journal of Korean Society of Steel Construction*, Vol. 1, No. 3, pp. 277–287.

- Leng, Y.B., Song, X.B., Chu, M., and Ge, H.H. (2015), "Experimental Study and Theoretical Analysis of Resistance of Steel-Concrete-Steel Sandwich Beams," *Journal of Structural Engineering*, Vol. 141, No. 2.
- LS-DYNA (2012a), *Keyword User's Manual*, Vol. I, Version 971 R6.0.0, Livermore Software Technology Corporation (LSTC), Livermore, Calif.
- LS-DYNA (2012b), *Keyword User's Manual*, Vol. II, Version 971 R6.0.0, Livermore Software Technology Corporation (LSTC), Livermore, Calif.
- McKinley, B. and Boswell, L.F. (2002), "Behavior of Double Skin Composite Construction," *Journal of Constructional Steel Research*, Vol. 58, No. 10, pp. 1347–1359. [https://doi.org/10.1016/s0143-974x\(02\)00015-9](https://doi.org/10.1016/s0143-974x(02)00015-9)
- Ozaki, M., Akita, S., Osuga, H., Nakayama, T., and Adachi, N. (2004), "Study on Steel Plate Reinforced Concrete Panels Subjected to Cyclic In-Plane Shear," *Nuclear Engineering and Design*, Vol. 228, pp. 225–244. <https://doi.org/10.1016/j.nucengdes.2003.06.010>
- Rabbat, B.G. and Russell, H.G. (1985), "Friction Coefficient of Steel on Concrete or Grout," *Journal of Structural Engineering*, Vol. 111, No. 3, pp. 505–515. [https://doi.org/10.1061/\(ASCE\)0733-9445\(1985\)111:3\(505\)](https://doi.org/10.1061/(ASCE)0733-9445(1985)111:3(505))
- Sener, K.C., Varma, A.H., and Ayhan, D. (2015), "Steel-Plate Composite (SC) Walls: Out-of-Plane Flexural Behavior, Database, and Design," *Journal of Constructional Steel Research*, Vol. 108, pp. 45–59. <https://doi.org/10.1016/j.jcsr.2015.02.002>
- Seo, J. and Varma, A.H. (2017a), "Experimental Behavior and Design of Steel Plate Composite-to-Reinforced Concrete Lap Splice Connections," *Journal of Structural Engineering*, Vol. 143, No. 5. [https://doi.org/10.1061/\(ASCE\)st.1943-541x.0001711](https://doi.org/10.1061/(ASCE)st.1943-541x.0001711)
- Seo, J. and Varma, A.H. (2017b), "Behavior and Design of Steel-Plate Composite Wall-to-Wall Corner or L-Joints," *Nuclear Engineering and Design*, Vol. 323, pp. 317–328. <https://doi.org/10.1016/j.nucengdes.2017.04.008>
- Seo, J. and Varma, A.H. (2017c), "SC Wall-to-Slab Connections in Safety Related Nuclear Facilities," *Proceedings of 24th International Conference on Structural Mechanics in Reactor Technology (SMiRT-24)*, August 20–25, Busan, Korea.
- Seo, J. and Varma, A.H. (2019), "Steel Plate Composite Wall-to-Wall T-Joints: Joint Shear Strength," *Journal of Structural Engineering*, Vol. 145, No. 7. [https://doi.org/10.1061/\(ASCE\)st.1943-541x.0002317](https://doi.org/10.1061/(ASCE)st.1943-541x.0002317)
- Song, X., Chu, M., Ge, H., and Wang, H. (2014), "A Failure Criterion for Steel-Concrete Composite Walls," *Proceedings of the International Conference on Sustainable Development of Critical Infrastructure*, Shanghai, China. <https://doi.org/10.1061/9780784413470.034>
- Takeuchi, M., Narikawa, M., Matsuo, I., Hara, K., and Usami, S. (1998), "Study on a Concrete Filled Structure for Nuclear Power Plants," *Nuclear Engineering and Design*, Vol. 179, pp. 209–223.
- Wittmann, F.H., Rokugo, K., Bruhwiler, E., Mihashi, H., and Simonin, P. (1988), "Fracture Energy and Strain Softening of Concrete as Determined by Means of Compact Tension Specimens," *Materials and Structures*, Vol. 21, No. 121, pp. 21–32.
- Yang, Y. (2015), "Shear Strength and Behavior of Reinforced Concrete Structures with T-Headed Bars in Safety-Related Nuclear Facilities," PhD Dissertation, Purdue University, West Lafayette, Ind.
- Zhang, K., Seo, J., and Varma, A.H. (2020), "Steel-Plate Composite Walls: Local Buckling and Design for Axial Compression," *Journal of Structural Engineering*, Vol. 146, No. 4. [https://doi.org/10.1061/\(ASCE\)st.1943-541x.0002545](https://doi.org/10.1061/(ASCE)st.1943-541x.0002545)



# Practice-Accessible Methodology for Nonlinear Refined Analysis of Gusset Plate Connections of Steel Truss Bridges

ALIREZA MOHAMMADI and WALID S. NAJJAR

---

## ABSTRACT

A new approach is proposed for estimating structural capacity of gusset plate connections of steel truss bridges. The approach involves nonlinear refined analysis of a truss model, consisting of a single truss made of shell elements for two gusset plates at a subject connection and frame elements for truss members. Connectors (bolts or rivets) are excluded from the proposed model in order to simplify the model, with the knowledge that their associated failure modes can be addressed by simplified design calculations. Only yielding and buckling failure modes of gusset plates are considered. The new approach is calibrated by comparison with laboratory test data from NCHRP Project 12-84. The primary intent of this paper's approach is to reduce the complexity of the refined analysis developed under this National Cooperation Highway Research Program project and make it more user-friendly to load rating engineers seeking accurate estimation of gusset plate capacity. Further, an imperfection sensitivity curve characterizing reduction in capacity as a function of lateral imperfection (gusset plate out-of-flatness) in gusset plate geometry is introduced as an added tool for the load rating engineer, providing more confidence in capacity estimation. Based on a limited case study, the proposed refined analysis provides an estimate of gusset plate capacity that is approximately equal to capacity calculated by the truncated Whitmore method of the AASHTO *Manual for Bridge Evaluation* (2018). In other words, the proposed approach validates the truncated Whitmore method as compared to the more conservative partial shear method of the AASHTO *Manual*.

**Keywords:** steel truss bridge, gusset plate connection, finite element analysis, load rating, inelastic compression buckling, nonlinear buckling.

---

## BACKGROUND

The history of steel truss bridges goes back to the late 19th century when steel displaced wood and iron as the material of choice for truss bridge construction. However, the first significant experimental study on steel gusset plate connections was performed by Wyss (1926), followed by several successive substantial studies in the next decades (Sandel, 1950; Whitmore, 1952; Irvan, 1957; Hardin, 1958; Vasarhelyi, 1971). These research efforts indicated that the maximum tensile and compressive stresses in gusset plates develop at the end of the truss members. Whitmore conducted a set of experiments on Warren truss joints of a small-scale model. Based on the results, he proposed his effective width concept known as the Whitmore section, formed of a line through the end row of rivets/bolts intersected by two lines radiating outward at 30° angles from the first row of rivets/bolts. Thereafter, common design

practice for gusset plates has consisted of (1) using beam theory over general sections and calculating the resultant moment and shear on a free-body diagram (for overall failure consideration); (2) adopting the Whitmore section method for tensile/compressive stresses at the end of truss members (for local buckling and yielding considerations); and (3) rivet/bolt shear, block shear, and hole bearing failures (for fasteners and gusset plate-fastener interaction considerations).

In 2007, the collapse of the I-35 bridge in Minneapolis led the bridge engineering community to reevaluate contemporary measures of safety and reliability of gusset plate connections of steel truss bridges. The investigations conducted by the National Transportation Safety Board (NTSB) indicated compression buckling in gusset plates as the initial cause for the subsequent bridge collapse (NTSB, 2008). In response to this disaster, the Federal Highway Administration (FHWA) issued recommendations for supplementary gusset plate load ratings for non-load-path-redundant steel truss bridges as well as new AASHTO procedures for design and load rating of gusset plates. However, there was not sufficient knowledge to address the concerns raised by the I-35 bridge collapse at the time. On that basis, NCHRP Project 12-84 (Ocel, 2013) was commissioned in 2008 (and completed in 2013) to develop the load and resistance factor design (LRFD) and load and resistance factor rating (LRFR) guidelines for riveted and bolted gusset plate connections.

---

Alireza Mohammadi, PhD, PE, Project Engineer, Dewberry, New York, N.Y.  
Email: amohammadi@dewberry.com (corresponding)

Walid S. Najjar, PhD, PE, Quality Manager/Vice President, WSP USA Inc., Valhalla, N.Y. Email: Walid.Najjar@wsp.com

---

Paper No. 2021-03

ISSN 0013-8029

ENGINEERING JOURNAL / FIRST QUARTER / 2022 / 53

That research consisted of comprehensive experimental and analytical investigations to explore failure modes of gusset plates and reliability calibration of resistance factors for shear and buckling limit states.

Regarding gusset plate buckling resistance, National Cooperation Highway Research Program (NCHRP) research findings indicate a considerable difference in buckling failure modes between tight connections with chamfered diagonals and typical connections with non-chamfered members. In tight connections, buckling occurs after significant shear yielding along the chamfered edge. While in typical nonchamfered connections, the buckling occurs following a slight compressive yielding in the gusset plate region at the end of the compression diagonal member. Based on these findings, two alternative methods are proposed by the NCHRP research team for buckling resistance estimation: Method 1 is a twofold buckling resistance estimation including Whitmore section buckling along with a proposed partial shear yielding check. Method 2 is a revised Whitmore method known as the truncated Whitmore method. These two methods have been adopted by the AASHTO *Manual for Bridge Evaluations* (MBE) (AASHTO, 2018) for gusset plate load rating. However, the truncated Whitmore method is discussed in the MBE Commentary. Despite the calibration conducted in the NCHRP research, there is substantial uncertainty about gusset plate buckling parameters, including the buckling length and assumed effective length coefficient,  $K$ . The research findings also indicated a large discrepancy between actual magnitude and location of maximum stresses in gusset plates using beam theory. For shear yielding, this discrepancy is addressed by including a reduction factor. However, this factor is also associated with uncertainty. These uncertainties arise due to a vast variety of gusset plate geometries and, consequently, significant variation in boundary conditions of gusset plates in the local yielding/buckling region. Considering the safety margins applied for generalization of these parameters, the MBE prescriptive gusset plate capacity estimation approach involves significant conservatism that may result in unnecessary repair recommendations. Alternatively, an authentic analytical simulation approach may provide a more realistic estimation of gusset plate yielding/buckling resistance.

The AASHTO MBE allows employing refined finite element simulation to determine nominal resistance of gusset plate connections, particularly when the MBE prescriptive capacity estimation approach results in unacceptable load rating based on compression yielding or buckling criteria. The MBE Commentary refers to NCHRP research modeling attributes as a reliable approach that was able to predict gusset plate capacities with less than 10% error as compared to experimental testing results. Nevertheless, following strictly the same approach is not required, and simpler

modeling is considered acceptable depending on the target failure model under investigation. The complexity of the NCHRP research modeling approach may hinder its implementation in common load rating practice. This paper proposes a more practical finite element modeling approach to estimate gusset plate capacity associated with yielding and buckling failure modes for typical double gusset plate connections of steel truss bridges.

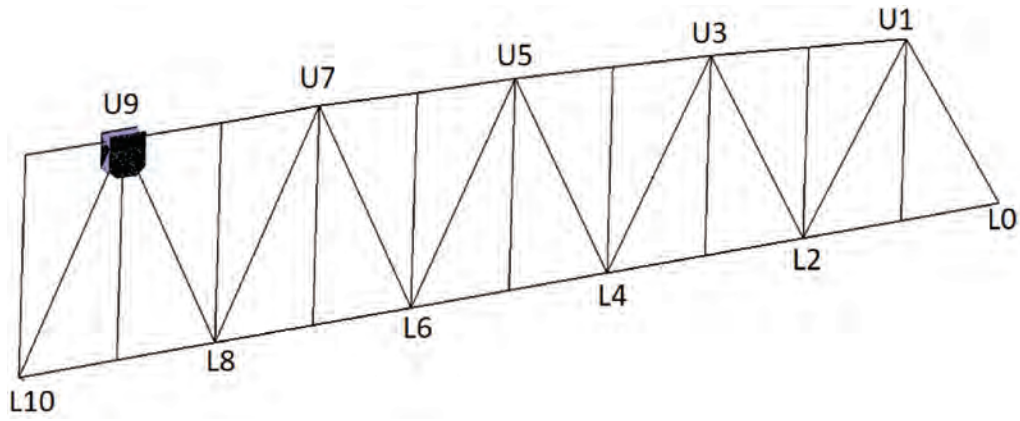
## PROPOSED NONLINEAR FINITE ELEMENT ANALYSIS APPROACH

The main concept of the alternative nonlinear finite element method (FEM) modeling and analysis approach presented in this study is to simplify an ideal full comprehensive approach by excluding model attributes related to failure modes that can be confidently evaluated by the current MBE prescriptive calculations, as well as other attributes having negligible effects on capacity estimation of remainder failure modes. Failure modes related to fasteners and gusset plate-fastener interactions, including shear resistance of fasteners, block shear resistance and hole bearing resistance, can be well evaluated with the MBE equations. Also, the NCHRP research results indicated that modeling of fasteners holes is not required for yielding and buckling failure modes. Therefore, fasteners and fasteners holes are not included in this alternative FEM modeling approach. However, proper modeling of load transfer between gusset plates and truss members at fastener locations is considered as a necessary modeling attribute in this approach.

Analytical simulations conducted under the NCHRP research indicated the necessity of utilizing shell elements to accurately predict gusset plate connection failure modes and related resistances. Besides, geometry and material nonlinearities along with inclusion of initial geometric imperfections are acknowledged as other essential modeling attributes to create an authentic FEM model for gusset plate connections. Accordingly, the mentioned attributes are considered as the basis of the proposed FEM modeling approach for gusset plate yielding and buckling failure modes.

Figure 1 illustrates FEM simulation for a subject Warren truss with refined gusset plate modeling at a top joint for gusset plate capacity investigations. Details of this simulation and the performed nonlinear analysis are discussed next and demonstrate application of the proposed approach. As shown in Figure 1(a), the model includes a full truss with a refined gusset plate model at joint U9. The full truss is simulated via ADINA v9.3 (Adina, 2017) using truss elements, except at panels 9 and 10, where truss members are modeled with beam elements to accurately present the force and moments induced in the gusset plate connection. Instead of a full-truss model, a two-panel truss system including the





(a) Full 3D truss model incorporating refined gusset plate connection modeling at joint U9

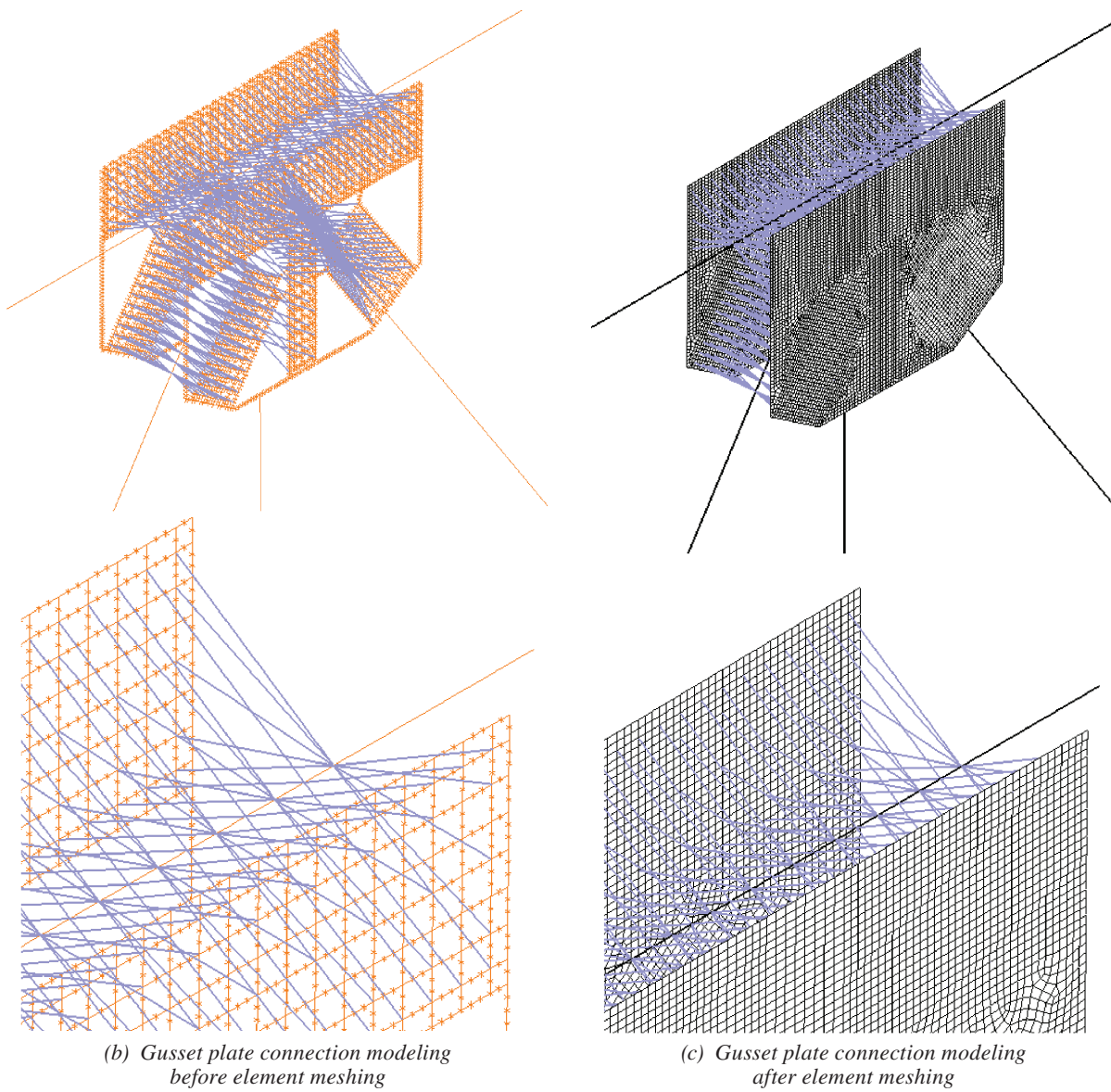


Fig. 1. An example of the proposed FEM modeling approach.

joint and two adjacent panels is acceptable for FEM simulation as recommended in the AASHTO MBE. However, boundary conditions and applied truss loads at the boundary joints shall be accurately set to guarantee the validity of the obtained results. In the NCHRP research modeling approach, the truss members attached to the gusset plates are modeled with a shell element for a distance of two member depths away from the gusset plate edge. This will significantly complicate the modeling of the truss members and gusset plate-to-truss member attachments. It will also significantly increase the time of modeling and analysis. Alternatively, in this proposed approach, the members are fully modeled with only beam elements. As shown in Figures 1(b) and 1(c), rigid links are provided to connect the truss members to the gusset plates at the fastener locations to precisely model the load transfer between them. In this approach, gusset plates are modeled using a combination of quadrilateral and triangular shell elements due to the gusset plate's complex geometry. However, quadrilateral elements constitute the majority of the elements. Utilizing triangular shell elements is relatively less favorable because it is associated with larger solution errors. Nonlinear material models should be used for gusset plate shell elements to capture the yielding, stress redistribution, and stress hardening.

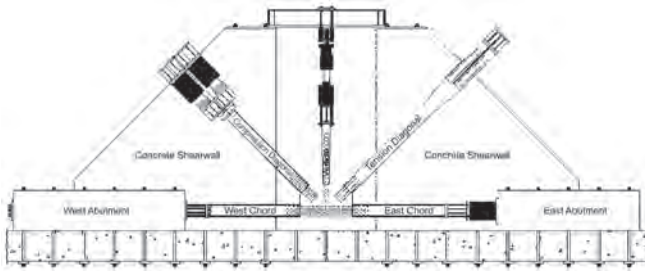
To incorporate geometric instability (buckling) failure modes into the gusset plate FEM model, proper inclusion of initial imperfection (gusset plate out-of-flatness) along with a gradually increasing load need to be applied until termination of the analysis due to structural instability. According to the AASHTO MBE, the maximum initial imperfections should be limited to the smaller of 1/150 of the longest free edge length, 10% of the gap between the end of the compression member and the next adjoining member, or the thickness of the gusset plate. However, an adequate application of this imperfection to the model is not suggested by the MBE. In the NCHRP research, the initial imperfection was applied to both the gusset plate and the compression diagonal member. The imperfection was applied by a separate linear analysis imposing transverse pressure to the end of compression diagonal until reaching the desired out-of-flatness. This will generate an initial imperfection shape following the gusset plate's first buckling mode, which is a transverse sway mode. However, this approach may result in unrealistic locked-in stresses induced by the applied imperfection. Moreover, due to uncertainty about actual imperfection, applying a single initial imperfection without considering the gusset plate's buckling sensitivity to initial imperfection may result in an underestimation of the imperfection effect. Alternatively, in this proposed approach, the initial imperfection is included with a transverse load applied at the end of the compression diagonal beam element simultaneously increasing with truss loading steps. The buckling sensitivity is studied by

applying a reasonable range of the mentioned imperfection simulating load. This will provide the load rating engineer with a full picture of the buckling resistance sensitivity and helps the engineer for more reliable gusset plate buckling resistance estimation.

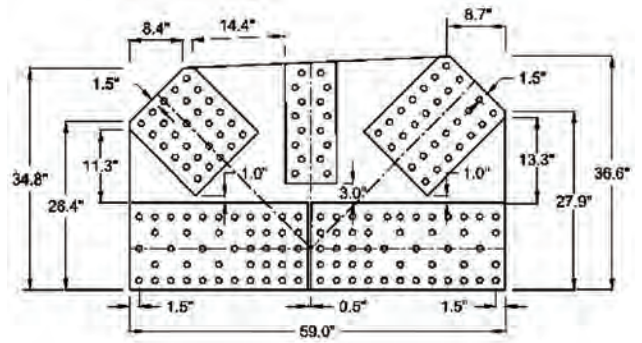
## VALIDATION ANALYSES FOR THE PROPOSED MODELING APPROACH

A set of validation analyses was conducted to evaluate the accuracy and reliability of the proposed nonlinear FEM analysis approach. For this purpose, full-scale experimental tests conducted under the NCHRP research for specimens E1-WV-307SS were simulated utilizing the approach proposed in this study. The ADINA v9.3 finite element package was used to generate structural models and conduct gusset plate connection nonlinear analyses. Figure 2(a) shows the load frame used in the NCHRP tests to simulate the loading applied on a double-gusset plate connection at the lower joint of a Warren truss configuration with vertical truss members. As shown, the truss loads were applied through five independent jacking systems at the end of the truss members. The experimental testing included four E1-WV-307SS specimens, all with the same gusset plate geometry as shown in Figure 2(b) but different thicknesses, including 0.25 in., 0.3125 in., 0.4375 in., and 0.5 in. Reported test observations indicated gusset plate inelastic buckling at the compression diagonal as the failure mode for all four specimens. Accordingly, this specific set of specimens was selected for this validation to thoroughly investigate the validity of this analysis technique to capture localized initial yielding and consequent inelastic buckling of gusset plates at the compression diagonal.

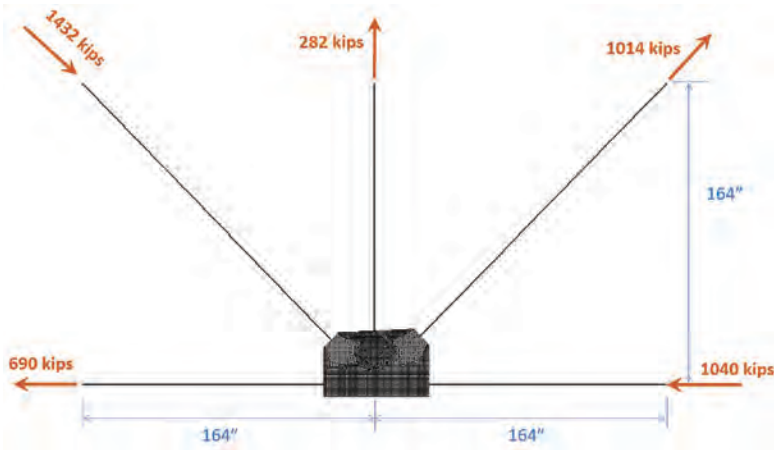
Figures 2(c) and 2(d) show the 3D FEM model developed for the validation analysis. The proposed modeling approach explained in the earlier section was utilized in this model. The model includes a shell element for gusset plates with nonlinear steel material model, elastic beam-element truss members (chords, diagonals, and the vertical), and rigid links connecting the truss members to the gusset plates at actual bolt locations. Figure 2(c) shows the truss loads applied at the end of the truss members. The loads are scaled up to twice the failure loads obtained for the 0.5-in. thickness. The larger loads were applied to ensure capturing simulation failure resistances higher than the reported test failure resistances. The loads were applied gradually with 1% increments along with software's automatic incrementation control (for further substepping at analysis diverging steps) to ensure capturing material and geometric nonlinearity until final failure. The loading step corresponding to the failure of analysis is presented as the applied load factor (ALF). ALF represents the fraction of total load at the last analysis step. The boundary conditions at the end of



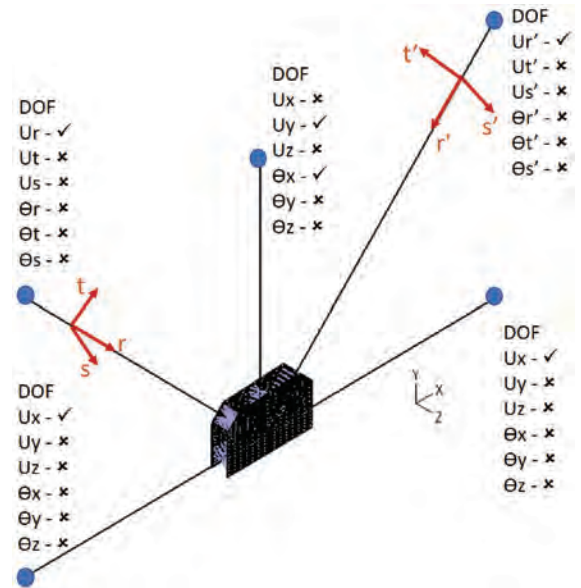
(a) NCHRP test load frame



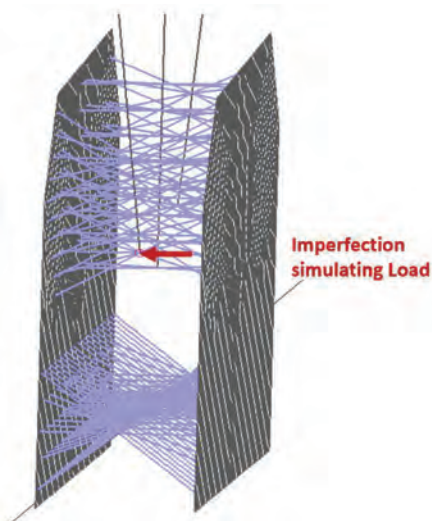
(b) Geometry of E1-WV-307SS specimens



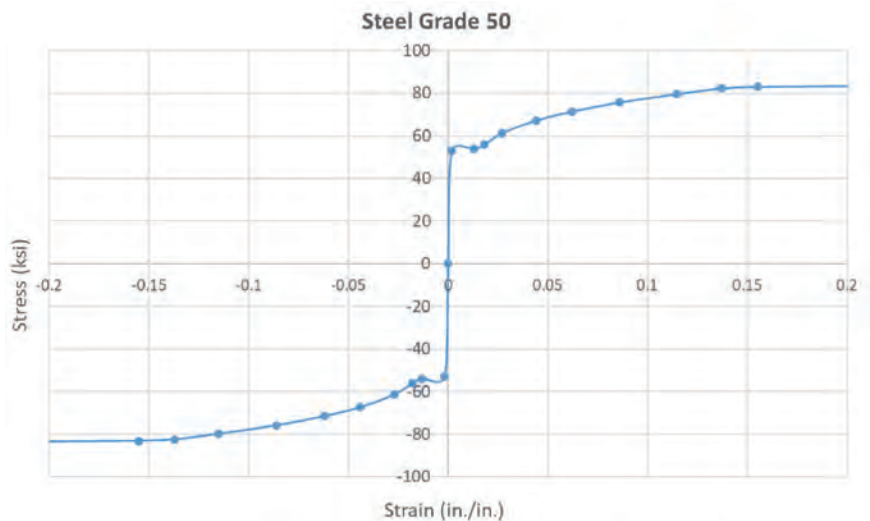
(c) Test simulation model, loads and dimensions



(d) Test simulation model, boundary conditions



(e) Imperfection simulating load



(f) Stress-strain relationship for Grade 50 steel

Fig. 2. E1-WV-307SS NCHRP test simulations.

truss members are shown in Figure 2(d) ( $U$  for translational, and  $\theta$  for the rotational degrees of freedom). As shown, all members are only free for translational movement in their longitudinal directions, except the vertical member, which has freedom for out-of-truss plane rotation. These translational and rotational fixities correspond to the constraints provided at the jacking setups. As shown in Figure 2(d), secondary coordinate systems were defined for diagonal members to facilitate the applications of loads and boundary conditions for the diagonal members. As illustrated, these secondary coordinate systems have an axis along the diagonals ( $r$  and  $r'$ ), a perpendicular axis within the truss plane ( $t$  and  $t'$ ), and the third axis normal to the truss plane ( $s$  and  $s'$ ). The bottom chord was modeled continuous over the gusset plate due to significant ample splicing plates provided in testing.

As explained earlier, in this proposed analysis approach, the initial imperfection of gusset plate connections is applied via a single transverse load at the beginning of the compression diagonal member. The intent is simplicity and practicality of using this approach in common load rating practice. Figure 2(e) shows the imperfection simulating load in this modeling. This load simulates an initial imperfection following the connection's transverse sway buckling mode. Similarly, alternative loading may be utilized when other gusset plate buckling modes are of concern. Figure 2(f) shows the nonlinear steel Grade 50 material model (per the NCHRP research report) used for gusset plate shell elements.

For each of the four test simulations, nonlinear analyses were performed by incorporating different amounts of imperfection simulating loads. Each applied imperfection load is also presented by an equivalent out-of-plane imperfection eccentricity of the gusset plates at the compression diagonal. This imperfection eccentricity is comparable to the out-of-plane imperfection referred to in AASHTO MBE. The equivalent imperfection eccentricity for each applied imperfection simulating load was obtained by equating the out-of-plane bending moments at the joint center resulting from the imperfection simulating load with the equivalent imperfection eccentricity. Figure 3 shows the imperfection sensitivity curves for all four test simulations. Each imperfection sensitivity curve presents the rate for gusset plate capacity reduction for the increase in the magnitude of out-of-plane initial imperfection. As shown in Figure 3, for all four simulations, the imperfection sensitivity follows the same trend with a relatively sharper capacity reduction at the beginning for smaller amounts of initial imperfection, followed by an almost constant reduction rate for the larger amounts of initial imperfection.

For each test simulation, the calibrated nonlinear FEM analysis was recognized by identifying the initial imperfection, which resulted in about the same gusset plate capacity as reported for the experimental testing. Table 1 presents the calibrated FEM analyses for all four simulation cases. As shown, the calibrated imperfection loads increase for specimens with gusset plate thickness increases. A comparison between the gusset plate thicknesses and the corresponding

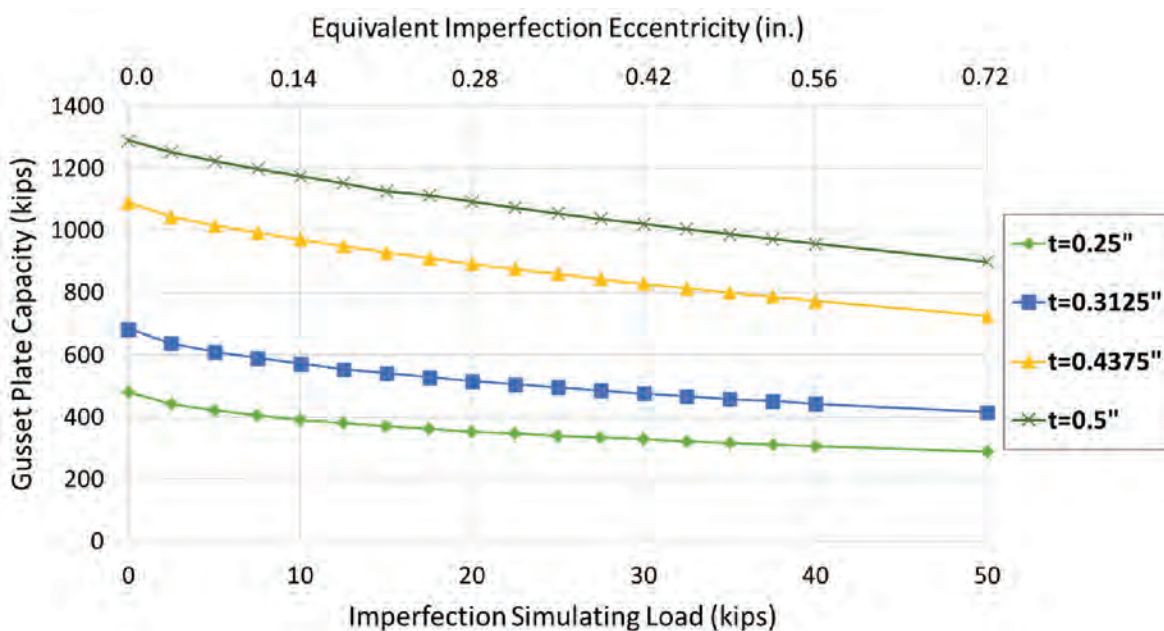


Fig. 3. Imperfection sensitivity curves for EI-WV-307SS test simulations.

**Table 1. Calibrated Gusset Plate Nonlinear FEM Analysis Results for E1-WV-307SS Test Simulations**

Simulations of NCHRP E1WV-307SS Specimens	Gusset Plate Thickness (in.)	Test Failure Resistance (kips)	Calibrated Imperfection Simulating Load (kips)	Calibrated Equivalent Imperfection Eccentricity (in.)	Applied Load Factor (ALF)	Simulation Resistance (kips)
	0.25 (¼)	380	12.5	0.180	0.266	381
	0.3125 (5/16)	530	17.5	0.250	0.369	529
	0.4375 (7/16)	817	32.5	0.460	0.567	812
	0.5 (½)	974	37.5	0.530	0.678	971

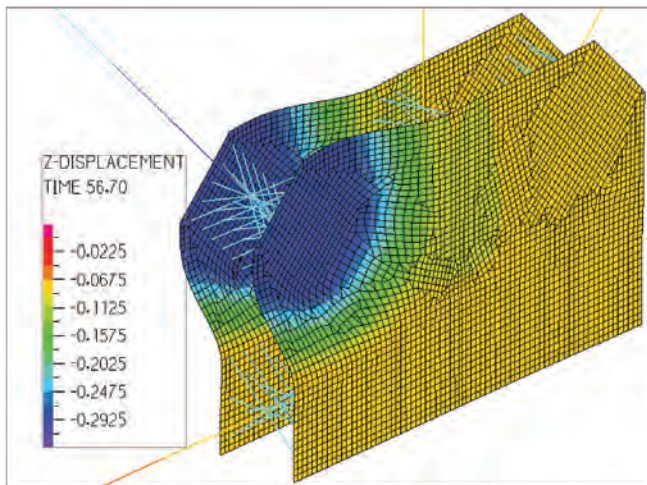
calibrated imperfection eccentricities presented in the table indicates their comparability with each other. In comparison to AASHTO MBE criteria for the magnitude of out-of-plane imperfection, this proposed method requires relatively larger imperfections due to excluding imperfection-induced locked-in stresses.

Figure 4 shows the calibrated nonlinear analysis results for the 0.4375-in. specimen at the failure stage (ALF = 0.567). Figure 4(a) shows the deformed gusset plates at the final analysis stage just before the analysis termination due to instability. The shown transverse displacement contours indicate sway buckling at the compression diagonal in conformity with the observed failure mode reported for the corresponding testing. Figure 4(b) illustrates the von Mises stress contours at the same final stage of the analysis. As shown, the gusset plates underwent significant yielding at the edge of the chord and vertical member at the compression diagonal side of the connection. This set of simulation analyses indicate the accuracy and reliability of the

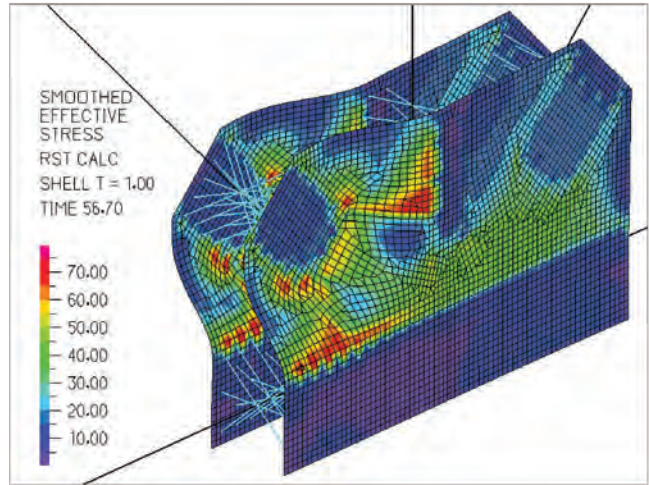
proposed nonlinear FEM analysis approach in the estimation of gusset plate capacity under inelastic buckling failure.

### UTILIZING THE PROPOSED APPROACH FOR A CASE STUDY

The proposed FEM analysis approach was utilized for investigating the gusset plate connection capacity for a subject steel truss shown in Figure 5. This example demonstrates the benefit of using this analysis approach for load rating practice. The gusset plate capacity of joint U9 connection as calculated by the LRFR method of AASHTO MBE is controlled by partial shear failure; the factored capacity equals 1792 kips for the compression diagonal member. The truncated Whitmore method, which is an alternative method in the AASHTO MBE Commentary, resulted in a gusset plate factored capacity of 2574 kips. This significant discrepancy resulted in inventory HL-93 load rating factors of 0.42 and 1.44 for the partial shear and truncated Whitmore methods,



(a) Lateral deformation contours



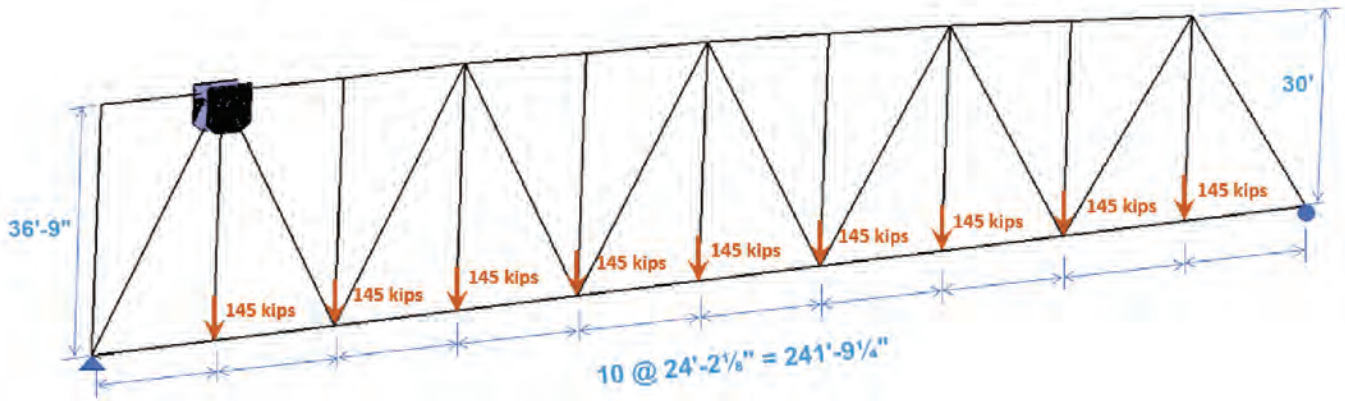
(b) Von Mises stress contours

Fig. 4. Gusset plate FEM nonlinear analysis results for E1-WV-307SS test, 0.3475-in. specimen with 32.5-kip imperfection load at ALF = 0.567.

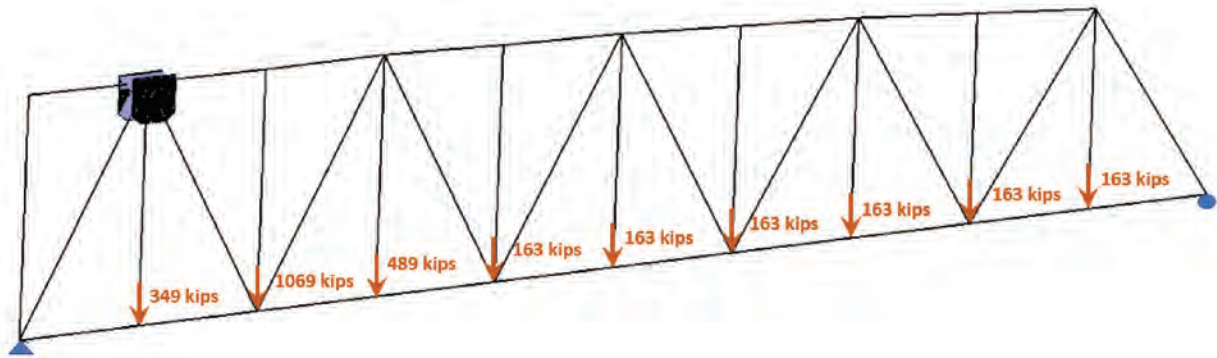
respectively. In the absence of utilizing a reliable and practical refined analysis method, a load rating engineer may conservatively recommend unnecessary retrofit for this gusset plate connection. With the aid of the proposed nonlinear FEM analysis approach, the capacity of the gusset plate connection was investigated in this study.

Figure 5 shows the geometry details of the studied steel

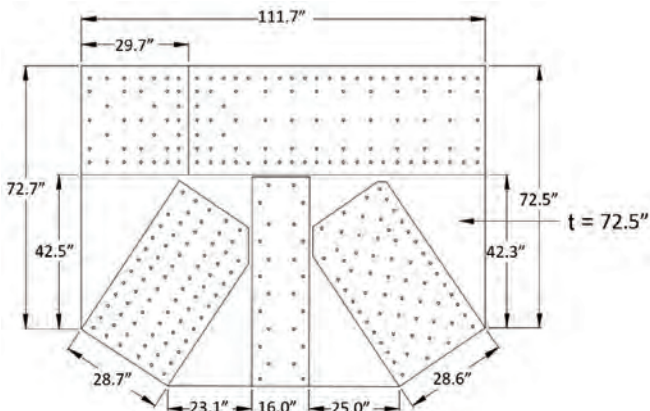
truss along with a nonlinear material model. The FEM modeling details for this subject truss and refined modeling of joint U9 are shown in Figure 1 and discussed in an earlier section of this paper. Figure 5(a) shows the geometry and applied dead loads for the subject truss. Simulation analysis was conducted by first applying the dead load in a single-step analysis. The analysis continued by gradually applying



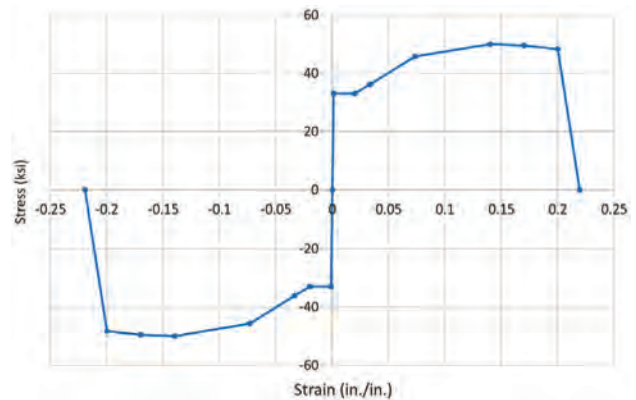
(a) Model geometry and dead loads



(b) Scaled-up live loads



(c) Details of gusset plates at joint U9



(d) Nonlinear material model for  $F_y = 33$  ksi carbon steel

Fig. 5. Studied steel truss.

scaled-up HL-93 live load reactions shown in Figure 5(b) until analysis termination due to structural instability. The geometry of joint U9 gusset plates is shown in Figure 5(c). As shown, both diagonals are slightly chamfered at the connection. Late 1930s carbon steel with  $F_y = 33$  ksi was used for truss members and gusset plates. The corresponding nonlinear material model used for gusset plates is shown in Figure 5(d). The top chord splice plates were not included in the model, and instead, a continuous top chord was considered in this simulation. This was reasonable because the chords are supplied with splice plates on all four faces, which significantly limits the contribution of gusset plates in taking splicing forces. For other cases where a significant splicing action is expected, the modeling can be revised by discontinuing the chord and adding splice plates and rigid links and following the same approach used for gusset plate modeling.

Figure 6 shows an imperfection sensitivity curve for the subject gusset plate connection developed by conducting 3D nonlinear analyses for a range of imperfection loads and associated eccentricities. As shown, the gusset plate capacity reduction is relatively slow for an initial increase in imperfection load/eccentricity, but the curve becomes steeper for larger imperfections. For this subject gusset plate connection, the imperfection eccentricity was assumed equal to the gusset plate thickness. According to the imperfection sensitivity curve, this imperfection eccentricity

corresponds to the gusset plate capacity of 2503 kips. Comparing the gusset plate capacity obtained from the refined analysis with partial shear and truncated Whitmore method capacities indicates that the refined analysis confirms the truncated Whitmore method's estimation. Accordingly, this also suggests no need for gusset plate retrofit. Figure 7 presents the nonlinear FEM refined analysis results, at the final stage before buckling failure, for the subject gusset plate connection with the imperfection eccentricity equals to the gusset plate thickness. Gusset plate transverse displacement contours are shown in Figure 7(a). As shown, buckling of gusset plates at the compression diagonal is the failure mode for the subject connection. Von Mises stress contours presented in Figure 7(b) indicate significant gusset plate yielding prior to final inelastic buckling. As shown, the gusset plates mostly yield along the horizontal section at the bottom edge of the top chord before failure.

### SUMMARY AND CONCLUSIONS

A 3D nonlinear refined FEM analysis approach for gusset plate capacity estimation is proposed in this paper. The main intention of this approach is to provide a less complicated but still reliable refined FEM modeling and analysis technique to be utilized in common practice of gusset plate load rating. For this purpose, the proposed modeling excludes modeling details related to failure modes that can

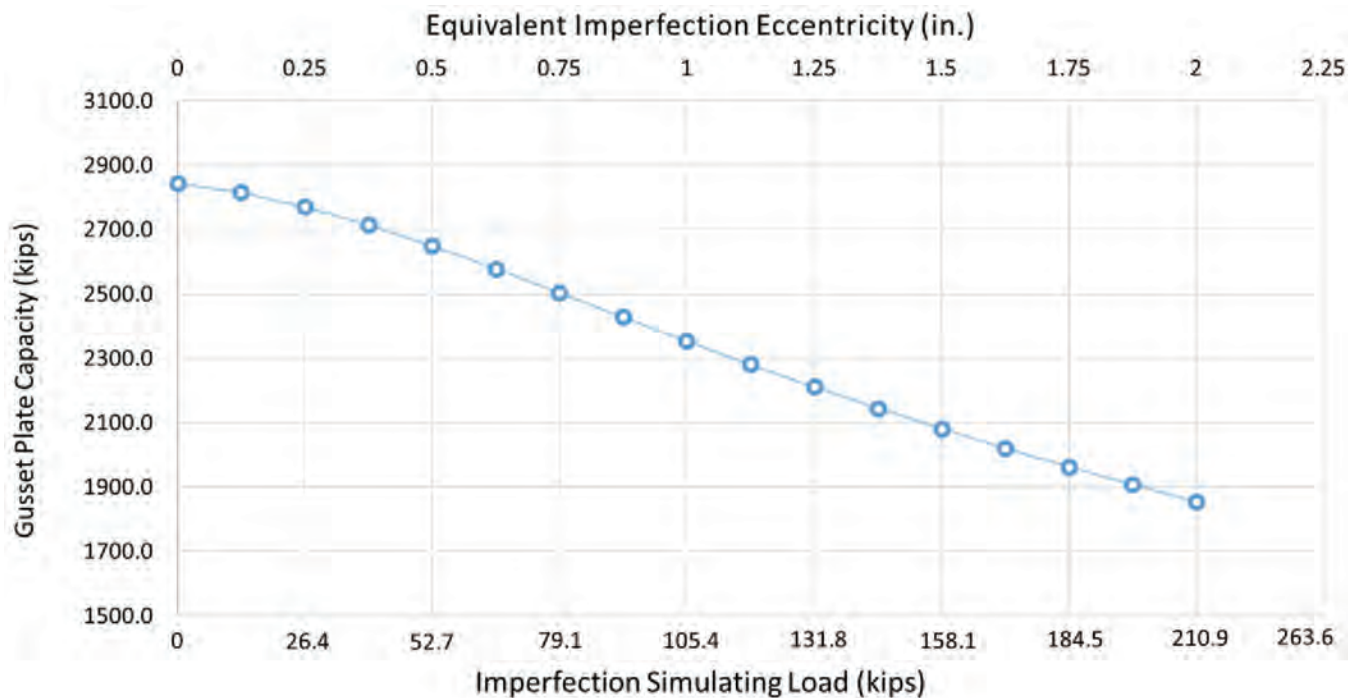


Fig. 6. Imperfection sensitivity curve for gusset plate connection at joint U9.

be confidently estimated with current design calculations. Accordingly, the proposed modeling deals with yielding and buckling failure modes of gusset plate connections that are associated with significant material, geometric, and boundary condition uncertainties. Incorporating initial imperfections to capture gusset plate connection buckling failure modes results in a significant complication in FEM modeling. In this proposed approach, the incorporation of initial imperfection is facilitated by applying an imperfection simulating force. Due to uncertainty about initial imperfection, this approach includes developing an imperfection sensitivity curve by investigating the rate of gusset plate capacity reduction for a reasonable range for the equivalent imperfection eccentricity. An imperfection sensitivity curve would provide a load rating engineer more confidence in estimating gusset plate capacity.

Reliability of the proposed refined analysis approach was investigated by numerically simulating a set of experimental tests on a gusset plate connection conducted under NCHRP Project 12-84. The validation analysis of this study demonstrated the reliability of the proposed approach in estimating gusset plate capacity at inelastic buckling failure as compared to actual tests. Calibration with test results indicated that a relatively larger out-of-plane imperfection eccentricity is required for this proposed approach as compared to the magnitude of imperfection criteria provided in the AASHTO MBE. This is due to not including imperfection locked-in stresses in this proposed approach. The proposed approach was utilized for a subject gusset plate case where the partial shear and truncated Whitmore method resulted in significantly different estimations for the gusset plate capacity and subsequent uncertainty about

the need for gusset plate retrofit. The refined FEM analysis resulted in a capacity estimation comparable with the truncated Whitmore method estimation and confirmed the unnecessary of gusset plate retrofit. As indicated, engineers should be aware that the partial shear method may result in a significantly conservative load rating for gusset plates. For cases where the partial shear method load rating requires a retrofit, the truncated Whitmore method can be used as an alternative approach. Divergence of calculated load ratings between the two methods will roughly indicate whether using refined FEM analysis will be beneficial or not. Further research is needed to study if the truncated Whitmore method will always provide an estimate of the gusset plate capacity that is comparable to the refined FEM analysis method.

As demonstrated, gusset plate load rating practice will significantly benefit from utilizing more practical gusset plate refined FEM analysis approaches such as the one presented in this paper. Bridge owner agencies also will benefit by avoiding costs and efforts of unnecessary retrofits. Further investigations are required to understand the benefits and limitations of this proposed approach and develop guidelines for its application in load rating practice.

## REFERENCES

- AASHTO (2018), *The Manual for Bridge Evaluation*, American Association of State Highway and Transportation Officials, Washington, D.C.
- Adina (2017), ADINA v9.3, Adina R&D, Inc., Watertown, Mass.

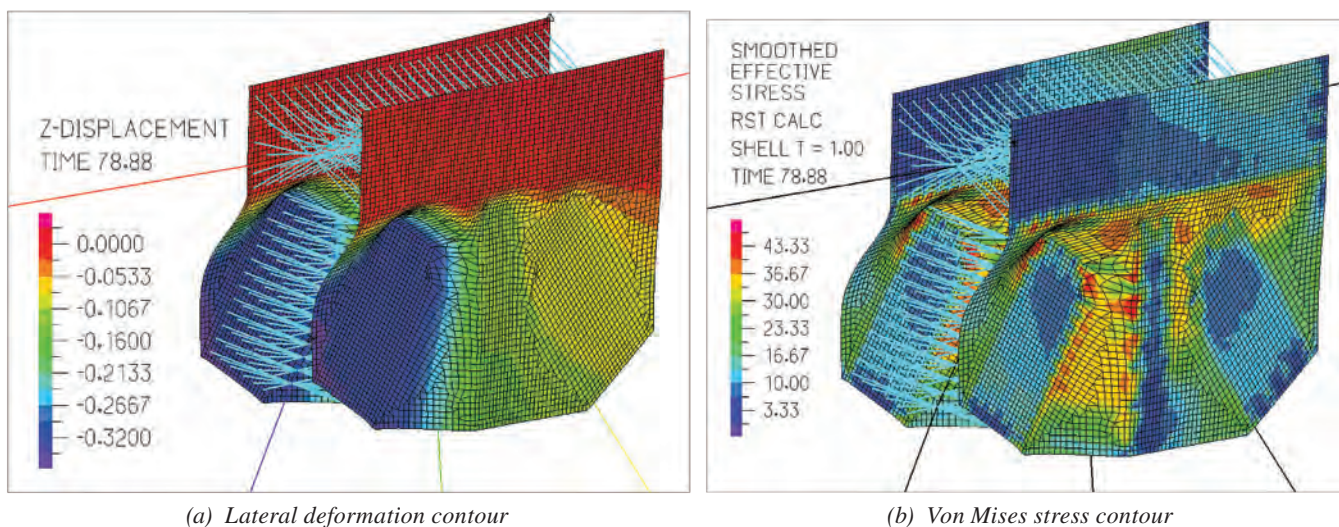


Fig. 7. Gusset plate FEM nonlinear analysis results for gusset plate connection at joint U9 with 0.75-in. imperfection eccentricity.



- Hardin, B.O. (1958), "Experimental Investigation of the Primary Stress Distribution in the Gusset Plates of a Double Plane Pratt Truss Joint with Chord Splice at the Joint," Doctoral Dissertation, University of Kentucky, Lexington, Ky.
- Irvan, W.G. (1957), "Experimental Study of Primary Stresses in Gusset Plates of a Double Plane Pratt Truss," Doctoral Dissertation, University of Kentucky, Lexington, Ky.
- NTSB (2008), *Collapse of I-35W Highway Bridge, Minneapolis, Minnesota, August 1, 2007*, Accident Report NTSB/HAR-08/03, PB2008-916203, National Transportation Safety Board, Washington, D.C.
- Ocel, J.M. (2013), *Guidelines for the Load and Resistance Factor Design and Rating of Riveted and Bolted Gusset-Plate Connections for Steel Bridges*, NCHRP Web-Only Document 197, National Cooperative Highway Research Program, Washington, D.C.
- Sandel, J.A. (1950), "Photoelastic Analysis of Gusset Plates," Doctoral Dissertation, University of Tennessee, Knoxville, Tenn.
- Vasarhelyi, D.D. (1971), "Tests of Gusset Plate Models," *Journal of the Structural Division*, Vol. 97, No. ST2, pp. 665–678.
- Whitmore, R.E. (1952), *Experimental Investigation of Stresses in Gusset Plates*, Engineering Experiment Station, University of Tennessee, Knoxville, Tenn.
- Wyss, T. (1926), *Die Kraftfelder in festen elastischen Körpern und ihre praktischen Anwendungen*, Verlag von Julius Springer, Berlin, Germany.



# Review of Local Buckling Width-to-Thickness Limits

BEN W. SCHAFFER, LOUIS F. GESCHWINDNER, TOM SABOL, and CHIA-MING UANG

---

## ABSTRACT

This paper provides a review of local buckling width-to-thickness limits (also known as  $w/t$  or  $\lambda$ ) employed in the ANSI/AISC 360-16 *Specification for Structural Steel Buildings* (2016b), hereafter referred to as AISC 360, and ANSI/AISC 341-16 *Seismic Provisions for Structural Steel Buildings* (2016a), hereafter referred to as AISC 341. The review was conducted by a task group formed to address potential changes in the next and/or future editions of the AISC *Specifications*. A comprehensive review of existing local buckling limits was completed, including detailing the underlying assumptions and the objectives of the existing limits. In addition, particular attention was given to the potential impact of adopting newer steel materials on the local buckling limits and to considerations of web-flange interaction in local buckling. Further, new methods that have been developed to address local buckling in structural steel design were also examined. It was found that in AISC 360, some  $\lambda_r$  limits for flexure may not be well aligned with intended objectives, and while all  $\lambda_p$  limits for flexure ensure the plastic moment may be achieved, rotation objectives are not consistently implemented. Review of  $\lambda_{md}$  and  $\lambda_{nd}$  in AISC 341 reveals complications with implementing expected yield stress in the slenderness parameters and highlights the large number of varied objectives for these limits in seismic design, as well as a need for improvements—particularly for deep wide-flange columns. In general, it is found that only minor changes are potentially needed to current width-to-thickness,  $w/t$ , limits. Thus, in most cases, it is expected that AISC design can continue unchanged, with the exception of the improved criteria for deep columns. To minimize change while still expanding opportunity, newer local buckling cross-section classification methods could be permitted as alternatives rather than used as replacements to current  $w/t$  limits so that advantages of the newer approaches can be utilized when beneficial.

---

## INTRODUCTION

During the development of the 2022 editions of AISC 360 (2016b) and AISC 341 (2016a), the AISC Committee on Specifications determined that a review of current local buckling width-to-thickness limits (also known as  $w/t$  or  $\lambda$ ) would be useful and appointed a task group, of which the first author was chair, to study the issue. Concerns about web-flange interaction in the cyclic response of deep columns, a desire to be forward-thinking regarding the adoption of higher strength steels, and an interest in alternative methods that had been developed to address local buckling were some of the motivating reasons for the formation of the task group. The task group was charged with reviewing all existing  $w/t$  limits, explicitly stating the objective of these limits and if current criteria achieve desired objectives, examining the impact of material properties and web-flange interaction on the  $w/t$  limits, exploring alternatives

to current methods for local buckling control, and finally to provide recommendations for the next and future editions of the AISC 360 and 341 *Specifications*. The objective of this paper is to provide a summary of the task group's report from Schaffer et al. (2020).

## BACKGROUND

Classically, steel cross sections are conceptualized as being composed of a series of connected long plates. The plates (also known as elements) of the cross section with continuous connection along both longitudinal edges, such as the web of an I-section, are known as stiffened elements; while plates with connection along only one longitudinal edge, such as half the flange of an I-section, are known as unstiffened elements. The elastic buckling of long plates, using Kirchoff thin plate theory (Allen and Bulson, 1980), leads to the following classical expression:

$$F_{cr} = k \frac{\pi^2 E}{12(1-\nu^2)} \left(\frac{t}{w}\right)^2 \quad (1)$$

where  $F_{cr}$  is the elastic plate buckling stress;  $E$  is the material modulus of elasticity;  $\nu$  is the material Poisson's ratio;  $t$  and  $w$  define the plate thickness and width, respectively; and the plate buckling coefficient,  $k$ , is a function of the loading and boundary conditions. Solutions for  $k$  exist for a wide variety of conditions and can consider multiple attached elements to form a full cross section (Allen and Bulson, 1980; Seif and Schaffer, 2010; Gardner et al., 2019). However, only the simplest values are commonly used in

---

Ben W. Schaffer, Professor, Johns Hopkins University, Baltimore, Md. Email: schaffer@jhu.edu (corresponding)

Louis F. Geschwindner, Professor Emeritus, Pennsylvania State University, State College, Pa. Email: lfg@psu.edu

Tom Sabol, Adjunct Professor, University of California–Los Angeles, Los Angeles, Calif. Email: tsabol@ucla.edu

Chia-Ming Uang, Professor, University of California–San Diego, San Diego, Calif. Email: cmu@ucsd.edu

---

Paper No. 2021-04

ISSN 0013-8029

ENGINEERING JOURNAL / FIRST QUARTER / 2022 / 65

design—for example,  $k$  of 4 for a stiffened element in uniform compression or  $k$  of 0.425 for an unstiffened element in uniform compression. See Allen and Bulson (1980), Salmon et al. (2009), and Ziemian (2010) for further discussion and a more thorough background.

Structural steel design specifications worldwide use  $w/t$  limits to provide engineers with guidance on the impact of local buckling on their designs. The strength and/or curvature capacity of beams is the archetypical case for this application and is illustrated in Figure 1, which includes the nomenclature of AISC 360: slender, noncompact, and compact, as well as that of Eurocode/EN 1993 (CEN, 2004): Class 4, Class 3, Class 2, and Class 1, where  $M_y$  is the moment at first yield,  $M_p$  the plastic moment,  $\kappa$  the curvature, and  $\kappa_p$  the plastic curvature of the beam when  $M_p$  is first reached.

If local plate buckling behaved in a manner similar to global flexural buckling (post-buckling neutral), then  $w/t$  limits would be easy to establish because elastic buckling itself would provide a useful limit. However, unlike flexural buckling of a member, local buckling of a plate is not post-buckling neutral—local plate buckling is post-buckling stable. Thus, design rules do not generally use  $F_{cr}$  for the plate as directly as one would use for flexural buckling. Further, the elastic plate buckling provides no consideration for material nonlinearity in the form of Equation 1. Therefore, development of  $w/t$  limits has classically relied on comparisons to experimental testing. If one can establish a buckling stress—say, at a stress of  $aF_y$ —that meets a desired objective (e.g.,  $M_p$ , a target rotation, etc.), then the resulting  $w/t$  limit can be simplified as follows:

$$F_{cr} = k \frac{\pi^2 E}{12(1-\nu^2)} \left(\frac{t}{w}\right)^2 = aF_y \quad (2)$$

$$\left(\frac{w}{t}\right)_{limit} = \sqrt{\frac{k\pi^2}{a12(1-\nu^2)}} \sqrt{\frac{E}{F_y}} = C \sqrt{\frac{E}{F_y}} \quad (3)$$

Note that the buckling stress in Equation 2 is a reference stress only and does not rigorously reflect a bifurcation stress in the plate, and  $a$  is a multiplier on  $F_y$  specific to local buckling effects. A typical observation from experiments is that an element with  $F_{cr} \cong 2F_y$  is needed to develop first yield at the extreme fiber in a full section. If the plate buckling coefficient,  $k$ , is also assumed, then the coefficient  $C$  may be found. These coefficients are tabulated in AISC 360, Table B4.1. For example, for the flange of a rolled shape to develop the plastic moment, AISC 360 provides:

$$\begin{aligned} \lambda_p &= \left(\frac{w}{t}\right)_p \\ &= C \sqrt{\frac{E}{F_y}} \\ &= 0.38 \sqrt{\frac{E}{F_y}} \end{aligned} \quad (4)$$

In much of the literature, a related but slightly different approach has been taken to finding coefficients similar to  $C$ . A nondimensional slenderness is defined as  $\lambda^* = \sqrt{F_y/F_{cr}}$ , and this parameter is examined to determine when the objective is met. The two methods are related:

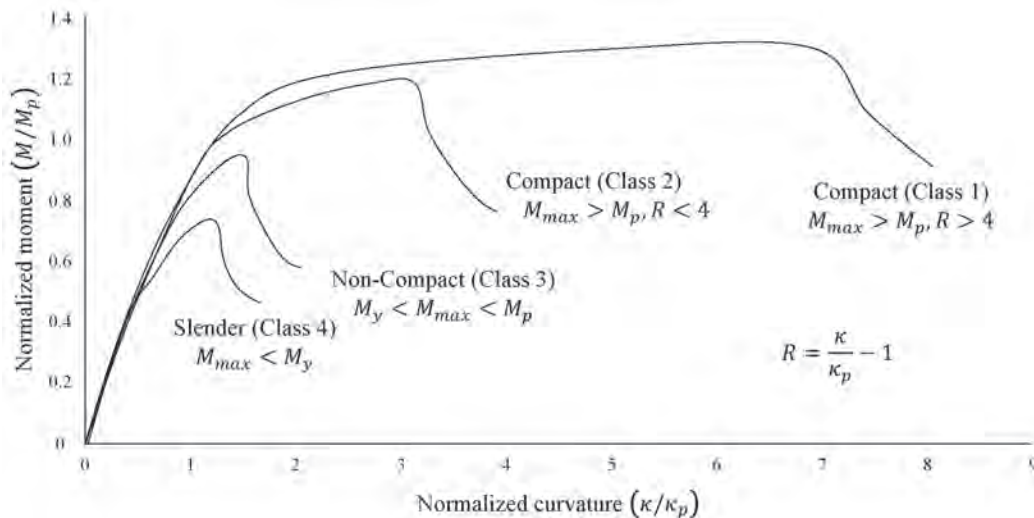


Fig. 1. Moment-curvature behavior of beams with different  $w/t$  limits (based on Wilkinson and Hancock, 1998).

$$\begin{aligned}\lambda^* &= \sqrt{\frac{F_y}{F_{cr}}} \\ &= \sqrt{\frac{1}{a}} \\ &= \sqrt{\frac{12(1-\nu^2)}{k\pi^2 E}} \left(\frac{w}{t}\right)\end{aligned}\quad (5)$$

For example, in Winter's classical work (1947), he found that  $\lambda^* = 0.673$  or  $a = 2.21$  was an accurate boundary between elements that could develop their first yield capacity and those that required additional reductions due to local buckling.

A variety of approaches have been employed to develop  $w/t$  limits for design. The most common approach is wholly experimental; however, sometimes the experiments have been conducted on idealized elements/plates and sometimes on entire sections. In some cases, researchers directly try to fit their data to the coefficient  $C$  of Equation 3, in other cases the focus is on finding the  $a$  or  $\lambda^*$  of Equation 2 or 5. Also, in some instances researchers have used Equation 3 in some form to backsolve for  $k$ . This can lead to unintended consequences when such  $k$  values are reinserted into elastic buckling expressions and used in other settings.

It is worth noting that in developing  $w/t$  limits, Equation 1 has sometimes been modified to be aligned with the tangent modulus theory and/or application of plasticity reduction factors to the modulus (Ziemian et al., 2010). These approaches can be problematic. Although flexural buckling of columns may be one-dimensional, plate buckling is inherently two-dimensional, and simple one-dimensional reductions to the modulus and ignoring the inherent post-buckling of the plates can lead to erroneous conclusions about strength and  $w/t$  limits. In several instances, researchers have found it useful to conceptualize Equation 1 in terms of one-dimensional strain instead of stress:

$$\epsilon_{cr} = \frac{F_{cr}}{E} = k \frac{\pi^2}{12(1-\nu^2)} \left(\frac{t}{w}\right)^2 \quad (6)$$

Equation 6 has the desirable feature of being independent of modulus of elasticity and thus, researchers and specifications in structural thermoplastics or gradual yielding materials (e.g., stainless steel) have often preferred this form. If one follows Equation 6 in establishing  $w/t$  limits, then instead of determining an  $F_{cr}$  in excess of  $F_y$  (i.e.,  $aF_y$ ), one thinks in terms of multiples of the yield strain (i.e.,  $a\epsilon_y$ ). This is more natural in inelastic cases, particularly for plastic redistribution or seismic design. It is also worth noting that in the classical literature for developing steel  $w/t$  limits, it was sometimes common to consider  $w/t$  limits that achieve a certain average applied strain. A typical target was for the element to sustain a strain up to the initiation of strain hardening, or three or four times the strain at first

yield,  $\epsilon_y$ . The format of Equation 6 is particularly convenient for such considerations, though one must be careful in that the critical strain is not a direct predictor of the strain that an element can sustain, but rather a parameter that is correlated with the desired strain. See Schafer et al. (2020) for further discussion.

## NONSEISMIC AISC 360 LOCAL BUCKLING LIMITS

AISC 360, Section B4, provides local buckling ( $w/t$ ) limits for compression,  $\lambda_r$ , and for flexure,  $\lambda_r$  and  $\lambda_p$ . These limits are utilized to determine domains in which local buckling influences the nominal strength, and those domains are used as primary parameters for establishing strength reductions. A thorough review of AISC 360 local buckling limits is provided herein; however, additional beneficial information is also provided in AISC 360, Section B4.1 Commentary, particularly for round sections that are not covered in detail here.

### Objective of AISC 360 Local Buckling Limits

As implemented, the specific objectives of the AISC local buckling limits depend on the loading. For members under axial compression,  $\lambda_r$  provides the slender/nonslender limit for the section; specifically for  $w/t \leq \lambda_r$ , the cross section can develop its squash (yield) strength—that is,  $P_y = A_g F_y$ . For members under flexure,  $\lambda_r$  provides the noncompact/slender limit for the section; specifically for  $w/t \leq \lambda_r$  the cross section can develop at least its elastic limit in bending—that is,  $M_r$ . In AISC 360,  $M_r$  varies by section and limit state and may be defined as  $M_r = M_y = S F_y$  or  $M_r = S F_L = 0.7 M_y$ , ostensibly to consider residual stresses. In flexure,  $\lambda_p$  provides the compact/noncompact limit for the section; for  $w/t \leq \lambda_p$ , the cross section can develop its ideal fully plastic capacity in bending—that is,  $M_p = Z F_y$ .

For members under flexure, the use of either  $F_y$  or  $F_L$  in determining  $\lambda_r$  creates complications. For Table B4.1b, Case 11 (flanges of I-shaped built-up sections), when  $w/t = \lambda_r$ , the cross section can develop its first yield capacity considering residual stresses—that is,  $M_r = S F_L$ , where  $F_L = F_y - F_r$  and  $F_r$  is the assumed level of residual stress. Other elements (e.g., webs of I-shaped sections) may have implicit consideration of residual stresses in determining  $\lambda_r$ , but do not use  $F_L$  in the final width-to-thickness limit [see Schafer et al. (2020) Appendix 1 for further details]. Note, in the 1999 AISC LRFD *Specification* (AISC, 1999), a precursor to AISC 360, the use of  $F_L = F_y - F_r$  in the flexural limits was far more pervasive; the following flexural cases used  $F_L$ : flanges of rolled I-shapes or channels; flanges of built-up I-shapes; and flanges of HSS, box sections, or cover plates. Also,  $F_r = 10$  ksi was used for rolled shapes, and  $F_r = 16.5$  ksi was used for welded shapes.

In relation to  $\lambda_r$ , AISC 360, Section B4.1 Commentary, states “Noncompact sections can develop partial yielding in compression elements before local buckling occurs but will not resist inelastic local buckling at the strain levels required for a fully plastic stress distribution. Slender-element sections have one or more compression elements that will buckle elastically before the yield stress is achieved.” As currently stated in AISC 360, the noncompact/slender boundary,  $\lambda_r$ , is poorly defined, and interpretation of  $F_y$  vs.  $F_L$  hinges on interpretation of plate behavior at the boundary between “buckling elastically” and resisting inelastic buckling “but not a full plastic stress.” Currently, different cross sections in Chapter F use different approaches to this issue—as discussed later in this paper. In general, the use of  $F_L$  relaxes (liberalizes) the  $w/t$  limits. A justification given for this application in Salmon et al. (2009) is that this relaxation should be allowed for cases where key residual stresses are tensile in nature.

While  $\lambda_p$  specifically addresses strength, there is some confusion over whether or not it addresses rotation/curvature capacity. For example, see Figure 1, where the term compact refers both to Class 1 and Class 2 sections. AISC 360, Section 1.3.2b Commentary, states that “compact sections ... possess a rotation capacity,  $R_{cap}$ , of approximately three,” where  $R_{cap}$  is the rotation at which the post-peak response drops back below  $M_p$  normalized by the elastic rotation at which  $M_p$  is first reached. In some cases (e.g., Table B4.1b, Cases 17 and 19 for elements of HSS sections), the  $\lambda_p$  limit was specifically selected to meet a minimum  $R_{cap}$  of 3. In other cases, as detailed in Appendix 1 of Schafer et al. (2020), there is not a direct connection between a target rotational capacity and the selected  $w/t$  limit, or the target rotational capacity was not 3. However, in available experiments on I-shaped beams that meet the  $\lambda_p$  criteria, all sections develop at least an  $R_{cap}$  of 2.9, and in many cases far in excess of this (Schafer et al., 2020). The AISC 360  $\lambda_p$  limits provide strength  $M_p$  and also supply a level of strain capacity in the element in excess of the yield strain. In many instances, researchers targeted a strain capacity up to the onset of strain hardening in the material [see Appendix 1 of Schafer et al. (2020) and AISC 341, Section D1.1b Commentary]. The end result of these varied approaches is that the section typically can sustain a rotation capacity of approximately 3 or more. One notable exception is Table B4.1b, Case 14: tee-stems in Chapter F of AISC 360,  $\lambda_p$  is associated with the first yield moment,  $M_y$ , instead of the fully plastic moment,  $M_p$ .

### Comparison with Eurocode

Provided in this paper is a comparison of the local buckling limits between AISC 360 and Eurocode EN 1993-1-1 (CEN, 2004). Additional comparisons to ANSI/AISI S100-16, *North American Specification for the Design*

*of Cold-Formed Steel Structural Members* (2016), herein referred to as AISI S100; the 8th Edition of the AASHTO *LRFD Bridge Design Specification* (AASHTO, 2017); and *Recommendations for Limit State Design of Steel Structures* from the Architectural Institute of Japan (AIJ, 2010), herein referred to as AIJ, are provided in Schafer et al. (2020). Due to its similar design rules with respect to local buckling and maturity with respect to application, direct comparison of AISC 360  $w/t$  limits to those of Eurocode is desirable. Table 5.2 in Part 1-1 of Eurocode 3 is the counterpart to AISC 360, Table B4.1. However, the format for presenting the limits is not identical. For a typical  $w/t$  limit, Eurocode expresses the limit as:

$$\left(\frac{w}{t}\right)_{limit} \leq C_{EN} \sqrt{\frac{235}{F_{yMPa}}} \quad (7)$$

where  $F_{yMPa}$  indicates the yield stress in units of MPa, and  $C_{EN}$  is a nondimensional coefficient provided in Eurocode. For a direct comparison with AISC’s format of  $C\sqrt{E/F_y}$ , the equivalent  $C$  coefficient in AISC’s format may be found from:

$$C_{eq} = C_{EN} \sqrt{\frac{235}{E_{MPa}}} \text{ or } 0.0343C_{EN} \quad (8)$$

where  $E_{MPa}$  indicates the modulus of steel in MPa. Comparison for compression is provided in Table 1 and for flexure in Table 2, wherein cases with substantial differences are highlighted in gray within the tables.

For compression members, AISC stiffened element  $w/t$  limits are quite similar to Eurocode. However, AISC unstiffened element  $w/t$  limits are different from Eurocode; for example, the AISC  $w/t$  limit is 36% higher than Eurocode for the stem of a tee section. For flexural members, AISC and Eurocode have greater differences. In flexure, AISC  $w/t$  limits are generally similar to Eurocode for stiffened elements but dissimilar, sometimes significantly, for unstiffened elements. AISC’s unstiffened element flange  $\lambda_p$  limit is greater than even Class 2 for Eurocode, which implies that Eurocode would not predict even minimal rotational capacity for members with flanges at the AISC  $\lambda_p$  limit. The AISC  $\lambda_r$  limit for unstiffened elements is more than double Eurocode Class 3, even for the simple case of a rolled flange.

Additional differences related to  $w/t$  limits between the standards also exist. AISC differentiates between rolled and built-up shapes, while Eurocode does not. AISC includes web-flange interaction for flanges of built-up shapes, while Eurocode does not. Note that AISC differentiates between compression and flexural members when defining the  $w/t$  limits; Eurocode does not. Instead, Eurocode considers the assumed stress on an element more explicitly than AISC. Thus, Eurocode provides  $w/t$  limits that consider arbitrary compression and bending. In minor-axis bending of

Table 1. AISC 360 $w/t$ Limits for Compression Elements in Members Subject to Axial Compression and Eurocode $w/t$ Limits for Elements in Uniform Compression			
	Element Description	AISC 360	Eurocode
<b>Case</b>	<b>Unstiffened</b>	$\lambda_r$	<b>Class 3</b>
1	Rolled flange	$0.56 \sqrt{\frac{E}{F_y}}$	$0.48 \sqrt{\frac{E}{F_y}}$
2	Built-up flange	0.38 to $0.56 \sqrt{\frac{E}{F_y}}$ <sup>a</sup>	$0.48 \sqrt{\frac{E}{F_y}}$
3	Angle leg, other	$0.45 \sqrt{\frac{E}{F_y}}$	$0.51 \sqrt{\frac{E}{F_y}}$
4	Stem of tee	$0.75 \sqrt{\frac{E}{F_y}}$	$0.48 \sqrt{\frac{E}{F_y}}$
	<b>Stiffened</b>		
5	Rolled web	$1.49 \sqrt{\frac{E}{F_y}}$	$1.44 \sqrt{\frac{E}{F_y}}$
6	HSS wall	$1.40 \sqrt{\frac{E}{F_y}}$	$1.44 \sqrt{\frac{E}{F_y}}$
7	Cover plate	$1.40 \sqrt{\frac{E}{F_y}}$	$1.44 \sqrt{\frac{E}{F_y}}$
8	Other	$1.49 \sqrt{\frac{E}{F_y}}$	$1.44 \sqrt{\frac{E}{F_y}}$
	<b>Round</b>		
9	Round HSS/pipe	$0.11 \sqrt{\frac{E}{F_y}}$	$0.11 \sqrt{\frac{E}{F_y}}$

<sup>a</sup> AISC provisions are a function of web  $h/t_w$ , bounds provided here, shading highlights substantial differences.

unstiffened elements, for example, considering the stress distribution explicitly as Eurocode does can lead to stark differences depending on whether or not the tip of the unstiffened element is in tension or compression. Generally, Eurocode's  $w/t$  limits are more closely aligned with the underlying assumptions of the effective width method as, for example, implemented in AISI S100 (2016).

### Plate Buckling Assumptions Implied in AISC 360 $w/t$ Limits

If one considers a given  $w/t$  limit expressed by the coefficient  $C$  of Equation 3, this coefficient is directly connected to (1) the assumed plate buckling coefficient,  $k$  (i.e., the loading and boundary conditions of the plate), and (2) the plate slenderness,  $\lambda^*$ , required to sustain the desired load or stress/strain. Combining Equation 3 and 5 at the  $\lambda_r$  for pure compression results in:

$$\begin{aligned} \lambda_r &= \left(\frac{w}{t}\right)_r & (9) \\ &= \lambda^* \sqrt{\frac{k\pi^2}{12(1-\nu^2)}} \sqrt{\frac{E}{F_y}} \\ &= C \sqrt{\frac{E}{F_y}} \end{aligned}$$

The most complete discussion of the underlying assumptions for the AISC 360  $w/t$  limits can be found in Salmon et al. (2009). For the  $\lambda_r$  limits of compression members, Salmon et al. provide most of the assumed  $\lambda^*$  and plate buckling coefficients,  $k$ . With these assumed values, Table 3 shows that the resulting  $\lambda_r$  limits match AISC 360.

Examination of the assumed  $k$  and  $\lambda^*$  values based on Equation 9 for flexure are more complex. Nonetheless, it can be completed with some success and is provided for

**Table 2. AISC 360 w/t Limits for Compression Elements in Flexural Members  
and Eurocode w/t Limits for Elements with Compressive Stress**

	<b>Element Description</b>	<b>AISC 360</b>	<b>Eurocode</b>	<b>Eurocode</b>	<b>AISC 360</b>	<b>Eurocode</b>
<b>Case</b>	<b>Unstiffened</b>	$\lambda_p$	<b>Class 1</b>	<b>Class 2</b>	$\lambda_r$	<b>Class 3</b>
10	Rolled flange	$0.38\sqrt{\frac{E}{F_y}}$	$0.31\sqrt{\frac{E}{F_y}}$	$0.34\sqrt{\frac{E}{F_y}}$	$1.0\sqrt{\frac{E}{F_y}}$	$0.48\sqrt{\frac{E}{F_y}}$
11	Built-up flange <sup>a</sup>	$0.38\sqrt{\frac{E}{F_y}}$	$0.31\sqrt{\frac{E}{F_y}}$	$0.34\sqrt{\frac{E}{F_y}}$	0.56 to $0.83\sqrt{\frac{E}{F_y}}$	$0.48\sqrt{\frac{E}{F_y}}$
12	Angle leg, other	$0.54\sqrt{\frac{E}{F_y}}$	$0.31\sqrt{\frac{E}{F_y}}$	$0.34\sqrt{\frac{E}{F_y}}$	$0.91\sqrt{\frac{E}{F_y}}$	$0.48\sqrt{\frac{E}{F_y}}$
13	Flange in minor axis <sup>b</sup>	$0.38\sqrt{\frac{E}{F_y}}$	$0.31$ to $0.63\sqrt{\frac{E}{F_y}}$ $0.31$ to $0.93\sqrt{\frac{E}{F_y}}$	$0.34$ to $0.68\sqrt{\frac{E}{F_y}}$ $0.34$ to $1.02\sqrt{\frac{E}{F_y}}$	$1.0\sqrt{\frac{E}{F_y}}$	$0.48$ to $1.44\sqrt{\frac{E}{F_y}}$
14	Stem of tee <sup>b</sup>	$0.84\sqrt{\frac{E}{F_y}}$	$0.31$ to $0.62\sqrt{\frac{E}{F_y}}$ $0.31$ to $0.93\sqrt{\frac{E}{F_y}}$	$0.34$ to $0.68\sqrt{\frac{E}{F_y}}$ $0.34$ to $1.02\sqrt{\frac{E}{F_y}}$	$1.52\sqrt{\frac{E}{F_y}}$	$0.48$ to $1.44\sqrt{\frac{E}{F_y}}$
<b>Stiffened</b>						
15	Web (doubly symmetrical shape)	$3.76\sqrt{\frac{E}{F_y}}$	$2.46\sqrt{\frac{E}{F_y}}$	$2.84\sqrt{\frac{E}{F_y}}$	$5.70\sqrt{\frac{E}{F_y}}$	$4.25\sqrt{\frac{E}{F_y}}$
19	Web HSS and box	$2.42\sqrt{\frac{E}{F_y}}$	$2.46\sqrt{\frac{E}{F_y}}$	$2.84\sqrt{\frac{E}{F_y}}$	$5.70\sqrt{\frac{E}{F_y}}$	$4.25\sqrt{\frac{E}{F_y}}$
16	Web (singly symmetrical shape)	c	c	c	$5.70\sqrt{\frac{E}{F_y}}$	c
17	Flange HSS	$1.12\sqrt{\frac{E}{F_y}}$	$1.13\sqrt{\frac{E}{F_y}}$	$1.65\sqrt{\frac{E}{F_y}}$	$1.40\sqrt{\frac{E}{F_y}}$	$1.44\sqrt{\frac{E}{F_y}}$
18	Flange cover plate	$1.12\sqrt{\frac{E}{F_y}}$	$1.13\sqrt{\frac{E}{F_y}}$	$1.65\sqrt{\frac{E}{F_y}}$	$1.40\sqrt{\frac{E}{F_y}}$	$1.44\sqrt{\frac{E}{F_y}}$
21	Flange box sections	$1.12\sqrt{\frac{E}{F_y}}$	$1.13\sqrt{\frac{E}{F_y}}$	$1.65\sqrt{\frac{E}{F_y}}$	$1.49\sqrt{\frac{E}{F_y}}$	$1.44\sqrt{\frac{E}{F_y}}$
<b>Round</b>						
20	Round HSS/pipe	$0.07\sqrt{\frac{E}{F_y}}$	$0.06\sqrt{\frac{E}{F_y}}$	$0.08\sqrt{\frac{E}{F_y}}$	$0.31\sqrt{\frac{E}{F_y}}$	$0.11\sqrt{\frac{E}{F_y}}$

<sup>a</sup> AISC provisions are a function of web  $h/t_w$ , bounds provided here,  $F_L = 0.7F_y$ .

<sup>b</sup> Eurocode provisions provide limit as a function of whether unsupported tip is in compression or tension and specific to the plastic or elastic stress distribution on the unstiffened element. Typical ranges provided here.

<sup>c</sup> AISC provisions are a function of ENA to PNA distances, Eurocode provisions a function of PNA for Class 1 and Class 2, ENA for Class 3—i.e., stress gradient dependent, shading highlights substantial differences.



Table 3. Assumptions Underlying AISC 360 $w/t$ Limits— $\lambda_r$ Compression Elements in Members Subject to Axial Compression Only					
	Element Description	$k$	$\lambda^* = \sqrt{\frac{F_y}{F_{cr}}}$	Equation 10	AISC 360
Case	Unstiffened			$\lambda_r$	$\lambda_r$
1	Rolled flange	0.70 <sup>a</sup>	0.70 <sup>f</sup>	$0.56 \sqrt{\frac{E}{F_y}}$	$0.56 \sqrt{\frac{E}{F_y}}$
2	Built-up flange	0.35 ~ 0.76	0.70 <sup>f</sup>	0.39 to $0.58 \sqrt{\frac{E}{F_y}}$	0.38 to $0.56 \sqrt{\frac{E}{F_y}}$
3	Angle leg, other	0.425 <sup>b</sup>	0.70 <sup>f</sup>	$0.43 \sqrt{\frac{E}{F_y}}$	$0.45 \sqrt{\frac{E}{F_y}}$
4	Stem of tee	1.277 <sup>c</sup>	0.70 <sup>f</sup>	$0.75 \sqrt{\frac{E}{F_y}}$	$0.75 \sqrt{\frac{E}{F_y}}$
<b>Stiffened</b>					
5	Rolled web	5.0 <sup>d</sup>	0.70 <sup>f</sup>	$1.49 \sqrt{\frac{E}{F_y}}$	$1.49 \sqrt{\frac{E}{F_y}}$
6	HSS wall	4.4 <sup>e</sup>	0.70 <sup>f</sup>	$1.40 \sqrt{\frac{E}{F_y}}$	$1.40 \sqrt{\frac{E}{F_y}}$
7	Cover plate	4.4 <sup>e</sup>	0.70 <sup>f</sup>	$1.40 \sqrt{\frac{E}{F_y}}$	$1.40 \sqrt{\frac{E}{F_y}}$
8	Other	5.0 <sup>d</sup>	0.70 <sup>f</sup>	$1.49 \sqrt{\frac{E}{F_y}}$	$1.49 \sqrt{\frac{E}{F_y}}$
<sup>a</sup> Approximately halfway between pinned and fixed $k$ values. <sup>b</sup> Ideal case for simple-free longitudinal edge conditions. <sup>c</sup> Ideal case for fixed-free longitudinal edge condition. <sup>d</sup> Approximately one-third of the way between pinned and fixed $k$ values. <sup>e</sup> This $k$ factor back-calculated from $\lambda^*$ and the $w/t$ limit. <sup>f</sup> Nondimensional slenderness to achieve a plate strength approaching $F_y$ .					

the  $\lambda_r$  and  $\lambda_p$  limits in Table 4. Completion of this effort reveals some key assumptions embedded within the current AISC 360  $w/t$  limits. It is important to note, particularly for the  $\lambda_p$  limits, that the plastic strength limits are usually not derived on the basis of Equation 9 or similar; rather, they are determined experimentally. Here we are able to observe after the fact if simple unifying methods/assumptions still exist despite the largely experimental basis.

For all elements of compression members,  $\lambda_r^* = \sqrt{F_y/F_{cr}} = 0.7$ , implying  $F_{cr} \cong 2F_y$  is necessary for an element to reach its yield stress. This is predicated upon assumptions about the plate buckling coefficient,  $k$ , but is consistent across the  $w/t$  limits. AISC 360 assumes singular  $k$  values and ignores element interaction (in all but one case). Selected  $k$  values are generally between simply supported and fixed edge boundary conditions, except for stems of tees which use the maximum fully fixed edge condition

assumption. For flexural members, the assumptions are far more complicated, with many exceptions. In the following, sections, both  $\lambda_r$  and  $\lambda_p$  for flexure are discussed.

#### Further Examination of $\lambda_r$ Limits in Flexure

Overall, the plate buckling coefficient  $k$  values for  $\lambda_r$  in flexure (Table 4) follow the same logic as for compression members; however, providing definitive background reasoning for some cases is hard to finalize—for example, Case 10 for a rolled flange using  $k = 0.7$  and  $\lambda_r^* = 1.0$  still results in a more conservative  $w/t$  limit than specified in AISC 360, potentially due to  $F_L$  in past use ( $k = 1.1$  provides agreement with AISC 360). For  $\lambda_r$  in flexural members, Table 4 shows that AISC 360 generally employs  $\lambda_r^* = 1.0$ , implying  $F_{cr} = F_y$  is all that is necessary for an element to reach its target stress (i.e.,  $F_y$  or  $F_L$ ) at the extreme compression fiber. This is more liberal than  $\lambda_r^* = 0.7$  used for

**Table 4. Assumptions Underlying AISC 360  $w/t$  Limits— $\lambda_r$  and  $\lambda_p$   
Compression Elements in Members Subject to Flexure**

	Element Description	$k$	$\lambda_p^* = \sqrt{\frac{F_y}{F_{cr}}}$	Equation 10	AISC 360	$k$	$\lambda_r^* = \sqrt{\frac{F_y}{F_{cr}}}$	Equation 10	AISC 360
Case	Unstiffened			$\lambda_p$	$\lambda_p$			$\lambda_r$	$\lambda_r$
10	Rolled flange	0.7 <sup>a</sup>	0.464 <sup>h</sup>	$0.37 \sqrt{\frac{E}{F_y}}$	$0.38 \sqrt{\frac{E}{F_y}}$	0.7 <sup>a</sup>	1.0 <sup>m</sup>	$0.80 \sqrt{\frac{E}{F_y}}$	$1.00 \sqrt{\frac{E}{F_y}}$
11	Built-up flange	0.35 to 0.76 <sup>b</sup>	0.464 <sup>h</sup>	0.26 to $0.38 \sqrt{\frac{E}{F_y}}$	$0.38 \sqrt{\frac{E}{F_y}}$	0.35 to 0.76 <sup>b</sup>	1.0 <sup>n</sup>	$0.56 \text{ to } 0.83 \sqrt{\frac{E}{F_y}}$	$0.56 \text{ to } 0.83 \sqrt{\frac{E}{F_y}}$
12	Angle leg	0.90 <sup>c</sup>	0.464 <sup>h</sup>	$0.42 \sqrt{\frac{E}{F_y}}$	$0.54 \sqrt{\frac{E}{F_y}}$	0.90 <sup>c</sup>	1.0 <sup>m</sup>	$0.90 \sqrt{\frac{E}{F_y}}$	$0.91 \sqrt{\frac{E}{F_y}}$
13	Flange in minor axis	0.7 <sup>a</sup>	0.464 <sup>h</sup>	$0.37 \sqrt{\frac{E}{F_y}}$	$0.38 \sqrt{\frac{E}{F_y}}$	1.1 <sup>c</sup>	1.0 <sup>m</sup>	$1.00 \sqrt{\frac{E}{F_y}}$	$1.00 \sqrt{\frac{E}{F_y}}$
14	Stem of tee (flexure)	2.6 <sup>c</sup>	0.464 <sup>h</sup>	$0.71 \sqrt{\frac{E}{F_y}}$	$0.84 \sqrt{\frac{E}{F_y}}$	2.6 <sup>c</sup>	1.0 <sup>m</sup>	$1.53 \sqrt{\frac{E}{F_y}}$	$1.52 \sqrt{\frac{E}{F_y}}$
	<b>Stiffened</b>								
15	Web (doubly symmetrical)	36 <sup>d</sup>	0.56 <sup>i</sup>	$3.19 \sqrt{\frac{E}{F_y}}$	$3.76 \sqrt{\frac{E}{F_y}}$	36 <sup>k</sup>	1.0 <sup>o</sup>	$5.70 \sqrt{\frac{E}{F_y}}$	$5.70 \sqrt{\frac{E}{F_y}}$
19	Web of HSS and box	36 <sup>d</sup>	0.56 <sup>i</sup>	$3.19 \sqrt{\frac{E}{F_y}}$	$2.42 \sqrt{\frac{E}{F_y}}$	36 <sup>k</sup>	1.0 <sup>o</sup>	$5.70 \sqrt{\frac{E}{F_y}}$	$5.70 \sqrt{\frac{E}{F_y}}$
16	Web (singly symmetrical)	36 <sup>e</sup>	0.56 <sup>i</sup>	$3.19 \sqrt{\frac{E}{F_y}}$ <sup>j</sup>	$3.76 \sqrt{\frac{E}{F_y}}$ <sup>j</sup>	36 <sup>l</sup>	1.0 <sup>o</sup>	$5.70 \sqrt{\frac{E}{F_y}}$	$5.70 \sqrt{\frac{E}{F_y}}$
17	Flange of HSS	4.4 <sup>f</sup>	0.56 <sup>i</sup>	$1.12 \sqrt{\frac{E}{F_y}}$	$1.12 \sqrt{\frac{E}{F_y}}$	4.4 <sup>f</sup>	0.7 <sup>p</sup>	$1.40 \sqrt{\frac{E}{F_y}}$	$1.40 \sqrt{\frac{E}{F_y}}$
18	Flange cover plate	4.4 <sup>f</sup>	0.56 <sup>i</sup>	$1.12 \sqrt{\frac{E}{F_y}}$	$1.12 \sqrt{\frac{E}{F_y}}$	4.4 <sup>f</sup>	0.7 <sup>p</sup>	$1.40 \sqrt{\frac{E}{F_y}}$	$1.40 \sqrt{\frac{E}{F_y}}$
21	Flange of box	5.0 <sup>g</sup>	0.56 <sup>i</sup>	$1.19 \sqrt{\frac{E}{F_y}}$	$1.12 \sqrt{\frac{E}{F_y}}$	5.0 <sup>g</sup>	0.7 <sup>p</sup>	$1.49 \sqrt{\frac{E}{F_y}}$	$1.49 \sqrt{\frac{E}{F_y}}$

<sup>a</sup> Estimated as halfway between pinned and fixed  $k$  values.

<sup>b</sup> Factor at the limits of expression provided in AISC 360:  $k = 0.35 < 4\sqrt{h/t_w} < 0.76$ .

<sup>c</sup> Back-calculated from assumed flexure  $\lambda_r^* = 1.0$ .

<sup>d</sup> Based on elastic stress distribution, if plastic stress distribution used  $k_{\text{pinned}} = 10.3$ ,  $k_{\text{fixed}} = 15.4$ ,  $k_{90\%} = 14.4$  (also see note  $k$ ).

<sup>e</sup> Based on bending about symmetry axis, but  $k$  would be a function of ENA location in reality.

<sup>f</sup> Back-calculated from compression  $\lambda^*$  and  $w/t$  limit, same in flexure as compression.

<sup>g</sup> Estimated as one-third of the way between pinned and fixed  $k$  values for pure compression.

<sup>h</sup> 0.46 based on Haaijer and Thurlimann (1960) as onset of strain hardening in unstiffened element, also connects to continuous strength method (CSM) base curve by Gardner et al. (2019) and implies  $4\epsilon_y$  at this slenderness.

<sup>i</sup> 0.56 based on Haaijer and Thurlimann (1960) as onset of strain hardening in unstiffened element, also connects to CSM base curve by Gardner et al. (2019) and implies  $2\epsilon_y$  at this slenderness.

<sup>j</sup> Expression varies, value here for ENA = PNA and  $M_p/M_y = 1.12$  (typical rolled shape I); i.e., the symmetrical limit.

<sup>k</sup> Based on symmetrical bending, 80% of difference from  $k_{\text{pinned}} = 23.9$  and  $k_{\text{fixed}} = 39.6$  per Salmon et al. (2009).

<sup>l</sup> Based on bending about symmetry axis, but  $k$  would be a function of ENA in reality.

<sup>m</sup>  $F_{cr} = F_y$  assumed for  $\lambda_r^*$  because of agreement for Case 11 footnote  $n$ ; Cases 15, 16, and 19 footnote  $o$ ; and that even fully fixed values for  $k$  are not high enough to give AISC slenderness limits with  $\lambda_r^* = 0.7$  as was done in compression.

<sup>n</sup> Built-up flanges assumed to use  $F_{cr} = F_y$  for  $\lambda_r^*$ , also see footnote  $o$ .

<sup>o</sup> For flexure, AISC 360 assumes  $F_{cr} = F_y$  sufficient for extreme fiber of web to reach  $F_y$  (Salmon et al., 2009).

<sup>p</sup> For stiffened element flanges, AISC uses same normalized slenderness criteria as for compression members.

**Table 5. Application of  $\lambda_r$  Limits for Compression Elements in Members Subject to Flexure in AISC 360, Chapter F**

Section	Cross Section	Element	Limit State	$\lambda$	$M_r$	Equation Note	Table B4.1b Case
F3	I-doubly symmetrical	Unstiffened	FLB	$\lambda_{rf}$	$0.7M_y$	Explicit in Eq. F3-1	10
F4	I-singly symmetrical	Unstiffened	FLB	$\lambda_{rf}$	$0.7M_y$	Or lower per $S_{xt}/S_{xc}$	10, 11
F5	I	Unstiffened	FLB	$\lambda_{rf}$	$0.7M_y$	Explicit in Eq. F5-8	10, 11
F10	L	Unstiffened	LB	$\lambda_r$	$0.86M_y$	Implicit in Eq. F10-6	12
F6	I, C, minor	Unstiffened	FLB	$\lambda_{rf}$	$0.7M_y$	Explicit in Eq. F6-2	13
F9	Tee, 2L	Unstiffened	FLB	$\lambda_{rf}$	$0.7M_y$	Explicit in Eq. F9-14	10
F9	Tee, 2L	Unstiffened	LB flexure	$\lambda_r$	$0.65M_y$	Implicit in Eq. F9-18	14
F5	I	Stiffened	WLB	$\lambda_{rw}$	$M_y$	Implicit in $R_{pg}$ per Eq. F5-6	15, 16
F5	I	Stiffened	WLB-LTB	$\lambda_{rw}$	$M_y$	Implicit in $R_{pg}$ per Eq. F5-6	15, 16
F7	Box, HSS	Stiffened	FLB	$\lambda_{rf}$	$M_y$	Implicit in Eq. F7-2	17, 21
F7	Box, HSS	Stiffened	WLB	$\lambda_{rw}$	$M_y$	Implicit in Eq. F7-6	19
F7	Box, HSS	Stiffened	WLB-LTB	$\lambda_{rw}$	$M_y$	Implicit in $R_{pg}$ per Eq. F5-6	19

Note: Subscript *f* or *w* on  $\lambda_r$  refers to flange or web, respectively.

elements in compression members (implying  $F_{cr} \cong 2F_y$ ). AISC 360 extends this more liberal  $\lambda_r^* = 1.0$  to unstiffened element flanges that are part of a flexural member; but *does not* extend this more liberal  $\lambda_r^*$  to stiffened element flanges; these elements use the same  $\lambda_r^*$  as in compression. The use of the more liberal  $\lambda_r^* = 1.0$  appears to originate in past practice for plate girder design. Note that other studied specifications—Eurocode, AISI S100, and AIJ—do not make this assumption, leading to fairly stark differences between slender element  $w/t$  limits of flexural members.

Hidden in these comparisons are the past use of  $F_L$ , which liberalizes the  $w/t$  limit, and whether or not the limit is intended to achieve an  $M_r$  of  $M_y$  or  $0.7M_y$ . A review of the application of  $\lambda_r$  in AISC 360, Chapter F, is provided in Table 5. The  $\lambda_r$  for unstiffened elements provides an  $M_r$  of  $0.7M_y$ , while for stiffened elements in flexure,  $\lambda_r$  intends to establish an  $M_r$  of  $M_y$ . As detailed in Table 5, the connection is explicit for some cases, while in other cases, substitution of appropriate  $\lambda_r$  values must be completed to determine the strength that  $\lambda = \lambda_r$  implies.

The use of  $\lambda_r$  for flanges must be understood in the context of the strength predictions of AISC 360, Chapter F. For the prototypical flange local buckling (FLB) case, Figure 2 illustrates the solution. It can be observed that  $\lambda_r$  is an anchor point in the strength prediction and is typically tied to  $M_r = 0.7M_y$ . While it is true that AISC 360 transitions to the plate elastic buckling curve for  $\lambda > \lambda_r$ , actual behavior does not have a sharp inelastic/elastic transition. Thus,  $\lambda_r$  is not at a definitive transition to elastic stress, but rather is an anchor point in a strength curve deemed to provide reasonable cross-section flexural strength prediction.

Note that Eurocode and AISI S100 follow Winter’s equation (Winter, 1947) anchored to  $M_y$  instead of  $0.7M_y$ , and include post-buckling. Thus, the particulars of the strength curves selected in AISC 360, Chapter F (particularly  $M_r$ ) end up influencing the consistency of the  $\lambda_r$  limits in Chapter B.

The use of  $\lambda_r$  for webs in Chapter F is primarily handled through the  $R_{pg}$  reduction factor. Note that the connection between web slenderness limits and bending strength is particularly indirect and strongly dependent on the flange because the flange contributes much more to cross-section moment of inertia,  $I$ , and plastic section modulus,  $Z$ , than the web. Thus, a large error in a web slenderness limit may have only a small impact on the flexural strength prediction of many common sections. Nonetheless, the use of  $\lambda_r^* = 1.0$  for the  $M_r = M_y$  cases (15, 16, and 19) is difficult to justify based on plate mechanics arguments.

**Further Examination of  $\lambda_p$  Limits in Flexure**

The origin of the flexural compactness limit  $\lambda_p$  may be primarily understood as being derived from limits on the nondimensional slenderness  $\lambda_p^*$ . Historically, this has been based on mechanical approximations, setting  $\lambda_p^* \cong 0.46$  for unstiffened elements and  $\lambda_p^* \cong 0.58$  for stiffened elements (Haaijer and Thurlimann, 1960). Today, based on the work of Gardner and colleagues (e.g., Afshan and Gardner, 2013; Zhao et al., 2017), this could be characterized as providing  $4\epsilon_y$  for unstiffened elements and  $2\epsilon_y$  for stiffened elements. Unstiffened element  $\lambda_p$  generally follows  $\lambda_p^* \cong 0.46$ ; however, Case 12 (legs of single angles in Table 4) has a more relaxed  $\lambda_p$  limit than Case 10 (flanges of rolled shapes).

Because Case 12 includes the possibility of the angle leg bent about a geometric axis that places the entire element in compression (essentially the same as Case 10), the origin of the difference is not entirely clear. A possible reason is the application of upper bounds on  $M_p$  in AISC 360. For example, for an angle section,  $M_p$  is limited to  $1.5M_y$ , even though the typical shape factor is 1.8; therefore, the  $\lambda_p$  required to reach  $1.5M_y$  may be more relaxed than that to reach  $M_p$ .

Stiffened element  $\lambda_p$ , when the element is in compression, is generally consistent with the overall practice regarding a limiting  $\lambda_p^* \cong 0.56$ ; this is true even for HSS where the limit was derived experimentally on full sections without direct consideration of the underlying assumptions (Wilkinson and Hancock, 1998). Stiffened element  $\lambda_p$ , when the element is in flexure, does not agree particularly well with the overall assumption of slenderness  $\lambda_p^* \cong 0.56$ . Further, if the  $k$  is based on the plastic, not the elastic, stress distribution,  $k$  would be considerably lower, leading to an even larger disagreement between assumed and actual  $\lambda_p$  in AISC 360 for stiffened elements in flexure.

### Discussion of Local Buckling Web-Flange Interaction

Web-flange interaction is shorthand for the phenomenon that the isolated plate solutions that are typically used to predict local buckling are not actually isolated but, instead, interact. Equilibrium and compatibility are, of course, maintained between elements in a cross section when undergoing elastic or inelastic local buckling. In this regard, the separation into flange local buckling (FLB) and web local buckling (WLB) is artificial—the web and flange of cross sections always interact. The primary question is this: To what extent does this interaction matter? The traditional

conclusion, for rolled shapes at yield stresses consistent with mild steel, is that the interaction is either weak or otherwise does not vary much and can be approximated for standard (rolled) shapes by treating FLB and WLB as essentially constant and separate plate phenomena. This assumption is largely embedded in the  $w/t$  limits in AISC 360.

For nonseismic  $w/t$  limits, the one case where web-flange interaction is explicitly considered in AISC 360 is in the  $w/t$  limits for flanges of built-up I-shapes. For this case,  $k$  is calculated with the assumption:

$$k = 0.35 < \frac{4}{\sqrt{h/t_w}} < 0.76 \quad (10)$$

Equation 10 is a simplification of the expression provided by Johnson (1976), where  $k$  was approximated from testing employing the basic mechanics outlined in Haaijjer and Thurlimann (1960). Notably, this  $k$  is not a plate buckling coefficient in the traditional sense and does not agree well with elastic theory. A comparison was made employing the expressions in Seif and Schafer (2010), and Equation 10 is higher than the elastic solution. However, White (2008) found that the expression, albeit a simplification, works generally well with available data from a strength perspective.

Web-flange interaction is implicitly considered for other elements in the AISC  $w/t$  limits, but at assumed levels of rigidity as detailed in the footnotes to Table 3 and Table 4. For example, the  $k$  for an I-section flange in a compression member is assumed to be 0.7, which is halfway between the rigidity limits of a simply supported and a fixed longitudinal edge. This sounds rational, but when compared to the actual elastic  $k$  based on thin-plate theory and including web-flange interaction for I-sections [Figure 3(b)] in compression, this  $k$  is quite optimistic (Seif and Schafer, 2010).

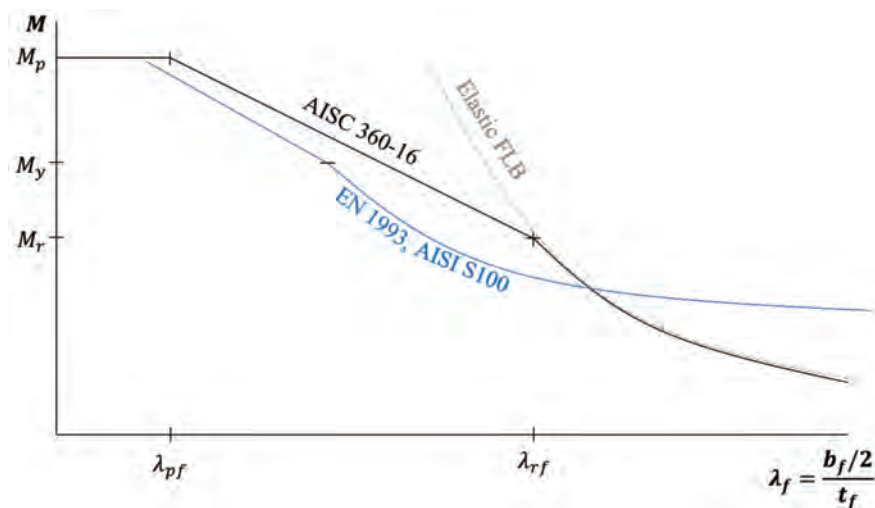


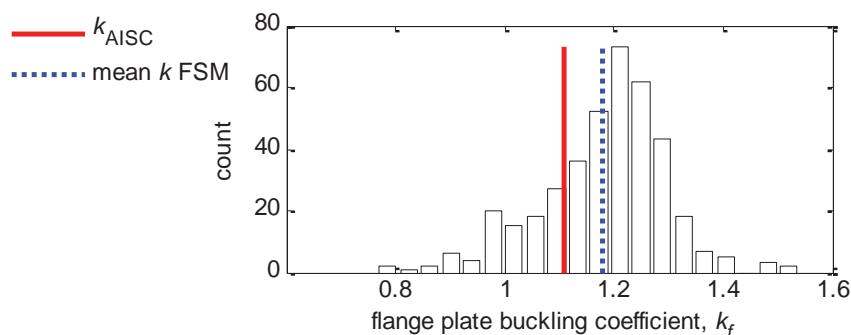
Fig. 2. Typical application of  $\lambda_r$  in flange local buckling for AISC 360 compared with other standards.

The compressive stress on the web degrades the flange plate buckling coefficient,  $k$ . This is not uncommon because it is not just the rigidity, but also the stress on the attached elements that influences the local cross-section stability. In flexure, the web stability is significantly enhanced from the compression case, and the mean flange  $k$  for I-sections is as high as 1.2 [Figure 3(a)] and compares favorably with the back-calculated  $k$  from AISC’s flexural  $\lambda_r$  limit. The footnotes of Table 3 and Table 4 specifically address the  $k$  value and their implicit assumptions about web-flange interaction for all  $w/t$  cases; comparisons are provided for nearly all cases in Seif and Schafer (2010). It is recommended in Seif and Schafer that mean  $k$  values (determined from elastic buckling of all relevant rolled shapes) or values based on a given exceedance probability be selected so as to provide uniformity across elements even if a single  $k$  is selected. This is a reasonable suggestion, but it would lead to changes in almost all  $\lambda_r$  limits in AISC 360. Alternatives are explored later in this paper.

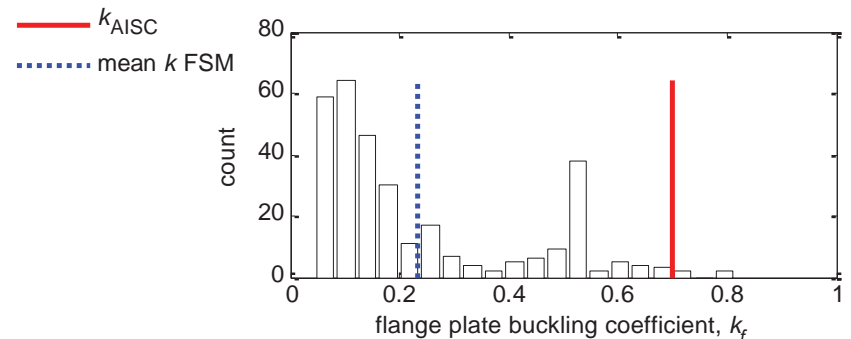
The dependency of the plate buckling coefficient on the applied stress leads to another important consideration in web-flange interaction: how to handle  $w/t$  limits for beam-columns. Earlier editions of the AISC *Specification*—for

example, the first edition of the AISC LRFD *Specification* (1986)—included  $w/t$  limits for “webs in combined flexure and axial compression” that were a function of the stress gradient captured through the ratio of  $P_r/P_y$ , where  $P_r$  is the required axial strength and  $P_y$  is the squash load. These provisions were later simplified using the compression  $w/t$  limit throughout; however, AISC 341 has maintained a dependence on the compression load that has seen recent study as discussed in Section 4.3. See Schafer et al. (2020) for additional discussion on implementing stress-dependent  $w/t$  limits for beam-columns in AISC 360.

Analytical expressions, derived from simulations, are available to provide closed-formed solutions for accurate plate buckling coefficients,  $k$ , or, more directly, the cross-section local buckling load,  $P_{crt}$ , or moment,  $M_{crt}$ . Seif and Schafer (2010) provide one set of solutions, and Fieber et al. (2019) have recently derived another set. In addition, efficient and simple computational programs exist for calculating cross-section local buckling [see Appendix 2 of AISI S100 (2016) for extensive commentary, including links to software] and all buckling values for common shapes could be tabulated in much the same way as complex section properties such as  $C_w$  are tabulated for use in design.



(a)  $k$  for flange (flange in compression, web in flexure)



(b)  $k$  for flange (flange in compression, web in compression)

Fig. 3. Excerpt from Seif and Schafer (2010). Example of flange buckling  $k_f$  for all I-sections in AISC Manual (a) flexure and (b) compression compared with  $k$  assumed in  $w/t$  development.

## AISC 341 LOCAL BUCKLING LIMITS FOR SEISMIC DESIGN

Since their introduction in 1990 in the AISC *Seismic Provisions* (AISC, 1990), the local buckling (i.e.,  $w/t$ ) requirements have undergone regular revision. The seismic  $w/t$  limits are part of the ductility design requirements to ensure adequate inelastic deformation capacities. The requirements in the 1990 edition of the *Seismic Provisions* were basically those from the 1988 Uniform Building Code (ICBO, 1988), which were based on limited research conducted in the 1970s and 1980s. The seismic local buckling requirements were also strongly influenced by the plastic design provisions in the AISC *Specification*.

The Northridge Earthquake in 1994 triggered a new wave of seismic steel research activities, not only for special moment frames (SMFs) but also for other types of seismic force-resisting systems (SFRSs). AISC 341, Table D1.1, provides the limiting  $w/t$  ratios for all SFRS covered in AISC 341 (see Table 6). Starting with the 2010 edition of AISC 341, this table expresses local buckling requirements in the form of  $\lambda_{hd}$  values for highly ductile members and  $\lambda_{md}$  values for moderately ductile members in lieu of the previously used terms: seismically compact and compact. This change in terminology was made because the limiting  $w/t$  ratios did not always reflect limit states consistent with the AISC 360 use of “compact.” Up until 2010, the limiting  $\lambda$  values were written as a function of  $E$  and  $F_y$ , but starting in 2016, these formulae were converted to a new format by replacing the nominal yield stress,  $F_y$ , by the expected yield stress,  $R_y F_y$ , and changing the coefficients under assumed  $R_y$  values as discussed in Section 4.2.

### Objectives

Local buckling,  $w/t$ , limits in AISC 341 serve multiple objectives, and their application is typically dependent on the SFRS. AISC 341, Table D1.1, provides two limits: moderately ductile  $\lambda_{md}$  and highly ductile  $\lambda_{hd}$ ; however, the limits are not only a function of the type of element in a section (e.g., stiffened vs. unstiffened), but also a function of how the section is employed in the SFRS. For example, a diagonal brace in a special concentrically braced frame (SCBF) and in an eccentrically braced frame (EBF) are treated differently, as is a beam in a SMF versus in a buckling-restrained braced frame (BRBF). Focusing on I-shaped beams in intermediate moment frames (IMFs) and SMFs as the prototypical application of local buckling  $w/t$  limits, the AISC 341 Commentary provides the basic objectives:  $\lambda_{md}$  provides a section that can undergo plastic rotation of 0.02 rad or less, and  $\lambda_{hd}$  provides a section that can undergo plastic rotation of 0.04 rad or more. The Commentary further states that  $\lambda_{md}$  in AISC 341 is generally the same as  $\lambda_p$  in AISC 360, with the exception of HSS, stems of WTs, and

webs in flexure. Further,  $\lambda_{hd}$  is typically stricter than  $\lambda_p$ , though in several cases this is relaxed. A summary of all current  $w/t$  limits for AISC 360 and AISC 341 is provided in Table 6.

To fully understand the objective in the application of the  $\lambda_{md}$  and  $\lambda_{hd}$  limits, one must go through each SFRS. A summary of the application of these limits and their intended objective is provided in Table 7 and complete details are provided in Schafer et al. (2020). In general, the following observations can be made regarding the objectives of  $\lambda_{md}$  and  $\lambda_{hd}$ :

- $\lambda_{md}$ : Provide enough ductility so that the SFRS can develop its system strength,  $R_r$ , and last several cycles at that strength ( $n$  cycles); provide sufficient compactness so that a member can develop  $M_p$  or, in some cases,  $M_p$  and at least 0.02 rad, or  $M_p$  up to and including strain hardening,  $M_{pe}$ . Application of these objectives is system dependent.
- $\lambda_{hd}$ : Provide enough ductility so that the SFRS can develop its system strength,  $R_r$ , and last several system cycles at that strength ( $n$  cycles) or system interstory drift (3% ID); provide sufficient compactness so that a member can develop  $M_p$  or, in some cases,  $M_p$  and at least 0.04 rad rotation (i.e., story drift angle) at a post-peak of  $0.8M_p$ , or  $M_p$  up to and including strain hardening,  $M_{pe}$ , or high component level strains (10–20 $\epsilon_y$ ) and high numbers of component cycles ( $n$  cycles). Application of these objectives is system dependent.

When a concern exists regarding seismic behavior of a member, but limited research or knowledge is available, it is common to require  $\lambda_{md}$  or  $\lambda_{hd}$  even if it is not strictly needed for strength. As a result, the objectives for these criteria are sometimes clear and discrete, but more often manifold and complex.

### Expected Material Properties and $w/t$ Limits

The use of  $R_y F_y$  in AISC 341 and  $F_y$  in AISC 360 for the  $w/t$  limits creates a discrepancy for the user that requires attention and explanation. If it is important to use the best estimate of the mean  $F_y$  in seismic design,  $R_y F_y$ , why not do so in nonseismic design? Also, has the introduction of  $R_y F_y$  in AISC 341 met the desired intent when applied?

The AISC task group considered if the increased yield strength modifier,  $R_y$ , that is used in AISC 341 should also be included in AISC 360. The actual  $F_y$  is, on average, greater than the nominal  $F_y$  used in design. This opens the possibility that a compact section based on the nominal  $F_y$  may actually be a noncompact section because the  $\lambda$  based on the actual  $F_y$  may be less than  $\lambda_p$  based on the nominal  $F_y$ . The counterargument is that the design strength based on  $F_y$  will be conservatively less than that based on  $R_y F_y$ ,

**Table 6. Comparison of AISC 360 and AISC 341 w/t Limits**

AISC 360 Table B4.1a Compression Elements in Members Subject to Compression Only				AISC 341 Table D1.1		
Case	Element Description	$\lambda_r$	$\lambda_p$	Note	$\lambda_{md}$	$\lambda_{nd}$
1	Rolled I-flanges	$0.56\sqrt{E/F_y}$	—		$0.40\sqrt{E/(R_yF_y)}$	$0.32\sqrt{E/(R_yF_y)}$
2	Built-up I-flanges	$0.64\sqrt{E/F_y}$	—		$0.40\sqrt{E/(R_yF_y)}$	$0.32\sqrt{E/(R_yF_y)}$
3	Angle legs	$0.45\sqrt{E/F_y}$	—		$0.40\sqrt{E/(R_yF_y)}$	$0.32\sqrt{E/(R_yF_y)}$
4	Tee stems	$0.75\sqrt{E/F_y}$	—		$0.40\sqrt{E/(R_yF_y)}$	$0.32\sqrt{E/(R_yF_y)}$
5	I-webs	$1.49\sqrt{E/F_y}$	—	Braces	$1.57\sqrt{E/(R_yF_y)}$	$1.57\sqrt{E/(R_yF_y)}$
6	HSS walls	$1.40\sqrt{E/F_y}$	—	Braces	$0.76\sqrt{E/(R_yF_y)}$	$0.65\sqrt{E/(R_yF_y)}$
			—	Columns	$1.18\sqrt{E/(R_yF_y)}$	$0.65\sqrt{E/(R_yF_y)}$
7	Cover plates	$1.40\sqrt{E/F_y}$	—		—	—
8	Stiffened element	$1.49\sqrt{E/F_y}$	—		—	—
9	Round HSS	$0.11 E/F_y$	—		$0.062 E/(R_yF_y)$	$0.053 E/(R_yF_y)$
	Flanges of H-piles	—	—		$0.48\sqrt{E/(R_yF_y)}^a$	n.a. <sup>a</sup>
	Webs of H-piles	—	—		$1.57\sqrt{E/(R_yF_y)}^a$	n.a. <sup>a</sup>
AISC 360 Table B4.1b Compression Elements in Members Subject to Flexure						
10	Rolled I-flanges	$1.00\sqrt{E/F_y}$	$0.38\sqrt{E/F_y}$		$0.40\sqrt{E/(R_yF_y)}$	$0.32\sqrt{E/(R_yF_y)}$
11	Built-up I-flanges	$0.95\sqrt{E/F_y}$	$0.38\sqrt{E/F_y}$		$0.40\sqrt{E/(R_yF_y)}$	$0.32\sqrt{E/(R_yF_y)}$
12	Angle legs	$0.91\sqrt{E/F_y}$	$0.54\sqrt{E/F_y}$		$0.40\sqrt{E/(R_yF_y)}$	$0.32\sqrt{E/(R_yF_y)}$
13	Minor axis I-flanges	$1.00\sqrt{E/F_y}$	$0.38\sqrt{E/F_y}$		—	—
14	Tee stems	$1.52\sqrt{E/F_y}$	$0.84\sqrt{E/F_y}$		$0.40\sqrt{E/(R_yF_y)}$	$0.32\sqrt{E/(R_yF_y)}$
15	I-webs	$5.70\sqrt{E/F_y}$	$3.76\sqrt{E/F_y}$		$f(P_u/P_y)$	$f(P_u/P_y)$
16	Singly symmetrical I-webs	$5.70\sqrt{E/F_y}$	$f(h_c/h_p)$		—	—
17	HSS flanges	$1.40\sqrt{E/F_y}$	$1.12\sqrt{E/F_y}$		$1.18\sqrt{E/(R_yF_y)}$	$0.65\sqrt{E/(R_yF_y)}$
18	Flange cover plates	$1.40\sqrt{E/F_y}$	$1.12\sqrt{E/F_y}$		—	—
19	HSS webs	$5.70\sqrt{E/F_y}$	$2.42\sqrt{E/F_y}$		—	—
	Box webs				$1.75\sqrt{E/(R_yF_y)}$	$0.67\sqrt{E/(R_yF_y)}$
20	Round HSS	$0.31E/F_y$	$0.07E/F_y$		$0.062E/(R_yF_y)$	$0.053E/(R_yF_y)$
21	Box flanges	$1.49\sqrt{E/F_y}$	$1.12\sqrt{E/F_y}$		$1.18\sqrt{E/(R_yF_y)}$	$0.65\sqrt{E/(R_yF_y)}$

<sup>a</sup> Potentially better categorized as flexure case in AISC 341.  
 — Denotes not applicable.

Table 7. Summary of Intended Objectives for Application of $\lambda$ Limits in AISC 341-16			
	System*	Element	Objective
$\lambda_{md}$	IMF	Beam	$M_p$ , 0.02 rad ID
		Column	$R_r$
	OCBF	Brace	$R_r$ , $n$ cycles
	MT-SCBF	Strut	$M_{pe}$
	EBF	Beam outside link	$R_r$
		Brace	$R_r$
	BRBF	Beam	$R_r$
		Column	$R_r$
$\lambda_{hd}$	SMF	Beam	$M_p$ , 0.04 rad ID @ $0.8M_p$
		Column	$M_p$ , $R_r$ , 0.04 rad
	STMF	Chord and diagonal	3% ID
		Column	3% ID
	SCCS	Column	$M_p$ , limit FLB, large $\theta_p$
	SCBF	Beam	$R_r$
		Column	$R_r$ , large $\theta_p$
		Brace	$R_r$ , $n$ cycles, yield @ 0.3%ID, 10–20 $\epsilon_y$
	MT-SCBF	Column	$M_{pe}$
		Brace	$R_r$ , $n$ cycles, yield @ 0.3%ID, 10–20 $\epsilon_y$
	EBF	Link	0.02–0.08 rad inelastic rotation
		Column	$R_r$
MT-BRBF	Beam	$R_r$	
	Column	$R_r$	
SPSW	Column boundary	$R_r$	
	Horizontal boundary	$M_p$ , $n$ cycles	

Note:  $R_r$  = required system strength based on capacity design, ID = interstory drift, FLB = flange local buckling.  
\* See AISC 341 for SFRS abbreviations.

even if the member is no longer compact. This counter argument was found to prevail for all practical cases studied (Schafer et al., 2020). For the structures, loadings, and margin of safety in AISC 360, large overloads are not expected, and the actual mode of failure is not important. This is not true for AISC 341, where structures undergo extreme conditions. In this case, the failure mode could potentially cause the energy-absorbing location to shift from the intended location to an undesirable location, resulting in nonductile failure modes. Therefore, while it is not recommended that  $R_y$  be included in AISC 360, it is appropriate to include  $R_y$  in AISC 341.

Use of  $R_y F_y$  in the  $w/t$  limits for AISC 341 provides a more accurate prediction of the desired behavior; further, it removes the perverse incentive of specifying a lower  $F_y$ , even when expected  $F_y$  is high, only so that a compactness

limit or other limit related to energy dissipation can be met. However, the implementation of the  $R_y$  factor in the existing  $w/t$  limits requires discussion. AISC 341 introduced  $R_y$  into its  $w/t$  limits in the 2016 edition for the first time, but in such a manner as to not actually change the limiting values for typical steels. For example,  $\lambda_{md} = 0.38\sqrt{E/F_y}$  for flanges of I-shaped sections in AISC 341-10 was converted to  $0.40\sqrt{E/(R_y F_y)}$  in AISC 341-16 by assuming  $R_y = 1.1$  for A992-type steel. Similarly, for walls of rectangular HSS used as diagonal braces  $\lambda_{hd} = 0.55\sqrt{E/F_y}$  for flanges of I-shaped sections in AISC 341-10 was converted to  $0.65\sqrt{E/(R_y F_y)}$  in AISC 341-16 by assuming  $R_y = 1.14$  for A500 Grade B steel.

For the former example, the original experimental source for the  $\lambda_p$  limit (Lukey and Adams, 1969), which



$\lambda_{md}$  is based on, was experimentally developed based on measured  $F_y$  but then applied in AISC 360, and later in AISC 341, as nominal/specified  $F_y$ . In general, researchers develop  $w/t$  limits with measured  $F_y$  properties and code committees then implement them with specified properties. If the change in 2016 for AISC 341 was intended to bring the  $w/t$  limit in line with the original testing, then the coefficient should not have been modified and only  $R_y$  added to the denominator. The task group recommended that course of action and it is expected in the forthcoming 2022 edition of AISC 360. Schafer et al. (2020) provides additional discussion on  $R_y$  and the impact of other material properties (strain hardening slope, etc.) and higher strength steels on the  $w/t$  limits.

### Web-Flange Interaction and Impact on Seismic $w/t$ Limits (Deep Columns)

Deep wide-flange columns have seen increasing use in the SFRSs of buildings, particularly in moment frames due to their relative effectiveness for story drift control. Columns in an SMF are expected to experience flexural yielding and form a plastic hinge at the column base. Deep columns have  $h/t_w$  ratios that often are significantly higher than those of shallow columns (e.g., W12 or W14). Recent testing of  $\lambda_{hd}$ -compliant deep columns at the University of California–San Diego (UCSD) has shown that the web in these columns was not effective in stabilizing the flanges under cyclic loading (Ozkula and Uang, 2015; Chansuk et al., 2018). Interactive web-flange local buckling occurs prematurely and causes significant strength degradation and axial shortening. Under cyclic loading, lateral-torsional buckling, together with local buckling, can also occur. Figure 4 illustrates two typical stability driven failures observed in the testing. Independent research conducted by Elkady and Lignos (2018) and Wu et al. (2018) have also confirmed this problematic phenomenon in deep columns for moment frames.

To resolve this issue, new  $\lambda_{hd}$  and  $\lambda_{md}$  limits have been

proposed for AISC 341 to be used in beams, columns, or links as webs in flexure, or as combined axial and flexure, including webs of rolled or built-up I-shaped sections or channels, side plates of boxed I-shaped sections, and webs of built-up box sections as provided in Table 8. The new limits are based on regression analysis of deep column responses from both testing and finite element simulation and consider the effects of boundary condition and lateral loading sequence on local and lateral-torsional buckling (Ozkula et al., 2021). The limiting  $h/t_w$  ratios are developed for constant axial loads. For exterior columns with varying axial loads due to the overturning moment effect, the proposed limits are conservative.

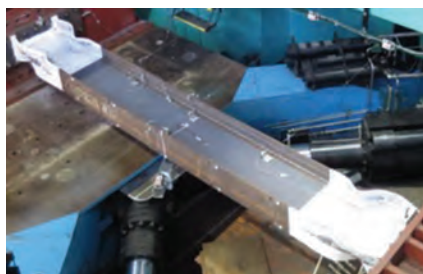
### ALTERNATIVES TO LOCAL BUCKLING ( $w/t$ ) LIMITS

The task group was also charged with commenting on alternative means of establishing basic local buckling performance objectives and ensuring the specification provides user pathways to these alternative means when current  $w/t$  limits may be an impediment—for example, for higher strength steels, steels with nontraditional stress-strain relations (e.g., no yield plateau like stainless steel), unusual built-up cross sections, etc.

### Cross-Section Local Slenderness Limits and Application of DSM

The direct strength method (DSM) (Schafer, 2019) as implemented in AISI S100 provides limits that are similar in spirit to the AISC  $w/t$  limits, but for the entire cross section, where  $P_{cr\ell}$  is the elastic axial local buckling force and  $M_{cr\ell}$  is the elastic flexural local buckling moment. Cross-section elastic local buckling may be determined by analytical formulas for common shapes (e.g., Gardner et al., 2019; Seif and Schafer, 2010) or numerical analyses for more complex configurations as detailed in the AISI S100 Commentary.

$$P_n = P_y \quad \text{if} \quad \lambda_\ell^* = \sqrt{\frac{P_y}{P_{cr\ell}}} = 0.776 \quad (11)$$



(a) W24x131 column



(b) W24x176 column

Fig. 4. Typical deep column buckling mode.

Table 8. Proposed Change in Web $w/t$ in AISC 341		
	$\lambda_{hd}$ for Highly Ductile Members	$\lambda_{md}$ for Moderately Ductile Members
AISC 341-16	For $C_a \leq 0.114$ : $2.57 \sqrt{\frac{E}{R_y F_y}} (1 - 1.04 C_a)$ For $C_a > 0.114$ : $0.88 \sqrt{\frac{E}{R_y F_y}} (2.68 - C_a) \geq 1.57 \sqrt{\frac{E}{R_y F_y}}$	For $C_a \leq 0.114$ : $3.96 \sqrt{\frac{E}{R_y F_y}} (1 - 3.04 C_a)$ For $C_a > 0.114$ : $1.29 \sqrt{\frac{E}{R_y F_y}} (2.12 - C_a) \geq 1.57 \sqrt{\frac{E}{R_y F_y}}$
Proposed for AISC 341-22	$2.5(1 - C_a)^{2.3} \sqrt{\frac{E}{R_y F_y}}$	$5.4(1 - C_a)^{2.3} \sqrt{\frac{E}{R_y F_y}}$
Note: $C_a = \frac{\alpha_s P_r}{R_y F_y A_g}$ and $P_r$ is the required axial strength, $\alpha_s$ is the ASD/LRFD conversion factor, and $A_g$ is the gross area of the column; all other terms previously defined.		

$$M_n = M_y \text{ if } \lambda_\ell^* = \sqrt{\frac{M_y}{M_{cr\ell}}} = 0.776 \quad (12)$$

$$M_n \equiv M_p \text{ if } \lambda_\ell^* = \sqrt{\frac{M_y}{M_{cr\ell}}} = 0.086 \quad (13)$$

Equations 11 and 12 provide the equivalent to the  $\lambda_r$  limit and Equation 13 the  $\lambda_p$  limit. Equation 13 is intentionally conservative in its application for AISI S100 and would need modification for AISC 360 application.

### Cross-Section Local Slenderness Limits and Application of CSM

The continuous strength method (CSM) developed by Gardner et al. (e.g., Afshan and Gardner, 2013; Zhao et al., 2017) provides a complete strain-based alternative to local buckling classification limits, but it could equally be used to provide basic limits. The CSM base curve implies the maximum strain capacity is a function of the local buckling slenderness, focusing on the range where  $\varepsilon \geq \varepsilon_y$ :

$$\varepsilon = \frac{0.25}{\lambda_\ell^{*3.6}}, \quad \lambda_\ell^* = \sqrt{\frac{P_y}{P_{cr\ell}}} \text{ or } \sqrt{\frac{M_y}{M_{cr\ell}}} \quad (14)$$

If we set  $\varepsilon = \varepsilon_y$  for the equivalent to the  $\lambda_r$  limit, and set  $\varepsilon = 4\varepsilon_y$  for the  $\lambda_p$  limit:

$$P_n = P_y \text{ if } \lambda_\ell^* = \sqrt{\frac{P_y}{P_{cr\ell}}} = 0.68 \quad (15)$$

$$M_n = M_y \text{ if } \lambda_\ell^* = \sqrt{\frac{M_y}{M_{cr\ell}}} = 0.68 \quad (16)$$

$$M_n \equiv M_p \text{ if } \lambda_\ell^* = \sqrt{\frac{M_y}{M_{cr\ell}}} = 0.46 \quad (17)$$

Note  $\varepsilon = 15\varepsilon_y$  for the  $\lambda_{hd}$  limit would result in  $\lambda_\ell^* = 0.32$ . Given the approximate nature of current element slenderness limits, it should be permitted to use more robust cross-section-based slenderness limits when desired by the engineer. Note that for some sections under some loading conditions, these limits will be more stringent than current practice and for others more lenient. In general, the large class of  $w/t$  limits (Table B4.1 in AISC 360 and Table D1.1 in AISC 341) could be replaced with these simple cross-section-based criteria.

An additional note on Equation 14: The power of this expression should not be understated. Recall Equation 6 where the elastic plate buckling strain was made independent of Young's modulus; so too is Equation 14 and, in fact, has been developed considering stainless steel, aluminum, and traditional mild carbon steels. Further, the limits in Equations 15–17 agree quite well with Winter's (1947) insights and Haijjer and Thurlimann's (1960) insights on key slenderness ranges for first yield and plastic behavior. This generalization is attractive, and a means to leverage this insight is worthy of consideration for AISC *Specifications*.

### Extensions on the Use of CSM and DSM

Both CSM and DSM can do more than provide the local buckling limits; they can be used to predict the actual cross-section strength. CSM's strain-based approach is particularly powerful if nonlinearity in the material stress-strain curve is such that the elastic-plastic assumption is not adequate (as is the case with some new high-strength steel grades). Both CSM and DSM have been developed and are being adopted for forthcoming editions of stainless steel standards (ASCE, 2021; AISC, 2021).

In addition, Torabian and Schafer (2014) used a CSM-inspired approach to establish rotation capacity in addition

to strength. Thus, it is possible to provide a methodology for predicting allowable rotation capacity,  $R_{cap}$ , for use in material nonlinear analyses, both static for AISC 360 and potentially dynamic for application to AISC 341. This could potentially be advanced in AISC 360, Appendix 1. Recent work of Gardner et al. (2019) has extended these insights directly into line elements for use in system analysis.

## DISCUSSION AND RECOMMENDATIONS

The current  $w/t$  formulation—for example, Equation 4—for local buckling limits in AISC 360 and AISC 341 has several strengths: The method (1) is easy and fast to apply, (2) has a long tradition of use, (3) has a relatively high level of clarity, and (4) leads to reliable strength predictions. Weaknesses of the existing  $w/t$  formulation include the following: (1) The method connects to the element, not the section, and most behavior objectives are at the section level; (2) for the limits to be simple, constant coefficients for  $C$  (Equation 4) are commonly used; however, if web-flange interaction (i.e., simple equilibrium and compatibility within the section), stress distribution (e.g., stresses from a beam-column, difference in stresses when a flange tip is in tension/compression), or material nonlinearity is considered, this breaks down, and determination of  $C$  becomes its own quite complex process; and (3) by using  $w/t$  instead of the nondimensional slenderness,  $\lambda^*$  (i.e.,  $\sqrt{F_y/F_{cr}}$ ), the limits appear to be different for every element (i.e., lots of different  $C$  values), while in reality, only one assumption ( $\lambda^*$ ) is typically being made—this reduces conceptual clarity. In addition, when one delves into the details, such as Table 3 and Table 4, numerous small inconsistencies emerge. Comparing the level of detail required to understand current provisions with the alternative local buckling criteria discussed earlier, it is evident that clearer, more robust, and more direct methods are now available based on cross-section local buckling instead of element local buckling to achieve the same objectives as current methods.

The task group came to the following recommendations:

### Nonseismic AISC 360 Recommendations

Rewrite the AISC 360, Table B4.1 Commentary. Provide objectives using the *Objective of AISC 360 Local Buckling Limits* section of this paper (aligned with the *Specification*, not aspirational). Make the role of nondimensional slenderness,  $\lambda^*$ , clear, and provide finalized versions of Tables 3 and 4 in the AISC 360 Commentary or through reference to an archival publication.

Provide an alternative pathway for the use of cross-section elastic buckling analysis that includes web-flange interaction as an alternative to current  $w/t$  limits. Set  $\lambda_r^* = 0.7$  or 1.0 as appropriate and  $\lambda_p^* = 0.5$  for these alternative provisions. Current  $\lambda_r$  for flexure limits should be recast to make

it explicitly clear why  $\lambda_r^* = 1.0$  not  $\lambda_r^* = 0.7$  is used. This would explain the discrepancy in Table B4.1b between (1) stiffened elements in compression and (2) unstiffened elements in compression and stiffened elements in flexure and explain the discrepancy between compression elements in Table B4.1a and b. This would also explain a significant discrepancy between current AISC practice and other international standards. Assuming independent research is not conducted, then it is recommended that  $\lambda_r^* = 0.7$  be used throughout and AISC 360, Chapter F, modified to accommodate this change. This would remove the discrepancy in Table B4.1b between (1) stiffened elements in compression and (2) unstiffened elements in compression and stiffened elements in flexure and would remove the discrepancy between compression elements in Table B4.1a and b. This would also remove a significant discrepancy between current AISC practice and other international standards.

With respect to the compact limit  $\lambda_p$ , it is recommended that this limit be split into  $\lambda_{p1}$  and  $\lambda_{p2}$  consistent with Eurocode Class 1 and Class 2 that provide  $M_p$  with minimum rotation and  $M_p$ , respectively. This will provide improved efficiency in some cases and will provide needed rotation capacity only where necessary—for example, in inelastic analysis with moment redistribution of AISC 360, Appendix 1. It is recommended that for simplicity, implementation in Chapter F need only use  $\lambda_{p2}$  since this establishes  $M_p$ , while AISC 360, Appendix 1, could reference the use of  $\lambda_{p1}$  for plastic design and/or material nonlinear analyses with redistribution.

In addition, the following is recommended: Align  $\lambda_p$  Case 12 (angle) with that of Case 10 (rolled flange in compression) or make it explicit that Case 12 only applies to the angle leg under stress gradient. Align  $\lambda_p$  Case 15 (I-section web) with that of Case 19 (box-section web) or provide evidence that I-section webs can have more liberal  $w/t$  limits than box-section webs (even beyond that of assuming a fully fixed edge boundary condition for the I-section web). Remove the use of residual stress ( $F_L$  vs.  $F_y$ ) in the Table B4.1 limits. As needed, correct application of limits in Chapter F after removal to ensure new limits are not unduly conservative.

### Seismic AISC 341 Recommendations

The task group recommendations for AISC 341 include rewriting the Table D1.1 Commentary: Provide objectives from the *Objectives* section of this paper (aligned with the *Specification*, not aspirational) and the finalized version of Table 7 in the Commentary or reference to archival publication. Note: The Commentary should describe intent and not imply specific values that are met by the  $w/t$  limits. Correct the  $\lambda_{md}$  and  $\lambda_{hd}$  limits back to their 2010 coefficients (and include  $R_y$ ). Provide an alternate pathway for the use

of cross-section elastic buckling analysis that includes web-flange interaction as an alternative to current  $w/t$  limits. Set  $\lambda_{md}^* = 0.5$  and  $\lambda_{hd}^* = 0.32$  for these alternative provisions. Adopt the proposed provisions for deep columns provided earlier.

### Additional Recommendations

A number of additional recommendations are also provided. Establish a research project to take advantage of the findings from the continuous strength method research and bring these advantages into the AISC 360 and AISC 341 standards. Active work in the development of AISC 370, *Specification for Structural Stainless Steel Buildings* (2021), may be utilized in this regard. Establish a research project to determine cyclic degradation in the strain capacity of plate elements subjected to local buckling such that AISC 341  $w/t$  criteria can be improved. Recent advances in cyclic fracture models of ductile steels can be leveraged as a mechanical basis for this effort, and the results have the potential to widely influence  $\lambda_{md}$  and  $\lambda_{hd}$  and their future application. Develop a test standard for establishing  $w/t$  limits (for AISC 360 and AISC 341) consistent with past practice and current application. This recommendation provides a pathway for alternative built-up shapes and new materials (steels) that may be impeded by current design rules. Extend AISC 360, Appendix 1, to provide alternative means for meeting  $\lambda_{pd}$  criteria based on cross-section slenderness, provide discussion/guidance on member rotational demands coming from nonlinear analysis, and show how to calculate member rotational capacity based on local cross-section slenderness.

### CONCLUSIONS

Cross-section width-to-thickness limits are a longstanding and reliable means to ensure behavioral objectives related to the local buckling performance of structural steel members. Establishing the underlying assumptions inherent in current width-to-thickness limits developed over the course of the last 80+ years is critical to advancing structural steel design for new steels and configurations. Existing width-to-thickness limits are presented in AISC *Specifications* in a manner suggesting each limit is unique to each element and loading, while actual limits are based on a small number of targeted, nondimensional plate slenderness regimes, where the nondimensional plate slenderness,  $\lambda^*$ , is defined based on the square root of the yield stress divided by the critical elastic plate buckling stress. Alternative methods that employ  $\lambda^*$  for local buckling of the complete cross section are capable of providing local buckling limits similar to current practice, but with greater simplicity and generality, and are worth considering as alternative means of meeting local buckling-based behavioral objectives for

both nonseismic and seismic local buckling limits. Seismic width-to-thickness limits provide for objectives far beyond strength and are used extensively to ensure ductility and avoid premature fracture in a variety of different seismic force-resisting systems. Proposals to improve current seismic width-to-thickness limits to account for the expected yield stress of the material and to handle web-flange interaction in local buckling of columns in moment frames are specifically addressed and recommendations provided. A series of recommendations spanning from practical—for example, provide two levels of compact section criteria to parallel Eurocode's Class 1 and Class 2 sections and adopt proposed provisions for deep columns in moment frames—to longer term—for example, provide alternative pathways for establishing local buckling limits are provided. This review of the current status of local buckling width-to-thickness limits was conducted by an ad hoc task group of the AISC Committee on Specifications during the development cycle for the 2022 editions of AISC 360 and AISC 341.

### ACKNOWLEDGMENTS

This paper is based on the work conducted by the AISC Task Group: Local Buckling (Width-to-Thickness Limits), which operated from 2017 to 2019 under the AISC Committee on Specifications (COS) with Ben Schafer as chair; Tim Fraser, Subhash Goel, Pat McManus, Don Sherman, Tom Sabol, Chia-Ming Uang, and Amit Varma as members; and Brent Leu as secretary. Additional AISC COS members and guests contributed at the in-person meetings as guests of the Task Group. In particular, Lou Geschwindner, Perry Green, Kerry Kreitman, and Don White all contributed substantially to the Task Group's work. All contributions and efforts of the Task Group members and friends are acknowledged and thanked by the authors.

### REFERENCES

- AASHTO (2017), *LRFD Bridge Design Specification*, 8th Ed., American Association of State Highway and Transportation Officials, Washington, D.C.
- Afshan, S. and Gardner, L. (2013), "The Continuous Strength Method for Structural Stainless Steel Design," *Thin-Walled Structures*, Vol. 68, pp. 42–49. doi:10.1016/j.tws.2013.02.011.
- AIJ (2010), *Recommendation for Limit State Design of Steel Structures*, Architectural Institute of Japan.
- AISC (1986), *Load and Resistance Factor Design Specification for Structural Steel Buildings*, American Institute of Steel Construction, Chicago, Ill.
- AISC (1990), *Seismic Provisions for Structural Steel Buildings*, American Institute of Steel Construction, Chicago, Ill.

- AISC (1999), *Load and Resistance Factor Design Specification for Structural Steel Buildings*, American Institute of Steel Construction, Chicago, Ill.
- AISC (2010), *Seismic Provisions for Structural Steel Buildings*, ANSI/AISC 341-10, American Institute of Steel Construction, Chicago, Ill.
- AISC (2016a), *Seismic Provisions for Structural Steel Buildings*, ANSI/AISC 341-16, American Institute of Steel Construction, Chicago, Ill.
- AISC (2016b), *Specification for Structural Steel Buildings*, ANSI/AISC 360-16, American Institute of Steel Construction, Chicago, Ill.
- AISC (2021), *Specification for Structural Stainless Steel Buildings*, ANSI/AISC 370-21, American Institute of Steel Construction, Chicago, Ill.
- AISI (2016), *North American Specification for the Design of Cold-Formed Steel Structural Members*, AISI S100-16, American Iron and Steel Institute, Washington, D.C.
- Allen, H.G. and Bulson, P.S. (1980), *Background to Buckling*, McGraw-Hill, New York, N.Y.
- ASCE (2021), *Specification for the Design of Cold-Formed Stainless Steel Structural Members*, SEI/ASCE 8-21, American Society of Civil Engineers, Reston, Va.
- CEN (2004), *Eurocode 3: Design of Steel Structures*, EN 1993-1-1 2004, Comité Européen de Normalisation, Brussels, Belgium.
- Chansuk, P., Ozkula, G., and Uang, C.-M. (2018), “Seismic Behavior and Design of Deep, Slender Wide-Flange Structural Steel Beam-Column Members: Phase 2,” Report No. SSRP-18/02, Department of Structural Engineering, University of California, San Diego, La Jolla, Calif.
- Elkady, A. and Lignos, D.G. (2018), “Full-Scale Testing of Deep Wide-Flange Steel Columns under Multi-Axis Cyclic Loading: Loading Sequence, Boundary Effects and Out-of-Plane Brace Force Demands,” *Journal of Structural Engineering*, Vol. 144, No. 2.
- Fieber, A., Gardner, L., and Macorini, L. (2019), “Design of Structural Steel Members by Advanced Inelastic Analysis with Strain Limits,” *Engineering Structures*, Vol. 199. doi:10.1016/j.engstruct.2019.109624.
- Gardner, L., Fieber, A., and Macorini, L. (2019), “Formulae for Calculating Elastic Local Buckling Stresses of Full Structural Cross-Sections,” *Structures*, Vol. 17, pp. 2–20. doi:10.1016/j.istruc.2019.01.012.
- Haaïjer, G. and Thurlimann, B., (1960), “On Inelastic Buckling in Steel,” *Proceedings ASCE*, 84 (EM2), p. 1581 [also *Transactions ASCE*, Vol. 125 (1960), Reprint No. 124 (60-2), (1960)], Fritz Laboratory Reports, Paper 1,426.
- ICBO (1988), *Uniform Building Code*, International Council of Building Officials, Whittier, Calif.
- Johnson, D. (1976), “Buckling of Beam Compression Flanges,” Report to American Iron and Steel Institute.
- Lukey, A.F., and Adams, P.F. (1969), “The Rotation Capacity of Beams under Moment Gradient,” *Journal of the Structural Division*, ASCE, Vol. 95, No. 6, pp. 1,173–1,188.
- Ozkula, G. and Uang, C.-M., (2015), “Seismic Behavior and Design of Deep, Slender Wide-Flange Structural Steel Beam-Column Members: Phase 1,” Report No. SSRP-15/06, Department of Structural Engineering, University of California, San Diego, La Jolla, Calif.
- Ozkula, G., Uang, C.-M., and Harris, J. (2021), “Development of Enhanced Seismic Compactness Requirement for Webs in Wide-Flange Steel Columns,” *Journal of Structural Engineering* (accepted).
- Salmon, C., Johnson, J., and Malhas, F. (2009), *Steel Structures: Design and Behavior*, 5th Ed., Pearson, New York.
- Schafer, B.W. (2019), “Advances in the Direct Strength Method of Cold-Formed Steel Design,” *Thin-Walled Structures*, Vol. 140, pp. 533–541. doi:10.1016/j.tws.2019.03.001.
- Schafer, B.W., Fraser, T. Goel, S., McManus, P., Sherman, D., Sabol, T., Uang, C.-M., and Varma, A. (2020), “Task Group Report on Local Buckling (Width-to-Thickness) Limits,” prepared by the AISC Committee on Specifications Ad Hoc Task Group on Local Buckling (Width-to-Thickness) Limits, January 7, AISC, Chicago, Ill.
- Seif, M. and Schafer, B.W. (2010), “Local Buckling of Structural Steel Shapes,” *Journal of Constructional Steel Research*, Vol. 66, pp. 1,232–1,247.
- Torabian, S. and Schafer, B.W. (2014), “Role of Local Slenderness in the Rotation Capacity of Structural Steel Members,” *Journal of Constructional Steel Research*, Vol. 95, pp. 32–43.
- White, D.W. (2008), “Unified Flexural Resistance Equations for Stability Design of Steel I-Section Members: Overview,” *Journal of Structural Engineering*, ASCE, Vol. 134, No. 9, pp. 1,405–1,424.
- Wilkinson, T. and Hancock, G.J. (1998), “Tests to Examine Compact Web Slenderness of Cold-Formed RHS,” *Journal of Structural Engineering*, ASCE, Vol. 124, No. 10, pp. 1,166–1,174.
- Winter, G. (1947), “Strength of Thin Steel Compression Flanges,” *Transactions of the American Society of Civil Engineers*, Vol. 112, No. 1, pp. 527–554.
- Wu, T.Y., El-Tawil, S., and McCormick, J. (2018), “Highly Ductile Limits for Deep Steel Columns,” *Journal of Structural Engineering*, ASCE, Vol. 144, No. 4, 04018016.

Zhao, O., Afshan, S., and Gardner, L. (2017), "Structural Response and Continuous Strength Method Design of Slender Stainless Steel Cross-Sections," *Engineering Structures*, Vol. 140, pp. 14–25. doi:10.1016/j.engstruct.2017.02.044.

Ziemian, R. (2010), *Guide to Stability Design Criteria for Metal Structures*, 6th Ed., Wiley, New York, N.Y.

# ERRATA

## AISC Provisions for Web Stability under Local Compression Applied to HSS

Fei Wei and Jeffrey A. Packer

Vol. 58, No. 1, 2021

In the following tables, Equations 4, 15, and 16 are shown incorrectly due to typesetting errors and should be revised as noted.

Revise Table 1, Row 4, Equation 4 to:

$$\frac{0.8t^2}{\sin\theta} \left( 1 + \frac{\frac{3H_b}{\sin\theta}}{H} \right) \sqrt{EF_y Q_f}$$

Revise Table 6, Row 1, Equation 15 to:

$$2F_y t \left( 7.5t + \frac{H_b}{\sin\theta} \right)$$

Revise Table 6, Row 2, Equation 16 to:

$$1.6t^2 \left( 1 + \frac{\frac{3H_b}{\sin\theta}}{H} \right) \sqrt{EF_y Q_f}$$





## Guide for Authors

**Scope** *Engineering Journal* is dedicated to the improvement and advancement of steel construction. Its pages are open to all who wish to report on new developments or techniques in steel design, research, the design and/or construction of new projects, steel fabrication methods, or new products of significance to the uses of steel in construction. Only original papers should be submitted.

**General** Papers intended for publication should be submitted by email Margaret Matthew, editor, at [matthew@aisc.org](mailto:matthew@aisc.org).

The articles published in the *Engineering Journal* undergo peer review before publication for (1) originality of contribution; (2) technical value to the steel construction community; (3) proper credit to others working in the same area; (4) prior publication of the material; and (5) justification of the conclusion based on the report.

All papers within the scope outlined above will be reviewed by engineers selected from among AISC, industry, design firms, and universities. The standard review process includes outside review by an average of three reviewers, who are experts in their respective technical area, and volunteers in the program. Papers not accepted will not be returned to the author. Published papers become the property of the American Institute of Steel Construction and are protected by appropriate copyrights. No proofs will be sent to authors. Each author receives three copies of the issue in which his contribution appears.

**Manuscripts** Manuscripts must be provided in Microsoft Word format. Include a PDF with your submittal so we may verify fonts, equations and figures. View our complete author guidelines at [aisc.org/ej](http://aisc.org/ej).



.....  
**Smarter. Stronger. Steel.**

.....  
American Institute of Steel Construction  
130 E Randolph St, Ste 2000, Chicago, IL 60601  
312.670.2400 | [aisc.org/ej](http://aisc.org/ej)